Doctoral Dissertation
Doctoral Program in Civil and Environmental Engineering (XXXIII cycle)
Doctoral Program in Mechanics, Energetics, Civil Engineering, Acoustics

Modelling pollutant dispersion at the city and street scales

From wind tunnel experiments to complex network theory

Sofia Fellini

* * * * *

Supervisors
Prof. Luca Ridolfi
Prof. Pietro Salizzoni

Doctoral examination committee
Prof. Andrea Rinaldo, Referee, EPFL, Università di Padova
Prof. Maarten van Reeuwijk, Referee, Imperial College
Prof. Silvana Di Sabatino, Università di Bologna
Prof. Catherine Gorlé, Stanford University
Prof. Costantino Manes, Politecnico di Torino
Dr. Enrico Ser-Giacomi, MIT, LOCEAN

Politecnico di Torino
École Centrale de Lyon
2021

I hereby declare that, the contents and organisation of this dissertation constitute my own original work and does not compromise in any way the rights of third parties, including those relating to the security of personal data.

Sofia Fellini
Turin, February 08, 2021

Allez les filles, au travail!

VALERIA SOLESIN

Acknowledgements

I express my deep gratitude to my supervisors Luca Ridolfi and Pietro Salizzoni, who involved me in this adventure. Their guidance, knowledge and enthusiasm have been a fundamental support for the development of this thesis and for my growth as a researcher.

I thank the Italian-French University for funding this PhD scholarship, and the University of Lyon and the ScuDo for the financial support for my mobility in France.

I would like to express my gratitude to professors Andrea Rinaldo and Maarten Van Reeuwijk. I was honored to have them as reviewers of this thesis.

I am grateful to all the members of the LMFA laboratory in Lyon for making me feel part of the group. Thanks in particular to the equipe AIR for giving me access to urban data and to the software SIRANE. My gratitude also goes to Massimo Marro for supporting me in the wind tunnel experiments.

I would like to extend my gratitude to professor Ilaria Butera for giving me the opportunity to teach in her master course.

Thanks to Carla McRae for her inspirational illustration on the cover of this thesis, and thanks to Journal Matters for giving me permission to use it.

I thank my undergraduate students but also adventure mates Michele, Alessandro, Giacomo, Giulia. Part of the results of this thesis is due to them.

Special thanks to all the brilliant and funny colleagues I met in Lyon and Turin (the very BAD ones). Most of my personal growth on this PhD journey is thanks to their friendship, intelligence and exuberance.

Finally, thanks to my family who patiently follows my crazy stories.
Thanks to Alessandro, for always being on my side.

Summary

Air pollution in urban areas is a major concern for the health and safety of citizens. Hubs of economic, political and social activities, cities are densely populated and are exposed to a large number of pollution sources. These factors, together with the risk of malicious acts for terrorist purposes, make them extremely vulnerable to gaseous releases. To predict and manage air pollution scenarios, the understanding and modelling of dispersion phenomena in the urban atmosphere is crucial. Differently from transport processes far from boundaries, flow and dispersion in the urban canopy are primarily governed by the intricate geometry of the city. The aim of this thesis is to investigate and model the effect of urban form on the dispersion of pollutants at two different spatial scales: at the scale of the district and at the scale of the single street canyon.

Urban street pattern is the dominant geometry at the district scale. Starting from this observation, the first part of this thesis proposes a new perspective based on the theory of complex networks to analyze and model the transport of pollutants along the streets of a city. The urban canopy is modelled as a network. Street canyons and their intersections shape the spatial structure of the network. The direction and the transport capacity of the flow in the streets define the direction and the weight of the links. Adopting this mathematical interpretation, propagation is modelled as a spreading process on a network and the most dangerous areas in a city are identified as the best spreading nodes. To this aim, a novel centrality metric tailored to mass transport in flow networks is derived. Besides providing an operational tool to identify the places in a city with the highest potential for dispersion over large areas, the proposed approach is suitable to investigate which structural properties of a city make it fragile to air pollution. The comparison between four emblematic cities with different urban patterns evidences that vulnerability is driven by the topological properties of the urban fabric, i.e. street connectivity and the variability in the orientation of the streets with respect to the approaching wind.

At the scale of the single street, flow and dispersion dynamics are governed by the canyon geometry. The dispersion of pollutants can be decomposed in the longitudinal transport along the street and the vertical transfer between the canyon and the external flow. While advection drives the dynamics along the canyon axis, the

mechanisms of mass exchange in the vertical direction are still not fully understood. The second part of this thesis investigates these processes by means of wind tunnel experiments of pollutant dispersion in a canyon oriented perpendicular to the wind direction. In this configuration, the vertical exchange is the dominant mechanism of canyon ventilation. Keeping the external flow unaltered, we analyse the effect of different boundary conditions at the building walls and the presence of obstacles within the canyon. The boundary conditions are modified by alternatively heating the downwind and upwind walls of the canyon, by changing its aspect ratio and by introducing roughness elements at walls. Two rows of model trees are arranged at the sides of a street canyon to simulate urban vegetation. Velocity and concentration measurements are performed within the canyon and a characteristic exchange velocity between the street canyon and the overlying atmosphere is estimated to quantify the overall canyon ventilation in the different configurations. Results evidence that the efficiency of the vertical exchange between the canyon and external flow is mainly driven by the fluctuating component of the turbulent flow within the canyon. The intensity and spatial distribution of the turbulent kinetic energy field varies according to the geometry of the canyon, the conditions imposed at the walls and the presence of obstacles.

In short, this thesis contributes to our understanding of (i) the role of urban geometry in the dispersion of pollutants, and (ii) the physical mechanisms that govern urban ventilation. Moreover, the techniques and methods adopted in this study highlight the importance of a multi-scale approach and the potential of innovative tools, both conceptual and experimental, to develop operational models for the assessment of urban air pollution.

Résumé

La pollution atmosphérique dans les zones urbaines constitue une menace sérieuse pour la santé et la sécurité des résidents. Centres d'activité économique, politique et sociale, les villes sont densément peuplées et exposées à un grand nombre de sources de pollution. Ces facteurs, ainsi que le risque d'actes malveillants à des fins terroristes, les rendent extrêmement vulnérables aux rejets gazeux. Afin de prévoir et gérer la pollution atmosphérique, il est très important de comprendre et de modéliser les phénomènes de dispersion dans l'atmosphère urbaine. Contrairement au transport loin des parois, l'écoulement et la dispersion dans la canopée urbaine sont principalement régis par la géométrie complexe de la ville. L'objectif de cette thèse est d'étudier et de modéliser l'effet de la forme urbaine sur la dispersion des polluants à deux échelles spatiales différentes: à l'échelle du quartier et à l'échelle de la rue.

Le tracé des rues est la géométrie dominante à l'échelle du quartier. Partant de ce constat, la première partie de cette thèse propose une nouvelle perspective basée sur la théorie des réseaux complexes pour analyser et modéliser le transport de polluants le long des rues d'une ville. La canopée urbaine est modélisée comme un réseau. Les rues-canyons et leurs intersections façonnent la structure spatiale du réseau. La direction et la capacité de transport de l'écoulement dans les rues déterminent les directions et le poids des liens du réseau. Avec cette interprétation mathématique, la propagation est modélisée comme un processus de diffusion sur un réseau et les zones les plus dangereuses d'une ville sont identifiées comme les nœuds avec le potentiel de diffusion le plus élevé. Dans ce but, nous introduisons une nouvelle métrique de centralité adaptée au transport de masse dans les réseaux de flot. L'approche proposée fournit un outil opérationnel pour identifier les lieux d'une ville avec le potentiel de dispersion le plus élevé. En outre, le modèle est utile pour identifier les propriétés structurelles qui rendent les villes vulnérables à la pollution atmosphérique. La comparaison entre quatre villes emblématiques, aux plans urbains différents, montre que la vulnérabilité dépend des propriétés topologiques du tissu urbain: la connectivité des rues et la variabilité de l'orientation des rues par rapport à la direction du vent extérieur.

À l'échelle de la rue, les dynamiques d'écoulement et de dispersion sont régies par la géométrie du canyon. Le transport des polluants peut être décomposée en

transport longitudinal le long de la rue et en transfert vertical entre le canyon et l'écoulement extérieur. La vitesse moyenne de l'écoulement régit la dispersion le long de la rue. En revanche, les mécanismes d'échange de masse dans le sens vertical ne sont pas encore parfaitement compris.
La deuxième partie de cette thèse analyse ces processus à l'aide d'expériences en soufflerie qui simulent la dispersion de polluants dans un canyon orienté perpendiculairement à la direction du vent. Dans cette configuration, l'échange vertical est le seul mécanisme de ventilation du canyon. Au cours des expériences, les conditions du canyon sont modifiées en chauffant alternativement les parois latérales, en modifiant le rapport hauteur/largeur du canyon et en introduisant des éléments de rugosité sur les parois. Deux rangées de maquettes d'arbres sont disposées le long du canyon pour simuler la végétation urbaine. Des mesures de vitesse et de concentration sont effectuées dans le canyon et une vitesse d'échange caractéristique entre la rue-canyon et l'atmosphère sus-jacente est estimée pour quantifier la ventilation globale du canyon dans les différentes configurations. Les résultats montrent que l'efficacité de l'échange vertical entre le canyon et l'écoulement externe est principalement déterminée par l'énergie cinétique turbulent à l'intérieur du canyon. L'intensité et la distribution spatiale du champ de l'énergie cinétique turbulente changent en fonction de la géométrie du canyon, des conditions imposées aux parois et de la présence d'obstacles.

En synthèse, cette thèse contribue à notre compréhension (i) du rôle de la géométrie urbaine dans la dispersion des polluants, et (ii) des mécanismes physiques qui régissent la ventilation urbaine. De plus, les techniques et méthodes adoptées dans cette étude mettent en évidence (i) l'importance d'une approche multi-échelles et (ii) le potentiel d'outils innovants, à la fois conceptuels et expérimentaux, pour développer des modèles opérationnels de simulation de la pollution atmosphérique dans les villes.

Sommario

L'inquinamento atmosferico nelle aree urbane rappresenta una grave minaccia per la salute e la sicurezza dei cittadini. Centri di attività economica, politica e sociale, le città sono densamente popolate ed esposte a un gran numero di sorgenti inquinanti. Questi fattori, assieme al rischio di atti dolosi a scopo terroristico, le rendono estremamente vulnerabili ai rilasci gassosi. Al fine di prevedere e gestire l'inquinamento atmosferico, è fondamentale comprendere e modellare i fenomeni di dispersione nell'atmosfera urbana. A differenza delle dinamiche lontano da parete, il flusso e la dispersione nel tessuto urbano sono governati principalmente dalla complessa geometria della città. L'obiettivo di questa tesi è studiare e modellare l'effetto della forma urbana sulla dispersione di inquinanti a due diverse scale spaziali: a livello del quartiere e a livello della singola strada.

Alla scala del quartiere, la geometria dominante è quella del reticolo urbano. Partendo da questa osservazione, la prima parte della tesi propone un metodo innovativo, basato sulla teoria delle reti complesse, per analizzare e modellare il trasporto di inquinanti lungo le strade di una città. Il dominio urbano è modellato come una rete. Le strade e gli incroci danno forma alla struttura spaziale della rete. La direzione del vento e la sua capacità di trasporto nelle strade determinano la direzione e il peso dei link della rete. Grazie a questa interpretazione matematica, la propagazione viene modellata come un processo di diffusione su rete e le aree più pericolose di una città vengono identificate come i nodi con il più alto potenziale di diffusione. Per stimare tale potenziale, introduciamo una nuova metrica di centralità in grado di descrivere il trasporto di massa nelle reti di flusso. L'approccio proposto fornisce uno strumento operativo per l'identificazione delle aree di una città con il più alto potenziale di dispersione. Inoltre, il modello è utile per investigare quali proprietà strutturali rendono le città maggiormente vulnerabili all'inquinamento atmosferico. Il confronto tra quattro città emblematiche, con differenti strutture urbanistiche, mostra che la vulnerabilità dipende dalle proprietà topologiche del tessuto urbano: dalla connettività delle strade e dallla variabilità dell'orientamento delle strade rispetto alla direzione del vento esterno.

Alla scala della singola strada, le dinamiche di flusso e di dispersione sono regolate dalla geometria del canyon stradale. Il trasporto di inquinanti può essere

scomposto in un trasporto longitudinale lungo la strada e in un trasferimento verticale tra il canyon e l'atmosfera esterna. La velocità media del vento lungo la strada governa il trasporto longitudinale, mentre i meccanismi di scambio di massa nella direzione verticale non sono ancora compresi appieno.
La seconda parte della tesi analizza questi processi di scambio tramite esperimenti in galleria del vento che simulano la dispersione di inquinanti in un canyon orientato perpendicolarmente rispetto alla direzione del vento. In questa configurazione, lo scambio verticale è l'unico meccanismo di ventilazione del canyon. Negli esperimenti, le condizioni del canyon vengono modificate riscaldando alternativamente le pareti laterali, cambiando il rapporto altezza / larghezza del canyon e introducendo elementi di rugosità sulle pareti. Inoltre, due file di modellini di alberi sono disposte lungo il canyon per simulare la presenza di vegetazione urbana. All'interno del canyon vengono effettuate misure di velocità e di concentrazione. Infine, viene stimata una velocità caratteristica di scambio tra la strada e l'atmosfera sovrastante per quantificare la ventilazione complessiva del canyon nelle diverse configurazioni. I risultati mostrano che l'efficienza dello scambio verticale tra il canyon e il flusso esterno è determinata principalmente dall'energia cinetica turbolenta all'interno del canyon. L'intensità e la distribuzione spaziale del campo di energia cinetica turbolenta variano a seconda della geometria del canyon, delle condizioni imposte alle pareti e della presenza di ostacoli.

In sintesi, questa tesi contribuisce alla nostra comprensione (i) del ruolo della geometria urbana nella dispersione degli inquinanti e (ii) dei meccanismi fisici che governano la ventilazione urbana. Inoltre, le tecniche e i metodi adottati in questo studio evidenziano (i) l'importanza di un approccio multi-scala e (ii) il potenziale di strumenti innovativi, sia concettuali che sperimentali, per sviluppare modelli operativi di simulazione dell'inquinamento atmosferico nelle città.

Contents

List of Tables

List of Figures

Nomenclature

Greek symbols

α	Thermal diffusivity
α_p	Aerodynamic porosity
β	Ratio of geometrical volumes in the box model
β_p	Optical porosity
γ	Ratio of concentration in the box model
ΔT	Temperature difference between the canyon walls
δ	Depth of the boundary layer
Θ	Local average of street orientation ($\cos(\theta)$) in a street network
ϑ	Heaviside function
θ	Angle between the street canyon and the external wind
κ	Von Karman constant
$\varkappa$	Node degree
ν	Kinematic viscosity
Φ	External wind direction with respect to the street network
ρ	Correlation coefficient
ρ_a	Air density
σ	Standard deviation of street orientation in the neighborhood of a node
σ_u^2,σ_v^2	Variances of the velocity components
$\overline{\boldsymbol{\omega}}$	Average vorticity field

Latin symbols

$\mathbf{A}$	Adjacency matrix
b	Branching index
C	Average concentration over a generic volume
c	Average concentration over a transversal section of the street
c_d	Drag coefficient
c_t	Instantaneous scalar concentration
$\langle c_t \rangle$	Ensemble average for the concentration
c_{th}	Threshold concentration for contamination to be relevant
c_0	Concentration at the source node
$\mathbf{D}$	Matrix storing the length of the shortest paths
$\mathcal{D}$	Shortest path between two nodes in a network
D_m	Mass diffusivity
d	Displacement height
$\mathcal{E}$	Edge-set of the graph
F	Drag force
Fr_i	Internal Froude number
$\mathcal{G}$	Network
$\mathbf{H}$	Matrix of the height of the street canyons
$\mathcal{H}$	Local average of canyon height in a street network
H	Height of a street canyon
h_r	Roughness height at the canyon walls
h_t	Heat transfer coefficient
h_T	Height of model trees
$I, I_\varepsilon, I_\mathcal{N}$	Error indexes for the delimitation of the zone of influence
$\mathcal{K}$	Tailored centrality metric for spreading potential of airborne pollutants
$\mathcal{K}_{clos}$	Closeness centrality
$\mathcal{K}_{harm}$	Harmonic centrality

$\mathbf{L}$	Matrix of the length of the street canyons
$\mathcal{L}$	Local average of the street length in a street network
L	Length of a street canyon
M	Number of edges in the network
$\dot{M}_q$	Mass flow rate of ethane per unit length at the source
N	Number of nodes in the network
$\mathcal{N}_1$	Set of first neighbors
$\hat{\mathcal{N}}_1$	Set of the first neighbours that have been contaminated
$\mathbf{P}$	Matrix of the number of inhabitants per unit length of the streets
$\mathcal{P}$	Path in a complex network
Pr	Prandtl number
Q	Mass flow rate of ethane at the source
$\dot{q}$	Thermal flux at the heated wall
r	Number of reachable links from a source node (reachability)
Re	Reynolds number
$\mathcal{S}$	Node-set of the graph
S	Exchange surface in a cavity
s	Source node in a street network
Sc	Schmidt number
T_0	Reference temperature
T_w	Mean temperature of the heated wall of the canyon
$\mathcal{U}$	General velocity scale
$\mathbf{u}$	Velocity vector
u	Instantaneous velocity along the x direction
$\overline{u}$	Single-point time average of u
$\mathbf{U_d}$	Matrix of the vertical exchange velocity u_d
$\mathbf{U_{st}}$	Matrix of the longitudinal velocity u_{st}
U_H	Wind speed at the building height
U_∞	Free stream velocity at the top of the boundary layer
u_d	Bulk velocity of vertical exchange

u_{st}	Average flow velocity in the y direction
u_*	Roughness velocity
$\mathcal{V}$	Vulnerability index as total number of affected people
v	Instantaneous velocity along the z direction
$\overline{v}$	Single-point time average of v
V_{tot}	Volume of the street canyon/cavity
$\mathcal{W}$	Local average of the width of the street canyons in a street network
W	Width of a street canyon
$\mathbf{w}$	Weight matrix associated to the graph
x, y, z	Coordinates in the transversal, longitudinal and vertical direction
$\mathbf{Z}$	Matrix of the contaminated length of the streets
$\mathcal{Z}$	Zone of influence of a source node as set of contaminated links
z^*	Blending height
z_0	Aerodynamic roughness

Acronyms

CFD	Computational Fluid Dynamics
DW	Downwind
FID	Flame Ionisation Detector
LES	Large Eddy Simulation
PIV	Particle Image Velocimetry
RAN	Reynolds-averaged Navier–Stokes
TKE	Turbulent Kinetic Energy
UP	Upwind

Introduction

Since ancient times, cities have been crossroads for peoples and nuclei of civilization. Arising along trade routes, they were the essential hubs of commerce and became centres of knowledge, innovation and economy [Hall, 1998]. The role of cities has become increasingly important in recent decades and this trend is set to intensify in the near future, due to the progressive shift of people from rural to urban areas. By 2050, 70% of the world's population is expected to live in cities [Field, 2014] – a remarkable increase from the current 55%.

The vibrant economic and cultural life of cities is supported by facilities whose efficiency and coordination guarantee the economic growth and livability of urban areas. The image of the city as an efficient system of parts inspired the analogy of the *city as a machine* [Lynch, 1984]. According to this concept, the structure of a city and its services can be planned and rebuilt following bottom up regulations aimed at convenience and functionality (Fig. 1.a). In this sense, the city form is designed for practical aims (e.g., the grid plan of Roman colonies or New York city) and organized in a regular and adaptable way. Since the twenty-first century, this paradigm has been supplanted by the vision of the *city as an organism* (Fig. 1.b) [Graedel, 1999, Batty, 2009]. Unlike a machine, an organism does not grow by simple spatial extension or addition of parts but reorganizes its form as its size increases. These self-regulating mechanisms are aimed at maximizing the metabolic capacity and minimizing the energy dissipation in living systems. For example, most of the physiological characteristics of biological organisms tend to scale with their body mass, according to specific power law relations [West et al., 1999]. In a similar way, many urban indicators (e.g., GDP, employment, infrastructure or innovation) are observed to be power law functions of population size [Bettencourt et al., 2007, Bettencourt, 2013, Bettencourt, 2020]. As a living organism, the city needs many resources, i.e. energy, food, and materials. The *urban metabolism* [Wolman, 1965, Kennedy et al., 2007] guarantees the functioning and prosperity of the city while producing emissions and waste. Conceiving cities as evolving organisms and understanding the pattern of energy and material flows between the city and the surrounding environment is crucial to develop key strategies for urban sustainability.

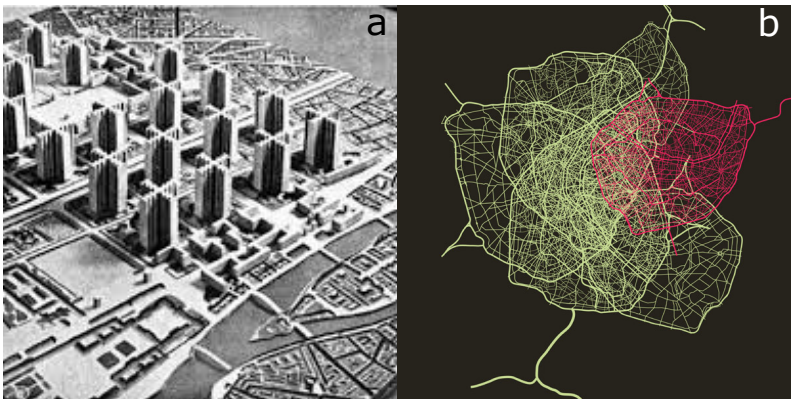

Figure 1: a) Model of the Plan Voisin for the city of Paris, planned by Le Corbusier in 1925. b) Artist's impression of the temporal evolution of Paris street pattern by designer Lee Jang Sub in the ComplexCity Project [Lee Jang Sub, 2008].

Today, cities account for about 78% of the world's energy and are responsible for more than 60% of the planet's greenhouse gas emissions, while covering less than 2% of the Earth's surface [UN, 2019]. Cities put a lot of pressure on natural resources and are largely responsible for climate change. At the same time, cities are already feeling the consequences of this exploitation of resources. Many urban areas suffer from dangerously high levels of air pollution from fossil fuel combustion and they are exposed to floods, heat waves, rainstorms and droughts due to the increasingly frequent extreme weather events.

Besides environmental risks, the high population density makes cities especially vulnerable to safety and health risks. Terrorism affects city centres as they are crowded environments, as well as strategic and symbolic sites. Similarly, closeness between people and the sharing of spaces and urban infrastructures exposes urban centres to the spread of contagious diseases, as unveiled by the current COVID-19 outbreak.

These considerations evidence cities as the main drivers of human activity, albeit evolving complex systems with emerging fragilities. For these reasons, the transition to sustainable and livable urban environments is a crucial challenge [Tominaga and Stathopoulos, 2016, Bibri and Krogstie, 2017, Güneralp et al., 2017, Seto et al., 2017] for the next decades and one of the sustainable development goals of the United Nations (SDG11). Fortunately, cities are equipped to tackle challenges thanks to their inclination to innovation and change.

The management of air pollution plays a major role in this transition. According to the World Health Organization (WHO) [WHO, 2018], air pollution causes around seven million premature deaths each year, largely due to increased mortality from stroke, lung disease, and heart disease [Brunekreef and Holgate, 2002].

Cities are the most impacted, with more than 80% of people living in urban areas exposed to air quality levels that exceed the WHO limits. These statistics are even worse for low and middle income countries. Outdoor and indoor environments are both responsible for exposure to air pollution. As people are spending an increasing proportion of their time in buildings, the awareness about indoor air quality is growing remarkably [Bo et al., 2017].

The main pollutant sources in urban areas [Mayer, 1999] are vehicular traffic [Heinrich and Wichmann, 2004] (CO_2, CO, NO_X, COV and particulate matter), exhausts from industries (SO_2, heavy metals) and residential heating (CO_2, CO, SO_2). However, accidental releases such those related to gas leaks (CH_4), industrial plants or the transport of hazardous material (e.g., explosive, flammable, asphyxiating gases) are also especially dangerous in densely populated environments. Besides unintentional releases, toxic substances (e.g., chlorine or sarin gases, bacterial pathogens) could be maliciously dispersed in the urban atmosphere for terrorist purposes. The attacks in Matsumoto and in Tokyo subway (Japan) and the use of chemical weapons during the Syrian civil war have shocked the international public opinion and raised fears of similar attacks in the future [Tucker, 2000, McLeish, 2017].

For these reasons, public authorities are urged to adopt instruments for the prevention of risks related to air pollution in urban areas. Monitoring networks are fundamental tools for controlling levels of pollution and detecting anomalies due to unexpected releases. Technological advances and the development of affordable sensors are facilitating the capillary detection of air quality parameters in urban areas [Kumar et al., 2015]. Alongside monitoring activities, the role of modeling is crucial. Simulations of the spatial and temporal distribution of pollutant concentration provide valuable information for the optimal positioning of monitoring sensors, and for the assessment of the measured data. Moreover, models are essential to analyse scenarios and support decision-makers in interventions and regulations, as multiple strategies for the mitigation of air pollution can be assessed in advance. Finally, models are predictive tools for the management of dangerous situations resulting from unexpected releases.

To address these issues, many efforts have been invested by the scientific community to develop accurate models of pollutant dispersion in urban areas [Di Sabatino et al., 2013, Blocken, 2015, Tominaga and Stathopoulos, 2016]. These require a deep understanding of the urban microclimate [Santamouris et al., 2001, Oke, 2002, Harman and Belcher, 2006] which is the result of the complex interaction between physical phenomena (e.g., wind, atmospheric stability, solar radiation) and the city (e.g., buildings, anthropogenic emissions, urban vegetation).

In air pollution models, the geometry of the urban area is represented in different ways depending on the spatial and temporal scales of the dispersion phenomenon under consideration. Usually, three spatial scales are adopted (Fig. 2): the regional scale ($\simeq 100$ km), the city-district scale ($\simeq 1-10$ km), and the street scale ($\simeq 100$

m).

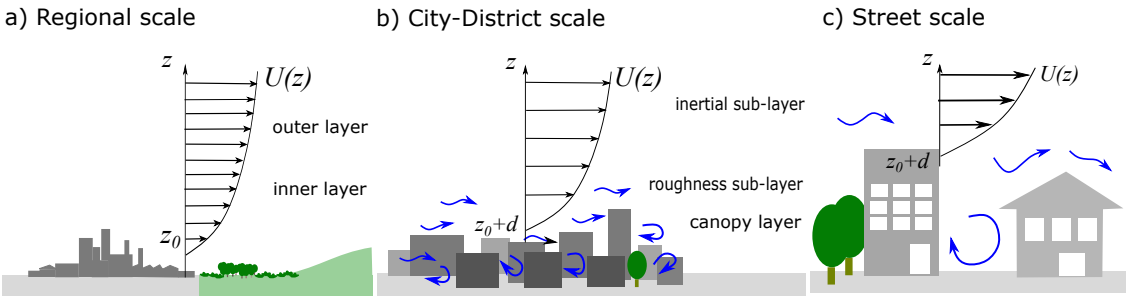

Figure 2: Boundary layer flow a the (a) regional, (b) city-district, and (c) street scale.

The regional scale

When the focus is on pollution processes involving spatial scales of the order of tens of kilometers and time scales of the order of hours, dispersion models at the regional scale are adopted. A typical example is ground-level ozone pollution which is the result of photochemical transformations of anthropogenic emissions - mainly from vehicular traffic and industries - occurring on a day time scale. In this time interval, pollutants travel great distances and are affected by (i) horizontal transport due to mesoscale circulations (e.g., thunderstorms, gap-winds, breezes), and (ii) vertical turbulent mixing, generated mostly by mechanical and thermal effects due to the presence of the Earth's surface. The thermal origin of turbulence is due to the heating of the surface by solar radiation that induces convective phenomena. On the other hand, mechanical turbulence originates from the shear of the wind with the Earth's surface. The wind speed is zero at the ground, due to the no-slip condition, and increases as the distance from the ground increases. This vertical velocity gradient produces instabilities in the air flow that originate turbulence. The mean velocity profile near the surface, in the so-called *inner* or *inertial* region, can be approximated with a logarithmic law of the form:

$$\frac{\overline{u}}{u_*} = \frac{1}{\kappa} \ln \frac{z}{z_0}, \tag{1}$$

where $\overline{u}$ is the mean horizontal velocity, z is the vertical coordinate, κ is the von Karman constant, u_* is the friction velocity, i.e. a reformulation of the shear stress τ in units of velocity, and z_0 is the roughness length which is related to the height of the surface irregularities.

Urban areas affect both roughness and temperature characteristics of the Earth's surface. The presence of buildings enhances surface roughness, while the heat island effect is responsible for an increase in temperature [Oke, 1982]. This phenomenon

is mainly due to the low albedo of buildings (less reflection of the sun's rays), the complex urban geometry which tends to trap escaping radiations, and the reduction of evaporation and transpiration, due to the scarce presence of vegetation.

In models at the regional scale, the effect of urban areas on the flow is taken into account by means of few parameters. Typically, the city is considered as a homogeneous region characterized by higher roughness (i.e., higher z_0 [Wiernga, 1993]) and temperature with respect to surrounding rural areas.

The city-district scale

When pollutants are rapidly transported through the streets of a city with an immediate effect on citizens' health, the urban geometry needs to be described in more detail. This is the case of a street level explosion in a city centre. The propagation of toxic gases is influenced by the orientation of the streets and by the geometry of the buildings. The concentration of pollutants (especially local concentration peaks) depends on the intensity of the wind in the streets and on vertical exchanges between streets and the above atmosphere. Therefore, in models at the city-district scale, characterization of the flow field within and above buildings is no longer negligible.

Near the urban surface, the flow field is three-dimensional since it is influenced by length scales of the individual roughness elements that form the urban canopy. This region is called *roughness sub-layer* and includes the canopy layer. With increasing distance from the ground, the aerodynamic effect of the individual obstacles is no longer distinguishable and the flow is affected by a homogeneous drag. In this region (the *inner* or *inertial* region), the flow can be assumed to be homogeneous on the horizontal plane and variable only with the vertical coordinate. The logarithmic law in Eq. 1 can therefore be applied in the *inner* region but with the addition of the parameter d, the displacement height, which expresses the upward displacement, due to the presence of obstacles, of the horizontal plane where the wind speed is assumed to be zero:

$$\frac{\overline{u}}{u_*} = \frac{1}{\kappa} \ln \frac{z-d}{z_0}. \tag{2}$$

On the other hand, the description of the flow field in the roughness sub-layer and canopy layer is much more complex. Many studies have been devoted to the analysis of wind blowing perpendicular to a canopy made of perpendicular streets (Fig. 3). In this case, a recirculating region generates behind the upwind buildings of the street and the flow is almost two-dimensional. Depending on the aspect ratio of the streets, i.e. the *height-to-width ratio* (H/W), three different flow regimes can be distinguished [Oke, 2002]. For wide streets ($H/W < 0.3$), the buildings act as isolated roughness elements (*isolated roughness regime*). At intermediate aspect ratios ($0.3 < H/W < 0.65$), the wakes generated by the single obstacles interact

and generate complex flow fields (*wake interference regime*). When the aspect ratio is high ($H/W > 0.65$), a single recirculating cell occupies the perpendicular street and the interaction between the flow inside the street and the atmosphere above is inhibited (*skimming flow regime*). For arbitrary wind directions with respect to the streets of the urban canopy, the flow field is much more complex and tends to exhibit spiral patterns [Soulhac et al., 2008].

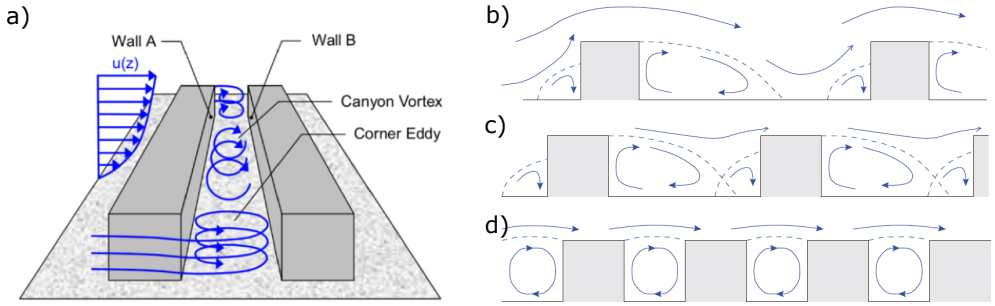

Figure 3: a) Three-dimensional flow field in a finite street canyon. From [Gromke and Ruck, 2007]. Different flow regime in a two-dimensional street canyon: b) isolated roughness, c) wake interference, d) skimming flow. From [Oke, 2002]. d)

To accurately model dispersion phenomena at the city-district scale, computational fluid dynamics (CFD) simulations can be adopted, as they solve the velocity and the concentration fields in the whole domain [Tominaga and Stathopoulos, 2012, Blocken, 2015]. However, when a district of hundreds of streets is considered, CFD codes require computational costs that are not yet feasible for operational purposes. To reduce the computational cost, different modelling approaches have been proposed in the last decades [Di Sabatino et al., 2013]. These include street network models [Carruthers et al., 2000, Soulhac et al., 2011] in which the atmospheric domain is decomposed in two sub-domain, the canopy layer and the atmosphere above. Above the canopy, where the flow field can be approximated with the logarithmic profile, the dispersion of pollutants is modelled using simple Gaussian models. In the canopy layer, instead, the geometry of the city is taken into account. The urban canopy is simplified as a network of street segments, in which the flow is driven by the longitudinal component of the external wind. To estimate pollutant concentration, each segment is considered as a box in which the pollutants are assumed to be uniformly mixed. The main transport mechanisms are parametrized, and pollutant concentration is obtained by means of a mass balance of the pollutant fluxes entering and leaving each street volume. These models evidenced that street level dynamics are much more complex to model than dispersion over buildings as they are governed by the geometry of the urban canopy.

The street scale

The street canyon is the fundamental unit of the urban fabric. It is the place where day-to-day activities of citizens occur but also the place where most of the airborne pollutants are released by vehicular traffic. Moreover, the street canyon is a low ventilated environment, due to the sheltering effect of lateral buildings. The proximity of the receptors to the sources and the high pollutant concentration make this environment extremely vulnerable and object of study on a higher resolution with respect to the city-district scale. A spatial scale of tens to hundreds of meters (the *street scale*) is necessary to analyse the spatial distribution of pollutant concentration within the canyon and to identify the regions with the highest pollution peaks.

For example (as will be presented in Chapter 5), when the wind is perpendicular to the street and the aspect ratio of the street canyon is sufficiently high to generate a skimming flow, concentration near the upwind wall of the canyon can be twice the concentration at the downwind wall. Street orientation, together with the canyon geometry, strongly influences the concentration of pollutants and their spatial distribution. However, the concentration field can drastically change due to thermal effects induced by solar radiation or dynamical effects caused by the presence of trees.

To simulate velocity and concentration fields at the scale of a single street canyon, CFD codes (RANS or LES) are widely used [Vardoulakis et al., 2003, Li et al., 2006]. However, numerical simulations present some issues when dealing with the treatment of boundary conditions (i.e. the canyon walls) and the reproduction of complex geometries, as for example porous and fractals element like vegetation. For this reason, experimental wind tunnel studies are fundamental for understanding flow and dispersion processes at this scale and for the validation of numerical simulations [Ahmad et al., 2005].

Clearly, the modeling scales analysed so far are not independent of each other. Conversely, each model at a specific scale requires boundary conditions and parameterizations obtained from analyses at a different resolution. A clear example is the case of operational models at the district/city scale. The wind forcing and air quality condition above the canopy are given by the results of regional scale models, while street scale studies provide parametrization for the typical exchange velocities (vertical and longitudinal) between a street canyon and the surrounding environment (the above atmosphere or the adjacent streets).

Content of this thesis

The elements presented in this chapter highlight the urgent need to provide tools to mitigate the fragility of cities to air pollution. This thesis aims to contribute to

this challenge by studying and modeling the dispersion of airborne pollutants at two different spatio-temporal scales.

The first part of the thesis, which includes Chapters 1-4, deals with the city-district scale and provides an innovative method to assess the vulnerability of an urban area to the release of harmful airborne pollutants. Going beyond the representation of the urban spatial domain as a street network, in the new proposed approach all the key variables involved in the dispersion process are viewed as properties of a complex network [Boccaletti et al., 2006, Newman, 2018]. Thanks to this mathematical interpretation, the modern techniques of the theory of complex networks can be adopted to efficiently simulate propagation phenomena in the streets as transport processes on a network. In this way, the most vulnerable locations in a city are promptly identified for multiple scenarios and the characteristics that make a city vulnerable to the spreading of airborne pollutants are investigated.

The second part of the thesis, which includes Chapters 5-6, deals with the street scale. By means of two experimental campaigns, we focus on the vertical mass exchange between a street canyon and the external flow. The aim is to understand how different properties of the canyon (its geometry, the characteristics of the lateral walls and the presence of vegetation) can affect the ventilation, and thus the concentration field, within the street.

Given the multiple scales involved in this thesis, different spatial and temporal averaging operators are used throughout the text for the velocity and concentration fields in a street canyon. We report here a brief summary for the fundamental notation. We will use x, y, z to denote respectively the transversal, longitudinal and vertical coordinates with respect to a local reference system for the street (see Fig. 4). u, v denote the components of the velocity vector $\mathbf{u}(x, y, z, t)$ along x and z, respectively. By adopting the Reynolds decomposition, the two components can be written as the sum of the ensemble average and the fluctuation component: $u = \langle u \rangle + u'$ and $v = \langle v \rangle + v'$. The instantaneous scalar concentration is $c_t(x, y, z, t)$, which can be written as the sum of the ensemble average $\langle c_t \rangle$ and the fluctuation component c'_t, namely: $c_t = \langle c_t \rangle + c'_t$. Note that $\langle c_t \rangle$, $\langle u \rangle$ and $\langle v \rangle$ may be a function of time if the turbulent flow is statistically unsteady. In the case of statistically steady flow, these ensemble averages coincide with the single-point time averages that we denote as $\overline{u}$, $\overline{v}$, and $\overline{c}$. We use $c(y, t)$ to indicate the spatial average over a transversal section of the street - i.e. in the (x, z) plane - for the ensemble averaged concentration $\langle c_t \rangle$. Similarly, the average over a generic volume within the street canyon is denoted as $C(t)$.

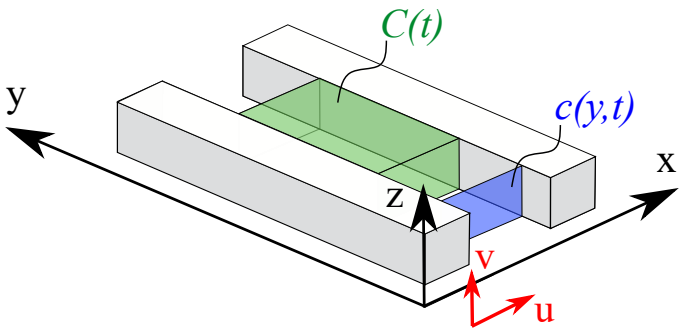

Figure 4: Schematic representation of a street canyon with the fundamental notation adopted in this thesis.

Part I

Complex network modelling of pollutant dispersion at the district scale

Introduction to Part I

Networks are ubiquitous in nature and in man-made systems. We, as human beings, are the results of a network of biochemical reactions (Fig. 5.a). Water flows over the Earth's surface shaping fascinating network patterns (Fig. 5.b). Even our work is based on networks: every time we send an email, or we share a file, we are exploiting the large network of computers that makes the Internet (Fig. 5.c). The fundamental property of networks is their structure, which describes how the elements of the system are interconnected. The nature of these interconnections can however change over time and may depend on a chain of consecutive actions [Artime et al., 2017]. For example, in a power transmission grid, the random breakdown of a power station (i.e. the removal of a node) results in a global redistribution of the power load over all the network that may trigger a cascade of overload failures [Boccaletti et al., 2006]. These dynamical behaviors are a characteristic feature of real-world networks, together with the non-trivial nature of their interconnections that are neither purely regular (as in lattices) nor purely random (as in Erdős-Rényi random networks). Networks showing these properties are called *complex networks* [Barabási et al., 2016, Newman, 2018].

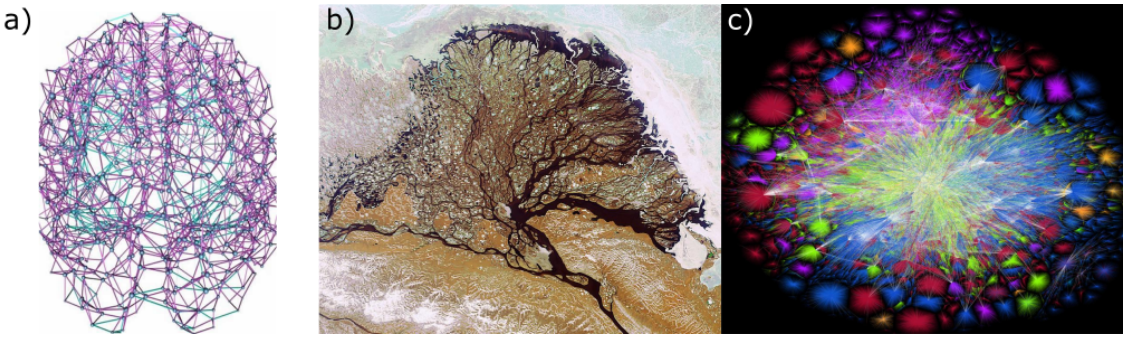

Figure 5: a) Structural network of the human brain [Gulyás et al., 2015]. b) River network from the Lena River Delta, Russia. Credit: Esa/Envisat, CC BY-SA 3.0 IGO. c) Visualization from the Opte Project [Lyon, 2015] of the Internet network in 2015. Links are connections between IP adresses. A different color is associated to each continent.

In the last two decades, the study of complex systems within a network perspective has dramatically expanded and scientists in a wide variety of fields, from the social sciences (e.g., [Borgatti et al., 2009]) to engineering and physics (e.g., [Albert et al., 2004, Rinaldo et al., 2006, Giustolisi et al., 2019]), have developed an extensive set of tools to analyse network structure and dynamics, contributing to the foundation of complex network theory. Besides the advantage of tracing complex systems to a clean and tractable model, the combination of traditional

fields of study with complex network theory has paved the way to multidisciplinary and inspiring research.

In this wake, the first part of this thesis proposes an innovative approach based on the theory of complex networks to investigate the vulnerability of cities to the release of airborne toxic substances in the urban atmosphere. The topic is highly multidisciplinary and includes aspects concerning (i) urban geometry, (ii) transport phenomena in fluid-flow systems and (iii) spreading dynamics. In previous literature, a complex network perspective has been proposed to analyse these three aspects individually.

The application of a network approach in urban science dates back to the 1960s, with visionary studies aimed at investigating the physical shape of cities [Larson and Odoni, 1981, Batty and Longley, 1994]. Network analysis in urban studies has been mostly based on an intuitive representation of the city as a network, with streets modeled as links and street intersections as nodes of the network. An interesting exception is the perspective adopted in Hillier's Space Syntax theory [Hillier and Hanson, 1989], where nodes are identified as street segments and edges represent street intersections. More recently, the studies of Porta et al. and Crucitti et al. [Porta et al., 2006, Crucitti et al., 2006] have proposed metrics from complex network theory to analyse the structural properties of cities, e.g. to identify the prominent urban routes or to distinguish planned from self-organized cities. Beyond the structural analysis, the network approach allows to investigate the dynamical properties of a city such as its spatial evolution, mobility patterns of citizens or socio-economic features, thus contributing to the development of a promising new science of cities [Batty, 2013, Barthelemy, 2016].

Recently, a network approach has been adopted for the description of geophysical flows, as tools from complex network theory proved to be suitable to uncover spatial and temporal patterns in the motion of particles in turbulent flows (e.g., [Scarsoglio et al., 2017, Schlueter-Kuck and Dabiri, 2017, Schneide et al., 2018] and [Iacobello et al., 2018, Iacobello et al., 2019a, Iacobello et al., 2019b]). We mention here the application of network theory to map flow fields into spatial networks. Relevant examples are *climate networks* [Tsonis et al., 2006, Donges et al., 2009], where nodes represent specific positions on the Earth's surface and links are activated on the basis of correlation in climatic variables (e.g., temperature, pressure). Similarly, in *flow networks* the nodes are specific positions of the fluid domain while links represent the material transport between these locations. Techniques from complex network theory give information about geophysical transport processes, as mixing and dispersion in the Mediterranean sea [Ser-Giacomi et al., 2015].

Interesting elements for our research also come from the field of *spreading dynamics on networks* [Newman, 2002]. Spreading describes many important phenomena in the real world, e.g., the dissemination of information and ideas in a society [Moreno et al., 2004], the rise of a political party [Polletta and Jasper, 2001], or the outbreak of an epidemic [Diekmann and Heesterbeek, 2000] These phenomena are based on the transmission of contents between elements of a group that come into contact. By associating these elements with the nodes of a network and their contact with links, transmission mechanisms can be investigated using tools from complex network theory. In spreading models, two fundamental elements must be specified [Pei and Makse, 2013]. The first is the underlying network, which describes how the elements are in contact with each other. The second is the model that regulates the transmission from one element to another. To this aim, compartmental models from epidemiology (e.g. the SIR model [Nåsell, 2002]) are widely adopted. Given the network model, many metrics [Erkol et al., 2019] have been proposed in literature to identify the best spreader nodes in a network.

In the following four chapters, we derive a network model to investigate the propagation of airborne pollutants in the urban atmosphere. The spatial representation of the urban fabric is the same adopted in the framework of urban science: streets and street intersections are represented as links and nodes of the network. The propagation of pollutants along a street recalls the concept of material transport between two nodes in *flow networks*. The most vulnerable locations in a city are identified as the best spreading nodes in the network, in analogy with the spreading of an epidemic. The aim is to provide a reliable and rapid technique to identify the most vulnerable location in a city, i.e. the source points from which a toxic spreading can affect the greatest number of people, and to understand the effect of meteorological conditions (namely wind direction) on the efficiency of gas propagation.

A brief description of the contents of the following chapters is reported below. In Chapter 1, we introduce the novel network perspective on urban air pollution. In Chapter 2, we propose an algorithm to delimit the most vulnerable locations of an urban areas in terms of potential for contamination and we compare the outcomes with a well-known dispersion model for urban air quality. In Chapter 3, a centrality metric, tailored on urban air pollution, for the detection of the best spreading nodes is formally presented. In Chapter 4, we investigate which properties of an urban area make it vulnerable to the release of airborne pollutants.

Chapter 1

The complex network perspective on urban air pollution

The work described in this chapter has been partially derived from [Fellini et al., 2019].

The dispersion of airborne pollutants in the urban atmosphere is a complex, canopy-driven process. The intricate structure of the city, the high number of potential sources, and the large spatial domain make it difficult to predict dispersion patterns, to simulate a great number of scenarios, and to identify the high-impact emission areas.

In this chapter, we show that these complex transport dynamics can be efficiently characterized by adopting a complex network approach. In Section 1.1, we first briefly recall some basic concepts from complex network theory which will be used throughout this thesis. Then, in Section 1.2, we introduce the physical assumptions adopted to model pollutant dispersion in the urban canopy. Finally, in Section 1.3, the network model is constructed.

1.1 Basic concepts of complex network theory

In the framework of network theory, complex systems are traced back to a set of entities, the network nodes, that interact with each other (Fig. 1.1.a). Interactions are represented as links between the nodes. Nodes and links can be abstract entities, such as in language networks where nodes are words and links represent their co-occurrence within a sentence [Solé et al., 2010], or tangible objects, such as a subway network of stations and lines. Network links may have weights that describe the strength, intensity, or capacity of the interactions (*weighted networks*). Moreover, links are directed (*directed network*) if the interaction between nodes is in one direction only (Fig. 1.1.b). For example, global trends in tourism are well described by a weighted and directed network, where links are travel routes

from country to country, and weights represent the number of tourists traveling. When nodes and edges are embedded in space, the network is defined as a *spatial network* [Barthélemy, 2011]. The topology of spatial networks is strongly limited by geographical constraints and two distant nodes are less likely to be connected.

Mathematically, the network is defined as a pair $\mathcal{G}(\mathcal{S}, \mathcal{E})$, where $\mathcal{S}$ is the set of network nodes and $\mathcal{E}$ is the set of links. A convenient way to represent the connectivity structure of the network is the *adjacency matrix*. Given a network of N nodes, its adjacency matrix $\mathbf{A}$ is a $N \times N$ square matrix whose element A_{ij} is equal to 1 if a link between node i and node j exists, is equal to 0 otherwise, namely:

$$A_{ij} = \begin{cases} 1, \text{if nodes } \{i, j\} \text{ are linked, with } i \neq j \\ 0, \text{otherwise} \end{cases} \tag{1.1}$$

The set of nodes that are adjacent to node i (i.e. nodes j such that $A_{ij} = 1$) constitutes the *first neighborhood* of this node. In undirected networks $\mathbf{A}$ is symmetric, while in directed networks the links are not bidirectional and the adjacency matrix is asymmetric. When the links are weighted, the *weight matrix* $\mathbf{w}$ is used instead of $\mathbf{A}$ (Fig. 1.1.c). The entry w_{ij} not only indicates the presence of a link between node i and node j but also quantifies the weight associated with the connection.

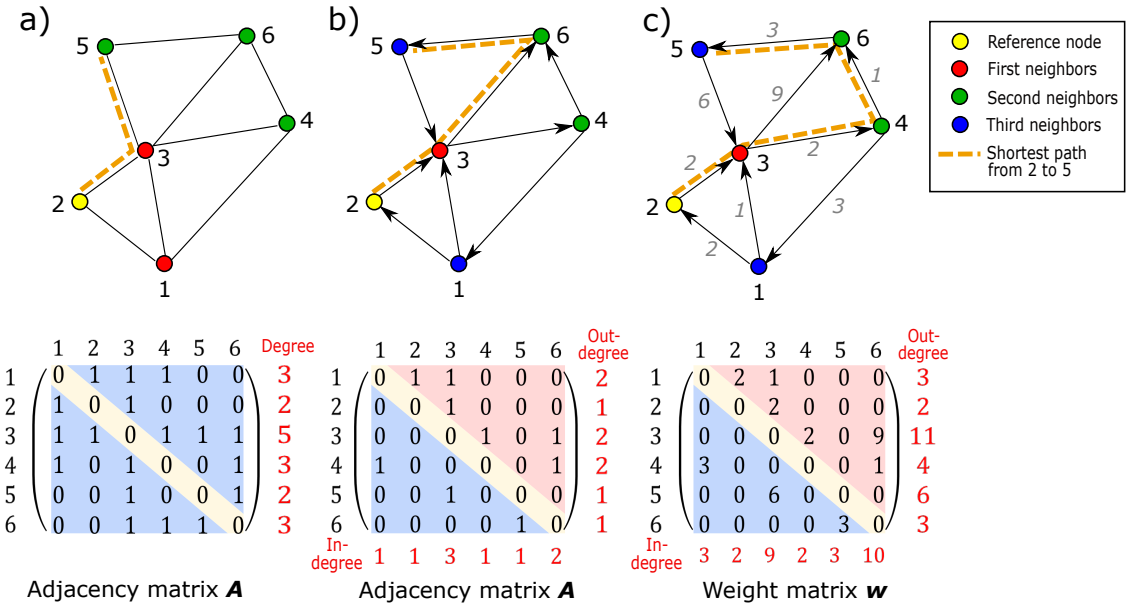

Figure 1.1: Example of a simple a) *unweighted* and *undirected network*, b) *unweighted* and *directed network*, and c) *weighted* and *directed network*. For each network, the adjacency or weighted matrix is reported.

Another feature to describe complex network topology is the concept of reachability. Two nodes i and j that are not directly connected, i.e. $A_{ij} = 0$, can still be reachable from one to another by traversing part of the network. A *walk* from i to j is a sequence of links that lead from node i to node j. If each node is visited only once, the walk is defined as a *path* ($\mathcal{P}$). As multiple paths can connect two nodes, the path with minimum number of links or minimum sum of link weights (in the case of weighted networks) is called *shortest path* ($\mathcal{D}$) (see examples in Fig. 1.1). Going back to the concept of node neighborhood, we can now state that a generic node j belongs to the *n-th neighborhood* (or *n-hop neighborhood*) of a node i if the shortest path from i to j is composed by n links. Algorithms for finding the shortest paths are widely used in many fields. A typical example is their implementation in journey planning applications to discover real-time shortest path for drivers [Abraham et al., 2010].

Given the network representation of a complex system, a crucial ability of network analysis is the identification of the most important nodes. Typical applications include the identification of the key transmission stations in a power grid, the most influential people in a social network, or the superspreaders during epidemics [MacKenzie, 2020]. The answer to these issues is given in terms of *centrality*, which can be defined as a function that associates to each node of the network a real value that allows a ranking of the nodes. As suggested by the examples above, the "importance" of a node has a wide variety of interpretations. For these reason, many centrality metrics have been proposed in the framework of complex network science [Newman, 2010]. Each metric defines the centrality of a node on the basis of particular topological properties, such as the number of its first neighbors (*degree centrality*) or the number of shortest paths passing across the node (*betweenness centrality*). For exemplary purposes, we report in Fig. 1.1 the calculation of the *degree centrality* for the different networks. For undirected and unweighted networks (panel a), the *degree* of a node is defined as:

$$\varkappa_i = \sum_{j \in \mathcal{S}} A_{ij}. \tag{1.2}$$

For weighted networks, the adjacency matrix is replaced with the weight matrix. Finally, for undirected networks, the degree of a node can be referred to the connections coming towards the node (*in-degree centrality*) or to those directed away from from the node (*out-degree centrality*). Mathematically, we define the in-degree and the out-degree of a node as:

$$\varkappa_i^{in} = \sum_{j \in \mathcal{S}} A_{ji}, \qquad \varkappa_i^{out} = \sum_{j \in \mathcal{S}} A_{ij}. \tag{1.3}$$

1.2 Physical assumptions for pollutant transport in a street network

Transport and mixing processes in the urban atmosphere are characterized by complex fluid structures due to the interaction between the atmospheric flow and the city. The presence of buildings and vegetation highly affects the structure of the urban boundary layer, characterized by the generation of a shear layer at the top of the canopy, wake diffusion behind buildings, and form drag due to the pressure differences across the roughness elements [Roth, 2000]. Moreover, the flow field in the streets is altered by the convective fluxes due to the differential solar irradiance on building walls and to the heat sources related to human activities [Oke, 1982, Arnfield, 2003]. The simulation of all these dynamical effects on the flow field within the urban canopy is nowadays a challenge for modellers that adopt sophisticated computational tools, typically CFD codes [Tominaga and Stathopoulos, 2012]. These require a huge amount of input data and high computational costs, which limit their use when analysing a large number of emission scenarios. In this latter case, alternative simulation strategies should be adopted, based on a simplified description of the flow and of the dispersion phenomena occurring within the urban area.

The physical assumptions for the propagation model presented in this work are inspired by the street network model approach (e.g., [Namdeo and Colls, 1996, Soulhac et al., 2011]). In street network models, the geometry of the urban canopy is simplified to a network of streets (Fig. 1.2.a), and the streets are represented as urban canyons, i.e. cavities of rectangular section with length L, height H and width W (Fig. 1.2.b). Following the approach of [Soulhac et al., 2011], the main transport phenomena for an airborne pollutant in the urban canopy are (i) the advective mass transfer along the street due to the mean wind along the longitudinal axis, (ii) the vertical transfer from/toward the external atmosphere and (iii) the transport at street intersections. In street network models, pollutant dispersion is then described by a series of mass balance equations within streets, at street intersections and above the urban canopy. This system of equations is numerically solved to evaluate pollutant concentrations within the streets and above them.

The objective of this work is to assess the vulnerability of urban areas to toxic releases by identifying the extension of the contaminated areas from pollutant sources located in the urban tissue. To this aim, a detailed quantification of the concentration in the streets and in the street intersections is generally not required. Rather, an operational model based on few input data and with very low computational cost is sought, so that it can be easily and quickly implemented for the assessment of large city vulnerability, even in emergency situations. For these reasons, numerical solution of mass balance equations and the estimation of a large number of physical parameters are here avoided. Conversely, we introduce an analytical solution for

dispersion along a street canyon, we adopt a simplified model for propagation in street intersections and we use concepts from complex network theory to simulate toxic spreading from one street to the adjacent ones. To this aim, further simplifications are required compared to those adopted in well-known street network models (e.g., [Soulhac et al., 2011]). These simplifications concern the physico-chemical processes of pollutants in the street canyons, vertical transfers between the canyon and the atmosphere, and pollutant fluxes in the intersections.

In the following, the transport mechanisms along a street canyon and at street intersections are described in detail. The adopted physical assumptions are introduced and discussed. The emission scenario consists of a release from a point source (s in Fig. 1.2) at ground level within the urban canopy. The external wind blowing on the city with direction Φ is the driving force for the propagation process.

1.2.1 Transport in a street canyon

Consider a street canyon with height H, length L and width W (Fig. 1.2.b). The coordinates x, y and z of a local reference system indicate the transversal, longitudinal and vertical directions with respect to the street. At the beginning of the street ($y = 0$), a source s releases a gaseous pollutant, as illustrated in Fig. 1.2.b-c. As a first approximation, the pollutant can be modeled as a passive scalar, since the physico-chemical processes are generally characterized by longer time scales than the time needed for propagation.

The transport of a passive scalar in a turbulent flow field is described by the advection-diffusion equation:

$$\frac{\partial c_t}{\partial t} + \frac{\partial}{\partial x_j}\left(u_j c_t\right) = \frac{\partial}{\partial x_j}\left(D_m \frac{\partial c_t}{\partial x_j}\right) \tag{1.4}$$

where $c_t(x, y, z, t)$ is the concentration field as a function of time (t), and of the transversal (x), longitudinal (y) and vertical (z) coordinates. $u_j(x, y, z, t)$ are the components of the velocity vector $\mathbf{u}(x, y, z, t)$, and D_m is the mass diffusivity. Neglecting molecular diffusion and applying the Reynolds average operator, we obtain:

$$\frac{\partial \langle c_t \rangle}{\partial t} + \frac{\partial \langle u_j c_t \rangle}{\partial x_j} = 0, \tag{1.5}$$

where the brackets indicate the ensemble average. $\langle u_j c_t \rangle$ is the flux of the passive scalar in the $j-th$ direction, given by the turbulent and mean transport: $\langle u_j c_t \rangle = \langle u_j \rangle \langle c_t \rangle + \langle u_j' c_t' \rangle$.

According to previous literature [Soulhac et al., 2013], the main transport processes in a street canyon are the flux along the longitudinal axis due to the mean wind, and the vertical flux between the street and the external atmosphere (Fig. 1.2.b). Under these assumptions, we neglect the transport along the transversal

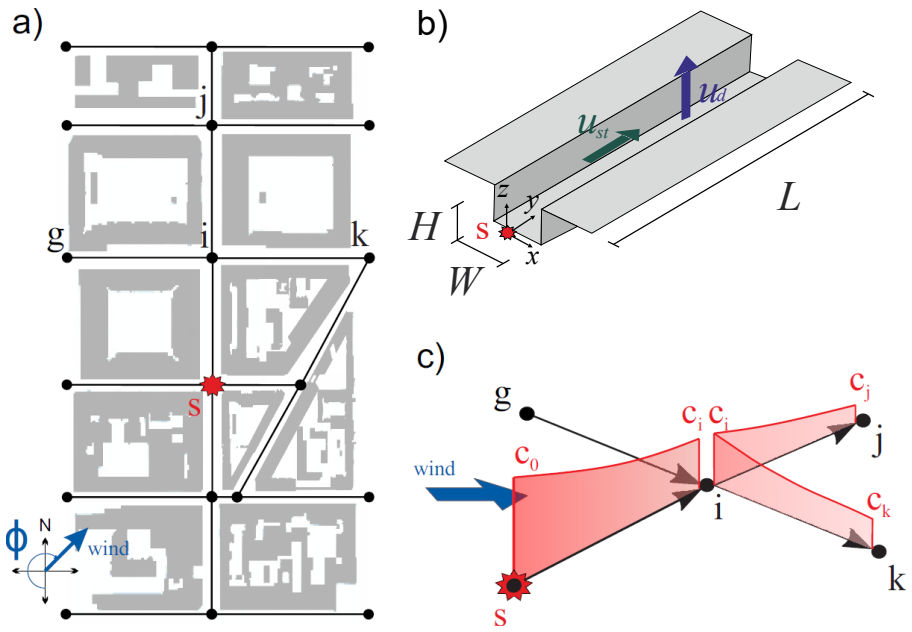

Figure 1.2: a) Toxic source s within a network of streets. Propagation is driven by the wind blowing on the city with direction Φ. b) Representation of a street canyon with the main variables of the model. c) Transport of a contaminated flow in street intersections.

direction (x) and we average Eq. 1.5 over x and z. Moreover, we consider that the turbulent longitudinal diffusion is marginal compared to the longitudinal transport given by the mean flow. In this way, we obtain:

$$HW\frac{\partial c}{\partial t} + HWu_{st}\frac{\partial c}{\partial y} + \int_0^W \left[\langle vc_t\rangle\right]_{z=H} dx = 0, \tag{1.6}$$

where H and W are the height and the width of the street canyon, $c = c(y,t)$ is the average concentration over a transversal section of the street (see Fig. 4), u_{st} is the spatially averaged wind velocity along y, v is the vertical velocity. The last term in Eq. 1.6 results from integration along the z coordinate of the vertical pollutant flux. At $z = 0$ the flux is assumed equal to 0, while its value is non-negligible at roof level ($z = H$) where the exchange with the external flow takes place.

Following [Soulhac et al., 2013], we now introduce a parametrization for the vertical flux at roof level. Considering the entire volume of the street canyon, the vertical flux at roof level can be parametrized as the product of a bulk exchange velocity u_d and the difference between the concentration within the canyon (C) and the concentration in the external flow (C_{ext}).

$$u_d(C - C_{ext})WL = \int_0^L \int_0^W \left[\langle vc_t\rangle\right]_{z=H} dxdy, \tag{1.7}$$

where C and C_{ext} refer to concentration averaged over volumes and L is the total length of the canyon. For an infinitesimal length along the y direction we can write:

$$u_d(c - C_{ext})W = \int_0^W \left[\langle v c_t \rangle\right]_{z=H} dx. \tag{1.8}$$

Introducing Eq. 1.8 in Eq. 1.6, we finally obtain the one-dimensional transport equation

$$\frac{\partial c}{\partial t} + u_{st}\frac{\partial c}{\partial y} + \frac{u_d}{H}(c - C_{ext}) = 0, \tag{1.9}$$

whose solution is the function $c(y,t)$, i.e. the concentration along the longitudinal coordinate y over time t.

The first two terms in Eq. 1.9 describe the transport driven by the spatially averaged wind velocity along y (u_{st}). This velocity is assumed to be given by a balance between the stress imposed at the canopy top by the external atmospheric flow and the drag due to the roughness of the canyon walls (neglecting the role of pressure gradients). Under this assumption, [Soulhac et al., 2008] derived an analytical formulation for u_{st}:

$$\begin{aligned} u_{st} = \upsilon \cos\theta \frac{G^2}{HW}\Bigg[\frac{2\sqrt{2}}{\mathcal{F}}(1-\varrho)\left(1 - \frac{\mathcal{F}^2}{3} + \frac{\mathcal{F}^4}{45}\right) + \varrho\frac{2\varsigma - 3}{\varsigma} \\ + \left(\frac{W}{G} - 2\right)\frac{\varsigma - 1}{\varsigma}\Bigg] \end{aligned} \tag{1.10}$$

$$\text{with} = \begin{cases} \varsigma = \ln\left(\frac{G}{z_{0,build}}\right) \\ \varrho = \exp\left[\frac{\mathcal{F}}{\sqrt{2}}\left(1 - \frac{H}{G}\right)\right] \\ \upsilon = u_* \sqrt{\frac{\pi}{\sqrt{2}\kappa^2\mathcal{F}}\left[Y_0(\mathcal{F}) - \frac{J_0(\mathcal{F})Y_1(\mathcal{F})}{J_1(\mathcal{F})}\right]} \\ \mathcal{F} \text{ solution of } \frac{z_{0,build}}{G} = \frac{2}{\mathcal{F}}\exp\left[\frac{\pi}{2}\frac{Y_1(\mathcal{F})}{J_1(\mathcal{F})} - \gamma_E\right] \\ G = \min\left(H, \frac{W}{2}\right) \end{cases} \tag{1.11}$$

where θ is the angle between the external wind and the longitudinal axis of the street, H and W are the height and the width of the street canyon, $z_{0,build}$ is the aerodynamic roughness of the canyon walls, u_* is the friction velocity of the external atmospheric boundary layer flow, J_0, J_1, Y_0 and Y_1 are Bessel functions, κ is the von Kármán constant, and γ_E is the Euler constant. The friction velocity u_* is determined using the Monin-Obukhov similarity theory to model the flow in the external boundary layer.

The third term in Eq. 1.9 models the mass transfer from/to the canyon to/from the overlying atmosphere by means of the bulk exchange velocity u_d. The velocity u_d represents an integral variable which depends on all features characterizing the

flow within the reference volume. Thus, we expect this velocity to depend on the dynamical conditions of the external flow and on the geometrical characteristics of the street canyon. As a first approximation, we adopt here the model proposed by [Salizzoni et al., 2009] which takes into account only the dependence of u_d on the external flow:

$$u_d = \frac{u_*}{\sqrt{2}\pi}. \tag{1.12}$$

The second part of this thesis will analyse the effect of the geometric and thermal characteristics of the canyon walls on this exchange velocity. In this regard, we underline that the specific physical models adopted here for u_{st} and u_d could be easily replaced if better ones become available. Moreover, a simple model for physico-chemical transformation could be easily implemented in Eq. 1.9 by adding a physico-chemical transformation rate to the exchange velocity u_d.

Since our focus is on a localized ground-level release only - therefore inducing maximal concentration at the street level -, we will assume that the vertical flux of pollutants from the canopy to the external atmosphere will induce significantly low concentrations, C_{ext}, above roof level, due to the high dilution occurring in the lower part of the boundary layer compared to that within the streets. As a consequence, we will consider that $c - C_{ext} \simeq c$, therefore ignoring the role of any re-entrainment of mass from the external flow to the streets. The effects of re-entrainment have been discussed by many authors [Hamlyn et al., 2007, Belcher et al., 2015, Goulart et al., 2018]. Their studies highlighted that re-entrainment effects are physically significant in the so called far-field region, i.e. the region extending from the third intersection downwind the source. However, the vertical flux is in general less than a quarter of the horizontal advective flux [Goulart et al., 2018]. For these reasons, the possible inclusion of re-entrainment effects in the model is not expected to bring significant improvements to the results. Under the assumption that C_{ext} is negligible with respect to the concentration in the street canyon, the one-dimensional transport equation 1.9 becomes

$$\frac{\partial c}{\partial t} + u_{st}\frac{\partial c}{\partial y} + \frac{u_d}{H}c = 0. \tag{1.13}$$

By introducing the substitution

$$g(y,t) = c(y,t)\exp\left(\frac{u_d}{H}t\right), \tag{1.14}$$

Eq. 1.13 yields

$$\frac{\partial g}{\partial t} + u_{st}\frac{\partial g}{\partial y} = 0. \tag{1.15}$$

The general solution for Eq. 1.15 is found by introducing the new coordinates $\tau = t$, $\xi = y - u_{st}t$ and using the chain rule:

$$\frac{\partial g(y,t)}{\partial t} = \frac{\partial g(\xi,\tau)}{\partial \tau} - u_{st}\frac{\partial g(\xi,\tau)}{\partial \xi} \tag{1.16}$$

$$\frac{\partial g(y,t)}{\partial y} = \frac{\partial g(\xi,\tau)}{\partial \xi}. \tag{1.17}$$

Equation 1.15 becomes

$$\frac{\partial g(\xi,\tau)}{\partial \tau} = 0, \tag{1.18}$$

and, therefore,

$$g(\xi,\tau) = F(\xi) \quad \rightarrow \quad g(y,t) = F(y - u_{st}t), \tag{1.19}$$

where F is a derivable function. The solution of Eq. 1.13 is obtained returning to the original function,

$$c(y,t) = g(y,t)\exp\left(-\frac{u_d}{H}t\right) = F(y - u_{st}t)\exp\left(-\frac{u_d}{H}t\right). \tag{1.20}$$

Function F is found using the initial or boundary conditions of the problem.

For a continuous release at the source node starting from $t \geq 0$, the boundary condition is defined as

$$c(0,t) = c_0\vartheta(t), \tag{1.21}$$

where ϑ is the Heaviside function and c_0 is the constant concentration at the source. For $y = 0$, Eqs. 1.20 and 1.21 yield

$$c(0,t) = F(-u_{st}t)\exp\left(-\frac{u_d}{H}t\right) = c_0\vartheta(t). \tag{1.22}$$

Function F is obtained from the previous one and the solution for the continuous release is thus

$$c(y,t) = F(y - u_{st}t)\exp\left(-\frac{u_d}{H}t\right) = c_0\exp\left(-\frac{u_d}{u_{st}}\frac{y}{H}\right)\vartheta\left(t - \frac{y}{u_{st}}\right). \tag{1.23}$$

The solution is a front that spreads along the street with velocity u_{st}.

For a quick release in the source node, the initial condition is set as a rectangular pulse with width a and height c_0:

$$c(y,0) = c_0[\vartheta(y) - \vartheta(y - a)]. \tag{1.24}$$

When a tends to zero, the release is almost instantaneous. Following the same reasoning as in Eqs. 1.22 and 1.23, but considering this time $t = 0$, we obtain the solution for a quick release:

$$c(y,t) = c_0\exp\left(-\frac{u_d}{H}t\right)[\vartheta(y - u_{st}t) - \vartheta(y - u_{st}t - a)]. \tag{1.25}$$

The solution describes the initial concentration step travelling along the street with velocity u_{st} and undergoing an exponential decay of concentration.

Although the analytical solutions 1.23 and 1.25 are different, the concentration at the end of the street ($y = L$) in both cases is the same:

$$c_L\left(y = L, t = \frac{L}{u_{st}}\right) = c_0 e^{-\frac{L}{u_{st}}\frac{u_d}{H}}. \tag{1.26}$$

Thus, the concentration at the beginning of the street (c_0) undergoes an exponential decay driven by the ratio between the longitudinal advection time (L/u_{st}) that the toxic front spends to reach the end of the street, and the vertical transfer time (H/u_d). The terms in the exponent summarize all the information about the geometry of the canyon and the flow dynamics in it.

1.2.2 Transport in street intersections

The flow field in the street intersections is driven by complex physical processes that depend on multiple geometrical and meteorological parameters. Several studies (e.g., [Hunter et al., 1990, Robins et al., 2002, Soulhac et al., 2009]) have demonstrated that even slight variations in the building geometry and wind direction can affect significantly the redistribution of the incoming fluxes over the outgoing fluxes. On the basis of these observations, *Soulhac et al.* have developed a model, quantifying the balance of the time-averaged incoming and outgoing fluxes at the street intersection [Soulhac et al., 2009]. This model requires the estimation of exchange coefficients between the streets, and the formulation of a mass balance equation for each intersection. In street network models (e.g., SIRANE), these balance equations are solved numerically together with the equations for transport along the canyons.

As mentioned in Section 1.2, our aim is to identify the contaminated area from a pollutant source by means of a simplified methodology that simulates propagation as a spreading process on a network. In order to adopt this approach, an analytical solution for the physical transport mechanisms is required. For these reasons, we define a simple exchange model in the intersections that avoids the use of mass balance equations. Given the uncertainty of flow redistribution in street intersections, a conservative approach is adopted in developing this minimalistic model.

Consider a simple intersection with a single incoming and one outgoing street canyon. The volumetric air flow rate entering the intersection with a concentration c_{in} is Q_{in}, while the volumetric air flow rate outgoing the intersection with a concentration c_{out} is Q_{out}. Two cases are possible for the mass balance in the intersection. In the first case, the mass flow rate from the incoming canyon ($\dot{m}_{in} = c_{in}Q_{in}$) is

lower than the mass flow rate toward the outgoing canyon ($\dot{m}_{out} = c_{out}Q_{out}$). In order for the mass balance to be satisfied, an external mass flow rate ($\dot{m}_{ext}$) from the atmosphere above the canopy enters the intersection vertically with a volumetric air flow rate Q_{ext} and a concentration c_{ext}, so that

$$\dot{m}_{in} + \dot{m}_{ext} = \dot{m}_{out} \rightarrow c_{in}Q_{in} + c_{ext}Q_{ext} = c_{out}Q_{out}. \tag{1.27}$$

In Section 1.2.1, we stated that re-entrainment from the atmosphere is negligible in our model. Thus, the mass flow rate from the atmosphere makes a zero contribution in Eq. 1.27. The concentration c_{out} at the beginning of the street outgoing the intersection is therefore given by $c_{out} = c_{in}Q_{in}/Q_{out}$. As the volumetric flow rate balance in the intersection is $Q_{in} + Q_{ext} = Q_{out}$, the ratio Q_{in}/Q_{out} is lower than 1 and thus $c_{out} < c_{in}$. In the second case, $\dot{m}_{in} > \dot{m}_{out}$ and the mass flow rate $\dot{m}_{ext}$ leaves the intersection vertically, in order for the mass balance to be satisfied:

$$\dot{m}_{in} = \dot{m}_{ext} + \dot{m}_{out} \rightarrow c_{in}Q_{in} = c_{ext}Q_{ext} + c_{out}Q_{out}. \tag{1.28}$$

We consider that the concentration leaving the intersection is the same for both the upwards flow and the flow towards the outgoing street canyon, i.e. $c_{ext} = c_{out}$. Applying Eq. 1.28 and the volumetric flow rate balance equation ($Q_{in} = Q_{out} + Q_{ext}$), we find that $c_{out} = c_{in}$.

These arguments show that in the case of an intersection with a single incoming and one outgoing street canyon, the concentration c_{out} is equal or lower than the concentration c_{in}.

Let's now consider an intersection with two incoming streets (street 1 and 2), and a single outgoing street. The volumetric air flow rates from streets 1 and 2 are Q_1 and Q_2. Their concentration are c_1 and c_2. The outgoing street is characterized by a flow rate Q_{out} and a concentration c_{out}. Following the same steps as above, when the total incoming mass flow rate $c_1Q_1 + c_2Q_2$ is lower than the mass flow rate outgoing the canyon $c_{out}Q_{out}$, an external mass flow rate enters the intersection vertically. The mass and volumetric flow rate read:

$$c_1Q_1 + c_2Q_2 + c_{ext}Q_{ext} = c_{out}Q_{out} \tag{1.29}$$

$$Q_1 + Q_2 + Q_{ext} = Q_{out}. \tag{1.30}$$

Neglecting the re-entrainment from the atmosphere above and setting $c_1 = \alpha c_2$ with $\alpha < 1$ (i.e. street 2 has the highest concentration), we have:

$$\frac{c_{out}}{c_2} = \frac{\alpha Q_1 + Q_2}{Q_{out}} \tag{1.31}$$

$$Q_1 + Q_2 < Q_{out}. \tag{1.32}$$

From these equations we obtain that $c_{out} < c_2$. When the total incoming mass flow rate is greater than the mass flow rate outgoing the canyon, the mass flow rate $\dot{m}_{ext}$

leaves the intersection vertically, and the balances read:

$$c_1 Q_1 + c_2 Q_2 = c_{out} Q_{out} + c_{ext} Q_{ext} \tag{1.33}$$
$$Q_1 + Q_2 = Q_{out} + Q_{ext}. \tag{1.34}$$

Assuming $c_{ext} = c_{out}$ and writing c_1 as a function of c_2, we find:

$$\frac{c_{out}}{c_2} = \frac{\alpha Q_1 + Q_2}{Q_{out} + Q_{ext}} \tag{1.35}$$
$$Q_1 + Q_2 = Q_{out} + Q_{ext}, \tag{1.36}$$

and again $c_{out} < c_2$.

These simple arguments suggest that in the case of an intersection with two incoming and one outgoing street canyon, the concentration c_{out} is lower than the maximal incoming concentration. The same result can be obtained for a higher number of incoming streets.

Given these considerations, in our model we assume that the concentration of pollutants at the beginning of the streets outgoing the intersection corresponds to the maximal concentration in the incoming contaminated canyons. This is a conservative approach.

In the case of several streets outgoing the intersection, we assume that when a contaminated puff with concentration c_{in} reaches the intersection, then the concentration at the beginning of the streets exiting the intersection is c_{in}. According to this assumption, we consider that when a contaminated flow reaches the intersection, it does not divide between the different outgoing streets but tends to spread towards one of them. Given the uncertainty associated with the trajectory taken by the pollutant puff [Scaperdas, 2000], we consider all the possible statistical realizations, and thus we assume that all the outgoing streets are contaminated by the incoming concentration c_{in}.

The assumptions adopted for the transport in street intersections are clearly illustrated in Fig. 1.2.c. The contaminated flow from street (s, i) propagates towards streets (i, j) and (i, k). According to this scheme, the concentration at the beginning of streets (i, j) and (i, k) is the one at the end of street (s, i).

1.3 The network construction

According to these propagation laws, the gas emitted at the point source spreads through the urban canopy driven by the direction of the external wind, while undergoing an exponential decay in concentration with distance from the source. The

street canyons behave thus like upward leaking transport channels and their geometry, position and connectivity strongly influence the propagation. In big cities, streets cross each other to compose intricate patterns (Fig. 1.3). Given the spatial extent and the high number of elements, these urban fabrics can be seen as complex networks [Porta et al., 2006, Barthélemy, 2011]. Links stand for the street canyons, while nodes represent the street intersections. The direction and the weight of the links describe the geometrical and fluid-dynamical properties of the street canyons. Within this approach, the tools of network theory provide interesting information about the propagation phenomena.

The urban canopy is modelled as a directed and weighted network $\mathcal{G}(\mathcal{S},\mathcal{E},\mathbf{w})$, with node-set $\mathcal{V}$, edge-set $\mathcal{E}$ and weight matrix $\mathbf{w}$ (the formulation of link weight is discussed in Chapter 3). N and M are the numbers of nodes (intersections) and links (streets), respectively. Fictitious nodes can be created to divide a street into two links in case there is a significant change in the street properties. Each link is directed according to the orientation of the mean wind along the street (u_{st}). Thus, the network structure represents both the topological properties of the urban fabric and the directions in which the propagation processes take place. The connectivity of the street canyons is described by a $N \times N$ adjacency matrix $\mathbf{A}$. As an example, consider the network in Fig. 1.2.c, extracted as a subgraph from the network of streets in Fig. 1.2.a. The adjacency matrix of this simple four-links graph reads

$$\mathbf{A} = \begin{array}{c} \\ s \\ g \\ i \\ j \\ k \end{array} \begin{array}{c} \begin{array}{ccccc} s & g & i & j & k \end{array} \\ \begin{pmatrix} 0 & 0 & 1 & 0 & 0 \\ 0 & 0 & 1 & 0 & 0 \\ 0 & 0 & 0 & 1 & 1 \\ 0 & 0 & 0 & 0 & 0 \\ 0 & 0 & 0 & 0 & 0 \end{pmatrix} \end{array}. \tag{1.37}$$

Since the links have a specific direction, the adjacency matrix is asymmetric.

According to this network representation, the geometry and fluid-dynamical properties of the street canyons are stored efficiently in matrices. $\mathbf{L}$ and $\mathbf{H}$ are the symmetrical matrices of the length of the streets (L) and the average height of the buildings overlooking the streets (H). The wind velocity along the streets (u_{st}) and the velocity of the vertical transfer towards the external atmosphere (u_d) are enclosed in matrices $\mathbf{U_{st}}$ and $\mathbf{U_d}$. Moreover, $\mathbf{P}$ is the matrix that associates at each link the number of inhabitants per unit street length.

An interesting advantage of this compact notation is that changes to the network properties can be easily implemented. By modifying matrices $\mathbf{U_{st}}$ and $\mathbf{U_d}$, we can simulate different meteorological scenarios, while variations in population distribution (e.g., differences between weekdays and holidays) can be considered by adjusting $\mathbf{P}$. Furthermore, new buildings and structural changes are included in the model by revising the single elements of $\mathbf{L}$ and $\mathbf{H}$.

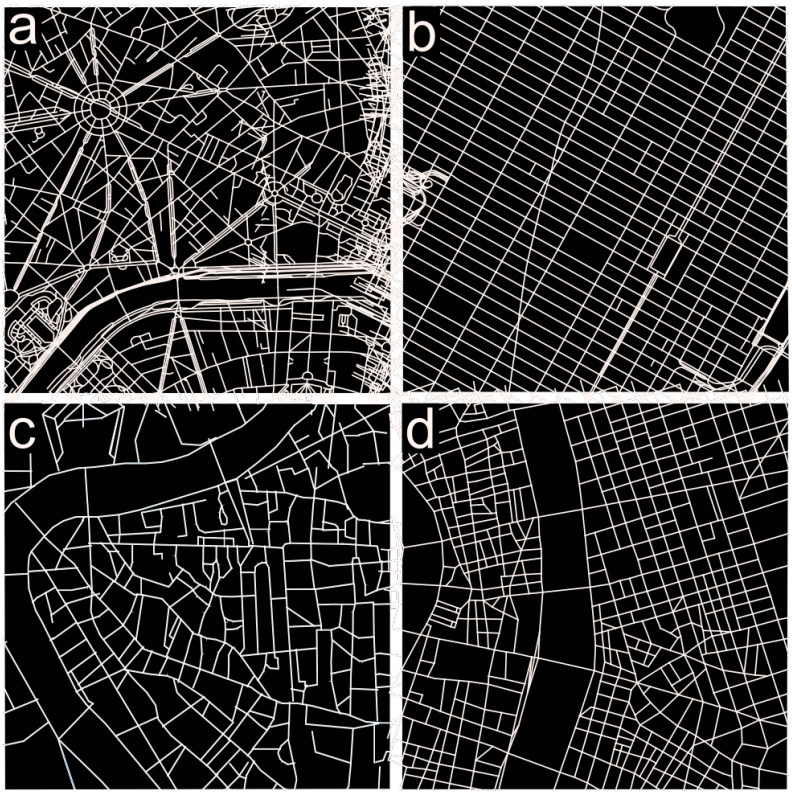

Figure 1.3: Snapshot of the street network of Paris (a), New York (b), Rome (c), and Lyon (d).

Chapter 2

Vulnerability and zone of influence of a source node

The work described in this chapter has been partially derived from [Fellini et al., 2019].

For the assessment of urban fragility to the release of toxic gases, we introduce the concept of zone of influence of a source node and a vulnerability index associated to each node of the street network.

The zone of influence $\mathcal{Z}_s$ for a generic node s is the set of links in a network that are contaminated with significant concentration, i.e. with concentration above a predefined threshold c_{th}, if the release takes place in s. The vulnerability index ($\mathcal{V}_s$) of node s is defined as the number of people affected by the toxic propagation. The network approach and matrix notation presented in Chapter 1 make it easy to calculate $\mathcal{V}_s$ as follows,

$$\mathcal{V}_s = \sum_{i}^{N} \sum_{j}^{N} Z_{ij} P_{ij}, \tag{2.1}$$

where $\mathbf{P}$ is the matrix that associates at each link (i, j) the number of inhabitants per unit street length and $\mathbf{Z}$ is the matrix that associates at each link (i, j) the contaminated length of the street. According to the definition of $\mathcal{Z}$, the matrix $\mathbf{Z}$ has non-zero values only for the links belonging to the zone of influence, i.e. for $(i, j) \in \mathcal{Z}$, and represents the extent of the contamination. Notice that, under the assumption of uniform residential density, the total length of the streets in the zone of influence is a good index for the danger associated with the source.

Given these definitions, we propose in this chapter a search algorithm on networks to delimit the zone of influence of a source node. By counting the number of people that reside in the zone of influence, the vulnerability index of the source node is estimated. The procedure is applied to each node of the network and vulnerability maps are constructed in order to reveal at a glance the urban areas with the

highest spreading potential. Finally, the model outcomes are compared with the results obtained from SIRANE, a well-known dispersion model for the simulation of urban air pollution.

2.1 Propagation as spreading on a network

Consider the release of a toxic substance in a street intersection (see Fig. 2.1.a). According to the hypotheses of our model (Section 1.2), (i) the substance propagates along the adjacent streets depending on the direction of the wind, (ii) the concentration decays exponentially along the streets, (iii) the concentration at the end of each street can be estimated using Eq. 1.26, (iv) the concentration remains unchanged in the street intersections, and (v) from a contaminated street intersection the gas spreads further to the adjacent streets.

Given this description, pollutant dispersion within the canopy can be easily seen as a spreading process on a network [Comin and da Fontoura Costa, 2011]. In Fig. 2.1.b the urban canopy is represented as a network. The links are directed according to the direction of the wind in the streets and the release is modelled as a source node s. From a network perspective, transport from s towards a generic node f is possible if there is a link directed from s to f, i.e. if (i) the two nodes are physically connected by a street canyon, and (ii) the wind is blowing from the source towards the target node. Once infected, the target node f is modelled as a new source and the spreading process carries on towards the farthest nodes. According to this scheme, propagation is a recursive process that spontaneously expands to the topological boundaries of the network. Physically, the extent of the contaminated zone can be delimited based on a threshold concentration value c_{th}: when the concentration falls below c_{th}, the contamination process is irrelevant. Thus, a stopping rule for the spreading process on the network is introduced: at each propagation hop the concentration at the target node is estimated. If this concentration is higher than c_{th}, then the propagation carries on.

Considering the example in Fig. 2.1.b, a toxic substance is released in the source node $s = 15$ and propagates towards the first neighbours of s: nodes 10, 11, and 16. The concentration in the first neighbours is evaluated using Eq. 1.26, as a function of the geometrical and wind characteristics of the street canyons associated to links (15,10), (15,11) and (15,16). Since the concentration in the first neighbours is grater than the predefined threshold c_{th}, nodes 10, 11 and 16 act as source nodes and the spreading process carries on towards the second neighbours of s. In the same way, the third and fourth neighbours are affected by the toxic propagation until the concentration in the nodes falls below c_{th}.

According to this network interpretation, the spreading of a toxic gas in the urban environment is governed by two properties of the network: (i) the topological connectivity of the network, given by its adjacency matrix $\mathbf{A}$, and (ii) the

concentration decay along the links, given by a combination of the geometrical characteristics and the flow dynamics in the street canyons.

This spreading results in the zone of influence ($\mathcal{Z}_s$) of the source node s, i.e. the set of links contaminated from the propagation process originated in s (the elements highlighted in blue in Fig. 2.1). The number of people living in the zone of influence represents the vulnerability index of s ($\mathcal{V}_s$). Notice that this index contains both information on population density and meteorological conditions in the city. In fact, as will be shown in the following sections, its value changes drastically with the wind direction.

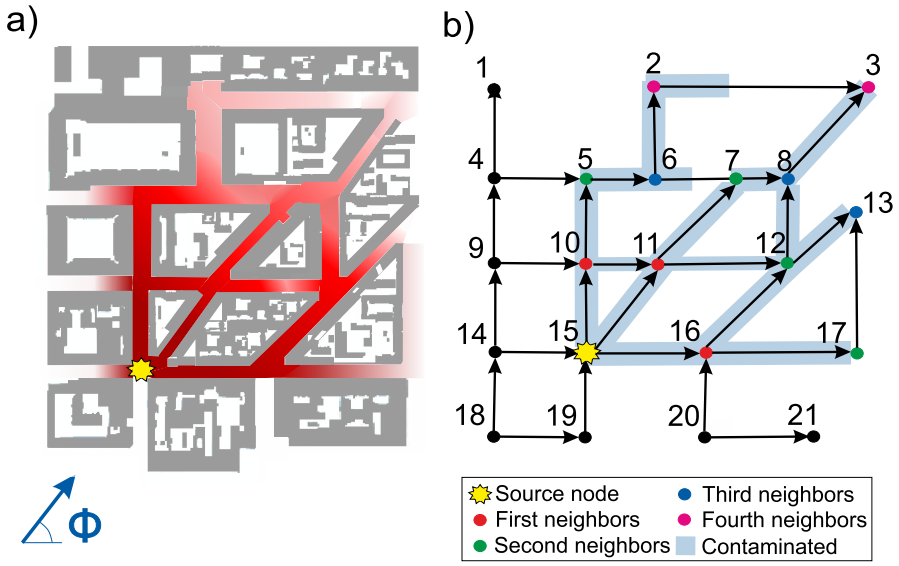

Figure 2.1: Analogy between the physical propagation of a toxic substance in the urban environment (a) and the spreading process on a network (b). Φ is the direction of the external wind blowing on the city.

2.2 A depth-first search algorithm to delimit the zone of influence of a source node

Given a source node s with a concentration c_s, the set of its first neighbours $\mathcal{N}_1(s)$ can be derived from the non-zero elements of the $s-th$ row of the adjacency matrix $\mathbf{A}$. In Fig. 2.1, $s = 15$ and thus $\mathcal{N}_1(s) = \{10,11,16\}$. For each node f belonging to the set $\mathcal{N}_1(s)$, the algorithm calculates the distance Z_{sf}^{pot}. This length is the potential distance (hence the superscript pot) that the contaminated front can reach along the link (s, f) with a concentration higher than the predefined threshold c_{th}. According to Eq. 1.26, Z_{sf}^{pot} is

$$Z_{sf}^{pot} = -\frac{H_{sf}}{U_{d,sf}} U_{sf} \log\left(\frac{c_{th}}{c_s}\right), \quad \forall f \in \mathcal{N}_1(s). \tag{2.2}$$

In general, Z_{sf}^{pot} is different from the physical length of the street (L_{sf}) associated to the link (s, f). Z_{sf}^{pot} is lower than L_{sf} if the concentration undergoes the threshold c_{th} before the propagation front has travelled the entire street. Conversely, it is higher if the front reaches node f with a concentration above the threshold. As a consequence, the effective contaminated distance (Z_{sf}) is the minimum between the reachable distance Z_{sf}^{pot} and the effective length of the street, i.e.

$$Z_{sf} = \min[Z_{sf}^{pot}, L_{sf}]. \tag{2.3}$$

If $Z_{sf} = L_{sf}$, the substance has reached the target node f with a concentration equal to or higher than c_{th}. As a result, node f is contaminated. Conversely, if the front reaches f with a negligible concentration (i.e. $Z_{sf} < L_{sf}$), then node f remains uncontaminated. In both cases, the algorithm stores the effective contaminated length Z_{sf} as the (s, f) element in the matrix $\mathbf{Z}$. As introduced in Section 1.3, this matrix defines the extent of the zone of influence of the source node s.

We define $\widehat{\mathcal{N}}_1(s)$ the set of the first neighbours of s that have been effectively contaminated,

$$\widehat{\mathcal{N}}_1(s) = \{f \in \mathcal{N}_1(s) \mid Z_{sf} = L_{sf}\}. \tag{2.4}$$

Referring to Fig. 2.1, $\widehat{\mathcal{N}}_1(15)$ = {10,11,16} since all the first neighbours of s are contaminated. The algorithm estimates the concentration in the nodes belonging to $\widehat{\mathcal{N}}_1(s)$ using Eq. 1.26, as

$$c_f = c_s e^{-\frac{U_{d,sf}}{H_{sf}} \frac{L_{sf}}{U_{sf}}}, \quad \forall f \in \widehat{\mathcal{N}}_1(s). \tag{2.5}$$

These nodes behave as new source nodes. Thus, the algorithm repeats the above presented steps, replacing in Eqs. 2.2-2.5 node s with the nodes belonging to $\widehat{\mathcal{N}}_1(s)$. For example, once node 16 (Fig. 2.1) has been contaminated from the initial source node 15, the algorithm finds the set of its first neighbours, i.e. $\mathcal{N}_1(16) = \{12, 17\}$. Eqs. 2.2-2.3 estimate the effective contaminated length along links (16, 12) and (16, 17), while Eq. 2.4 identifies the set of the first neighbours of node 16 that have been infected, i.e. $\widehat{\mathcal{N}}_1(16) = \{12, 17\}$. Finally, the concentration reached in nodes 12 and 17 is determined by Eq. 2.5. This procedure is repeated recursively until the concentration in each node of the network falls below the threshold c_{th}.

Notice that for nodes 15 and 16 the sets $\mathcal{N}_1$ and $\widehat{\mathcal{N}}_1$ are identical. However, this is not true in general. Consider node 6 in Fig. 2.1.b. The set of its first neighbours is $\mathcal{N}_1(6) = \{2, 7\}$, while $\widehat{\mathcal{N}}_1(6) = \{2\}$ because node 7 cannot be reached by the

propagation along link (6, 7).

The algorithm explores the nodes of the network starting from a root node and progressively visiting the adjacent nodes. In computer science, this process is called tree traversal [Valiente, 2013] since the result of the exploration is a tree structure that is a subgraph of the initial graph. In our study, this tree corresponds to the zone of influence of the source node. There are multiple ways to perform a tree traversal, according to the order in which the nodes are visited. The algorithm we use explores the nodes of the network using a depth-first search analysis. The algorithm starts at the source node and goes as far as it can down a given branch before backtracking. Referring to Fig. 2.1, the algorithm starts at node 15, selects the first node 10 in the set $\widehat{\mathcal{N}}_1(15)$ and deepens the analysis in the first element of the set $\widehat{\mathcal{N}}_1(10)$, i.e. node 5. Following this method, the algorithm visits the nodes in the order (15, 10, 5, 6, 2). The in-depth analysis along this path ends when the concentration falls below the threshold c_{th}. Formally, the path (15, 10, 5, 6, 2) ends because the set $\widehat{\mathcal{N}}_1(2)$ is empty. Once the first branch has been explored, the algorithm backtracks to node 6's next available neighbour, i.e. node 7.

From the numerical point of view, depth-first search analysis requires less memory and it is more efficient in finding trees on networks compared to other algorithms, such as breath-first search [Kozen, 1992].

Notice that, referring to the example in Fig. 2.1.b, link $(11, 7)$ is affected by toxic propagation twice, both along propagation path $\mathcal{P}_1$=(15, 11, 7) and $\mathcal{P}_2$=(15, 10, 11, 7). As a consequence the algorithm calculates two different values of $Z_{11,7}$, since the concentration reached at node 11 (c_{11}) along $\mathcal{P}_1$ is generally different from the one obtained along $\mathcal{P}_2$. As the aim of the method is to determine the extent of the zone of influence, the algorithm considers all the possible passages through a generic link and stores the longest distance reached by the toxic substance. More precisely, for each path $\mathcal{P}_\alpha$ the algorithm compares $Z_{sf}^{(\mathcal{P}_\alpha)}$ with the distance $Z_{sf}^{(\mathcal{P}_{\alpha-1})}$ obtained along the previously explored path $\mathcal{P}_{\alpha-1}$ passing through the link (s, f). Equation 2.3 is, thus, refined as:

$$Z_{sf}^{(\mathcal{P}_\alpha)} = \max[\min[Z_{sf}^{pot}, L_{sf}], D_{sf}^{(\mathcal{P}_{\alpha-1})}], \tag{2.6}$$

where $\mathcal{P}_\alpha$ is an index for the order in which the path is explored. This corresponds to considering in node 7, the maximum concentration of the incoming flows, in accordance with the assumptions in Subsection 1.2.2.

2.3 Application of the algorithm to a case study

The potential of the proposed approach is discussed through a case study. The model is applied to assess urban vulnerability of the city of Lyon (France) to the release of a toxic gas. Lyon (Fig. 2.2) is located in east-central France and it is the

third-largest urban agglomeration in France after Paris and Marseille, with a population of approximately 1.5 million inhabitants. In this work, the analysis is limited to a part of the city (Fig. 2.2.c) that presents an intricate urban fabric and tall buildings on the edges of the streets. These characteristics are consistent with the model representation of the streets as a network of street canyons. The study area has an extent of about 6.5 km^2, it hosts a population of about 140,000 inhabitants and is delimited by natural and artificial boundaries (rivers, parks and railways). These boundaries determine a discontinuity in the dispersion of pollutants along the street canyons.

The street canyons and the street intersections result in a network of 750 nodes and 1110 links. The geometrical characteristics of the street canyons, the population density, the longitudinal mean wind and the vertical transfer velocity in the streets are stored in the matrices $\mathbf{H}$, $\mathbf{L}$, $\mathbf{P}$, $\mathbf{U_{st}}$ and $\mathbf{U_d}$, respectively.

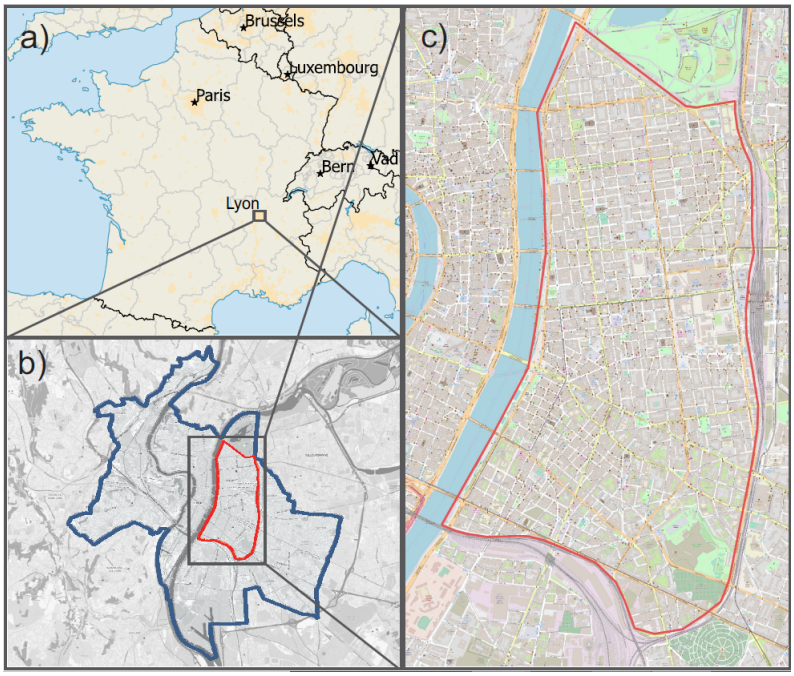

Figure 2.2: The case study area. a) Location of the metropolitan area of Lyon within France. b) Location of the study area within the municipality of Lyon. c) The study area.

2.3.1 The zone of influence of a source node

The first outcome of the model is the identification of the zone of influence of a source node $\mathcal{Z}$, i.e. the set of links contaminated by the toxic substance with a concentration above a defined threshold (see Section 1.3).

As an example, Fig. 2.3 shows the zone of influence of a source node for different wind directions ($\Phi = 45°$, $135°$, $225°$ and $315°$) and for two different initial concentration values. For the sake of generality, the concentration scenarios are defined by the ratio between the concentration in the source node (c_0) and the limit concentration (c_{th}).

The urban topology, the wind direction and the initial concentration shape the zone of influence of the source node. Variations in the mean velocity of the external wind as well as the stability conditions (as determined by the Monin-Obukhov length) are instead irrelevant. As stated in Eq. 1.12 and Eqs. 1.10-1.11, both u_d and u_{st} depend linearly on the friction velocity u_*. Since our propagation model evaluates the pollutant spreading as a function of their ratio (Eq. 1.26), variations of u_*, and thus of the Monin-Obukhov length and the mean velocity of the external wind, will not be effective in determining the zone of influence.

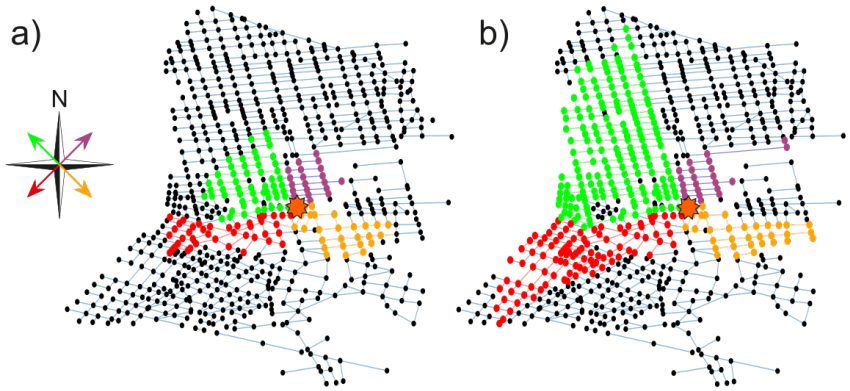

Figure 2.3: The zone of influence of a generic source node (orange star) in the network for different wind directions (red, green, violet and yellow refer to the wind directions $\Phi = 45°$, $135°$, $225°$ and $315°$, respectively). Panel (a) and (b) refer to a concentration ratio $c_0/c_{th} = 10$ and $c_0/c_{th} = 100$, respectively.

2.3.2 Spatial and frequency distribution of urban vulnerability

The spatial pattern of urban vulnerability can be analysed at a glance using vulnerability maps. Given the geometry of the urban fabric, the conditions of the external wind, the spatial distribution of the citizens and the emission scenario, the model provides a map that associates at each node of the street network its vulnerability index. The computational time is 2 (in the case of $c_0/c_{th} = 100$) or 3 (in the case of $c_0/c_{th} = 10$) orders of magnitude lower than the time taken by well-known street network models as SIRANE. As mentioned in Section 1.3, this is achieved by first applying the algorithm for the spread of toxic substances on

networks (Section 1.3) and by computing the matrix of the contaminated street lengths **Z** for all nodes of the network. Next, the vulnerability index defined in Eq. 2.1 is calculated for each node, taking into account both the extent of the zone affected by the propagation originated in the node (**Z**) and the number of people leaving in that zone (**P**). Finally, a vulnerability map is constructed by associating a colour to each node based on its vulnerability index.

Sixteen vulnerability maps for the case study area are obtained by varying the direction of the external wind (Φ) and the concentration ratio c_0/c_{th}. These parameters affect the node vulnerability by shaping the extent of its zone of influence, as mentioned in Section 2.3.1. In this study, the number of inhabitants in the streets (**P**) was kept constant in the different scenarios and was derived from the map of the resident citizens in the city of Lyon. Future works should consider how the spatial distribution of the population varies on different days of the week or at different times of the day. These variations could be easily implemented in the model by modifying the **P** matrix and would increase the number of cases (i.e. maps) considered.

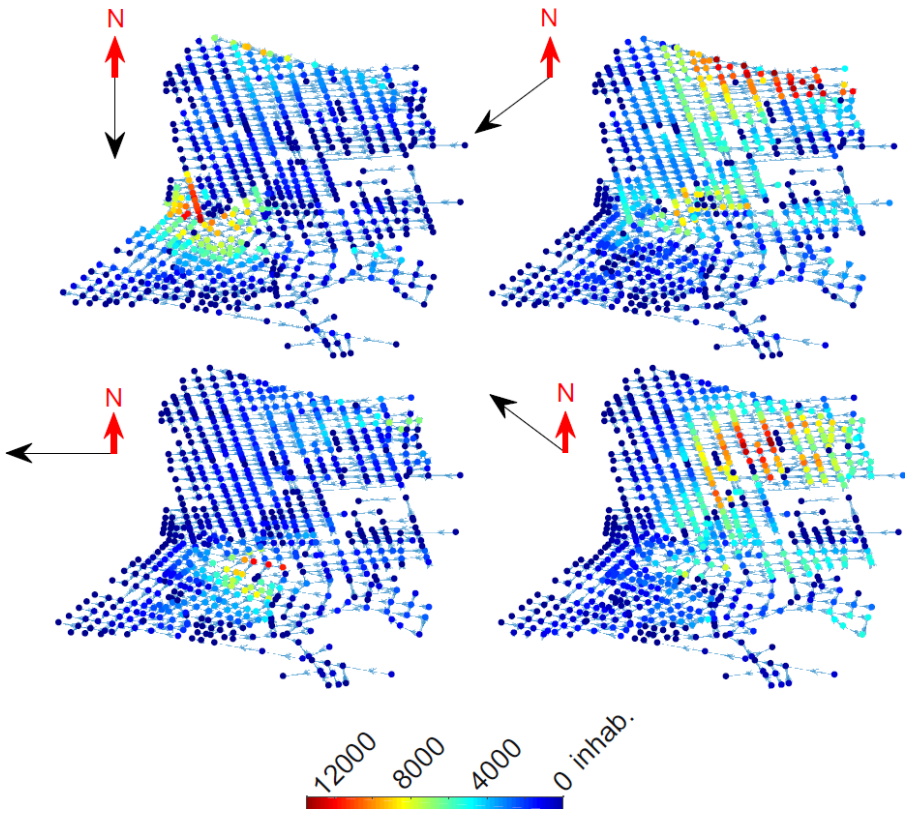

Figure 2.4: Vulnerability ($\mathcal{V}$) maps for different wind directions and with a concentration ratio c_0/c_{th} equal to 10. Wind direction with respect to the North is reported as a black arrow.

Fig. 2.4 shows four vulnerability maps for a wind direction varying between $\Phi = 0°$ (north wind) and $\Phi = 135°$. The maps are obtained simulating for each node a release with a concentration equal to ten times the threshold value, i.e. $c_0/c_{th} = 10$. Node vulnerability, defined in terms of number of affected people, varies between 0 (blue) and 12000 (red) inhabitants. The maps reveal at a glance the most susceptible zones and the global vulnerability of the urban area in the different wind direction scenarios. From Fig. 2.4, it can be seen that the vulnerability index is not distributed homogeneously. On the contrary, the vulnerability tends to be maximal (red nodes) in a defined area of the map and its value gradually decreases in the nodes around it. Moreover, the position of the most vulnerable nodes varies strongly with small variations in the wind direction. As an example, notice the difference between the two scenarios related to $\Phi = 0°$ and $\Phi = 45°$ in Fig. 2.4.

To better understand this behaviour, Fig. 2.5.a summaries the results of the sixteen simulated scenarios. Each scenario is represented by an arrow oriented with the wind direction, coloured according to the concentration ratio and positioned in the area of greatest vulnerability for that scenario. It is evident that for Φ equal to 0°, 90°, 180° and 270° (the cardinal directions) the most vulnerable nodes are located in the southern part of the network, while for Φ equal to 45°, 135°, 225° and 315° (the transversal directions) the most vulnerable areas are in the northern part of the network.

As the geometrical characteristics of the street canyons and the population density are rather homogeneously distributed in the street network, this different vulnerability pattern seems to be related to the orientation of the streets with respect to the wind direction. In fact, the northern part of the street network is mainly oriented according to the cardinal directions (North-South and West-East oriented streets) and experiences the highest vulnerability when the wind blows according to one of the transversal directions. Conversely, the southern part of the street network is oriented mainly according to the oblique directions, and a greater vulnerability occurs when the wind is blowing in the cardinal directions. Thus, if the wind blows obliquely with respect to street orientations then vulnerability increases.

For each of the sixteen scenarios analysed, the average vulnerability over the entire network ($\overline{\mathcal{V}}$) is calculated as

$$\overline{\mathcal{V}} = \frac{1}{N} \sum_{i}^{N} \mathcal{V}_i, \tag{2.7}$$

where $\mathcal{V}_i$ is the vulnerability index for the $i-th$ node and N is the number of nodes in the network. The two polar histograms of Fig. 2.5.b report these average vulnerability values for the two concentration ratios considered. Each sector in the polar histograms refers to a different wind direction. As expected, higher concentration ratios correspond to higher vulnerability values. Moreover, since most of the streets

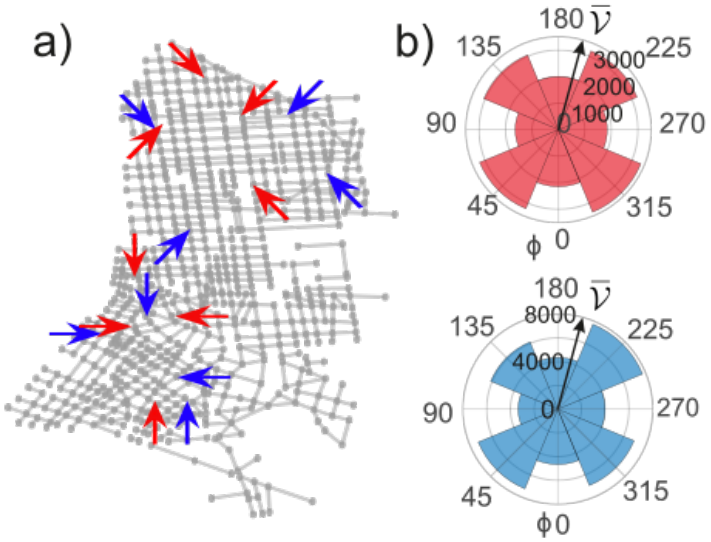

Figure 2.5: a) Most vulnerable areas in the street network for different wind directions and concentration ratios. Each scenario is represented by an arrow oriented according to the wind direction, coloured according to the concentration ratio (red arrows for $c_0/c_{th} = 10$ and blue arrows for $c_0/c_{th} = 100$) and positioned in the area of greatest vulnerability on the map. b) Polar histogram (red for $c_0/c_{th} = 10$ and blue for $c_0/c_{th} = 100$) of the average node vulnerability for the different wind directions

($\sim 60\%$) are oriented in the cardinal directions, the average vulnerability is greater when the wind blows in the oblique directions.

Fig. 2.6 gives an overview of the long-term vulnerability of the urban fabric to toxic releases. The maps depict nodes vulnerability weighted by the annual frequency of the wind directions over the city of Lyon. As detailed in the inset of Fig. 2.6, the dominant wind direction in Lyon is North-South. As a consequence, the highest vulnerabilities are located in the circled area, corresponding to the most critical area when North-South oriented winds blow (see Fig. 2.5.a).

Results in Fig. 2.4 suggest that, for each scenario, a restricted area of the urban fabric is characterized by high levels of vulnerability, while most of the nodes have a low spreading potential. Thus, both spatial and frequency distribution of node vulnerabilities are not trivial. A frequency analysis of vulnerability values was performed to identify the statistical distribution of the data. For each scenario, node vulnerability values were classified in ten equal size intervals. Then, the relative frequency (p) of each class was calculated. Fig. 2.7 presents the relative

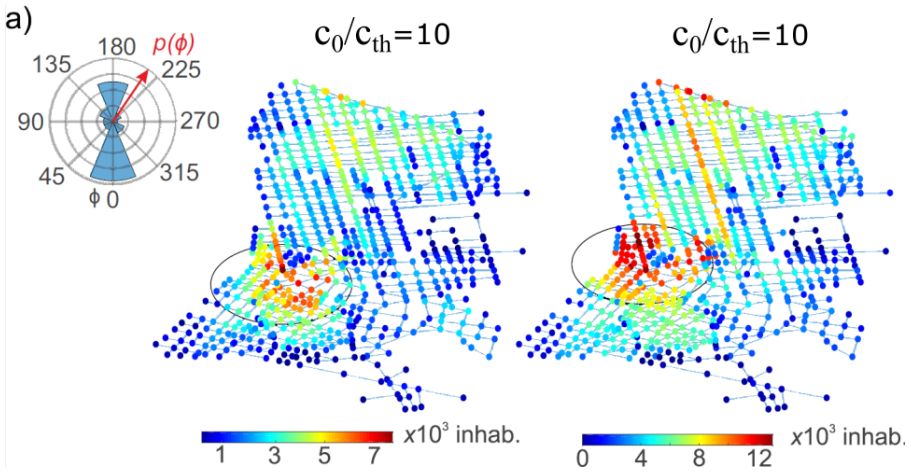

Figure 2.6: Maps of vulnerability weighted by the annual frequency of the wind directions. The polar histogram (inset *a*) shows the occurrence of wind directions in the city of Lyon in terms of annual relative frequency $p(\Phi)$.

frequency of node vulnerability for the different scenarios in a log-log plot. For the sake of graphic clarity, vulnerability values were normalised to the maximum one ($\mathcal{V}_{max}$). Generally, the data show a linear behaviour in the log-log plot, thus exhibiting a power law trend. The power law confirms that vulnerability distribution is heterogeneous, with few nodes being much more critical than the others. This configuration suggests that, for each wind scenario, the entire neighbourhood could be protected with security interventions targeted on small urban areas. From the opposite point of view, it demonstrates that a malicious release of gaseous substances can have a much more dramatic effect if it occurs in points characterized by maximum vulnerability.

Many real-world networks (e.g., the Internet, World Wide Web, scientific citations) present a power law distribution of node degree [Boccaletti et al., 2006]. The degree defines the importance of a node in the network in terms of its connectivity. In this case, a power law results from the non-trivial interaction of multiple factors that define the vulnerability index, i.e. the topological connectivity of the network, the geometry characteristics of the street canyons, the toxic spreading process and the population distribution in the city.

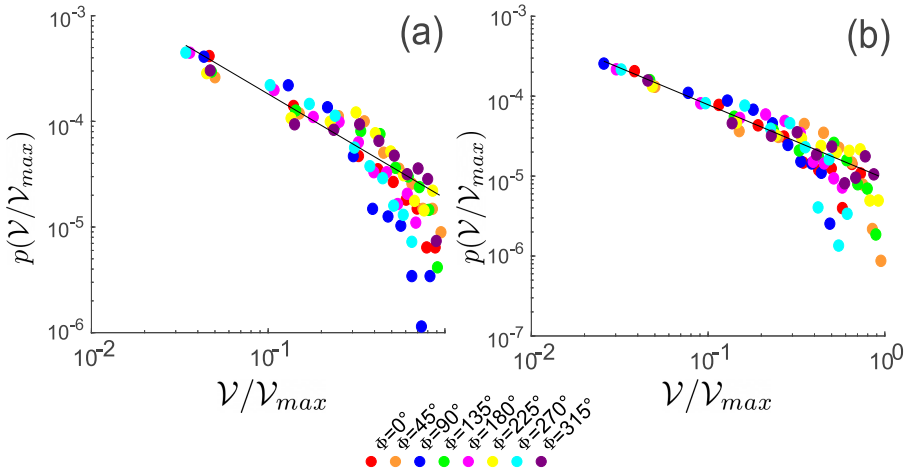

Figure 2.7: Relative frequency of vulnerability for different wind directions and for a concentration ratio $c_0/c_{th} = 10$ (a) and $c_0/c_{th} = 100$ (b). The display is in logarithmic scale.

2.4 Comparison with the model SIRANE

In the previous sections, a complex network approach has been adopted to delimit the zone of influence of a source point in the urban canopy. The zone of influence is defined as the set of streets in which pollutant concentration is above a certain threshold c_{th}. To validate this approach, we compare this zone of influence with the one obtained by means of the well-known model SIRANE.

SIRANE is an atmospheric dispersion model for urban air quality validated against both wind tunnel experiments and field campaigns [Soulhac et al., 2003, Carpentieri et al., 2012b, Soulhac et al., 2012, Soulhac et al., 2017]. The software requires many input parameters, as those related to the meteorological conditions and to the physico-chemical properties of the pollutants. Pollutants are released in the streets, differently from the network model presented above which accounts for pollutant sources located in the street intersections. Starting from a single pollutant source, the typical output of SIRANE is the mean concentration in each street of the network. From these results, we can delimit the zone of influence of the source link as the set of streets in which the mean concentration is above a threshold ($c_{th} = c_0/10$).

For the sake of comparison, we attempt to find the same result, i.e. the zone of influence of a source link, using the tree traversal algorithm proposed in Section 2.2. To this aim, an initial concentration c_0 is imposed at both the extreme nodes of a link representing the street canyon in which the release takes place. By means of the spreading algorithm, the propagation in the neighboring links is simulated. The propagation process ends when the concentration in the streets falls below the threshold c_{th} (with $c_{th} = c_0/10$).

For an initially contaminated street, we can thus formally define the zones of influence delimited by the network model ($\mathcal{Z}_\mathcal{M}$) and by SIRANE ($\mathcal{Z}_\mathcal{S}$) as the following sets:

$$\mathcal{Z}_\mathcal{M} = \{e \,|\, c_M(e) \geq c_{M,th}\}, \qquad \mathcal{Z}_\mathcal{S} = \{e \,|\, c_S(e) \geq c_{S,th}\}, \tag{2.8}$$

where e are the links of the network, $c_M(e)$ and $c_S(e)$ are the mean concentrations along each street calculated by the network model and by SIRANE, while $c_{M,th}$ and $c_{S,th}$ are the predefined threshold concentrations.

The possible errors in delimiting the zone of influence are as follows:

- the network model includes in the zone of influence ($\mathcal{Z}_\mathcal{M}$) streets that do not belong to the zone of influence defined by SIRANE ($\mathcal{Z}_\mathcal{S}$). We define ε the set of streets included incorrectly ("extra streets"):

$$\varepsilon = \mathcal{Z}_\mathcal{M} \setminus \mathcal{Z}_\mathcal{S} = \{e \in \mathcal{Z}_\mathcal{M} \,|\, e \notin \mathcal{Z}_\mathcal{S}\}; \tag{2.9}$$

- the network model does not include in the zone of influence ($\mathcal{Z}_\mathcal{M}$) streets that belong to the zone of influence defined by SIRANE ($\mathcal{Z}_\mathcal{S}$). We define $\mathcal{N}$ this set of neglected streets ("neglected streets").

$$\mathcal{N} = \mathcal{Z}_\mathcal{S} \setminus \mathcal{Z}_\mathcal{M} = \{e \in \mathcal{Z}_\mathcal{S} \,|\, e \notin \mathcal{Z}_\mathcal{M}\}. \tag{2.10}$$

The relation between the different sets can be visualized in Figure 2.8.

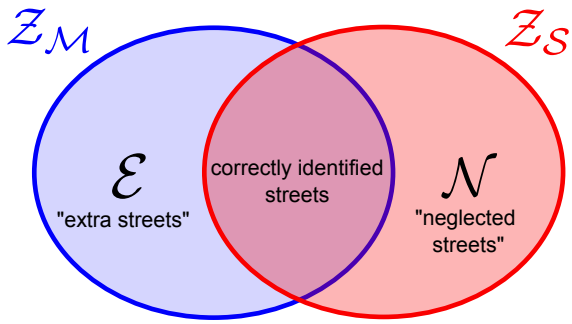

Figure 2.8: Relation between the different sets: $\mathcal{Z}_\mathcal{M}$=zone of influence delimited by the network model, $\mathcal{Z}_\mathcal{S}$=zone of influence delimited by SIRANE, ε=extra streets, $\mathcal{N}$=neglected streets.

The error associated to ε is minimum when the network model does not include any extra street ($\varepsilon = \{\}$). It is maximum when all the streets in $\mathcal{Z}_\mathcal{M}$ are not in the zone of influence delimited by SIRANE ($\mathcal{Z}_\mathcal{S}$). We can build an error index associated to ε and varying between [0,1]:

$$I_\varepsilon = \frac{\sum_{i\in\varepsilon} l_i \frac{c_{S,i}}{c_{S,0}}}{\sum_{i\in\mathcal{Z}_\mathcal{M}} l_i \frac{c_{S,i}}{c_{S,0}}}. \tag{2.11}$$

I_ε is equal to 0 when there are no "extra streets". It is equal to 1 when all the streets in the zone of influence ($\mathcal{Z}_\mathcal{M}$) are also in ε, i.e. when all the streets are wrongly detected. The length of each street is weighted on pollutant concentration. In this way, the severity of the error depends on the level of pollution inside the streets.

Similarly, we introduce an error index associated to the "neglected streets" and varying between [0,1]:

$$I_\mathcal{N} = \frac{\sum_{i\in\mathcal{N}} l_i \frac{c_{S,i}}{c_{S,0}}}{\sum_{i\in\mathcal{Z}_\mathcal{S}} l_i \frac{c_{S,i}}{c_{S,0}}} \tag{2.12}$$

$I_\mathcal{N}$ is equal to 0 when there are no "neglected streets", i.e. when $\mathcal{N} = \{\}$. It is equal to 1 when all the streets in the zone of influence of SIRANE ($\mathcal{Z}_\mathcal{S}$) are also in $\mathcal{N}$, i.e. when all the contaminated street are not detected by the network model.

The two indexes can be combined to give a unique error index:

$$I = \frac{\sum_{i\in\varepsilon} l_i \frac{c_{S,i}}{c_{S,0}} + \sum_{i\in\mathcal{N}} l_i \frac{c_{S,i}}{c_{S,0}}}{\sum_{i\in\mathcal{Z}_\mathcal{M}} l_i \frac{c_{S,i}}{c_{S,0}} + \sum_{i\in\mathcal{Z}_\mathcal{S}} l_i \frac{c_{S,i}}{c_{S,0}}}. \tag{2.13}$$

In Figs. 2.9 and 2.10 the probability density function of the three error indexes in shown for the urban areas of Lyon (France) and Firenze (Italy), for eight different wind directions. The error associated to the neglected streets ($I_{\mathcal{N}}$) has a longer tail, while the error associated to the extra streets is generally below 0.45. The total error I is mostly lower than 0.1. While the distributions tend to overlap for the city of Firenze, in the case of Lyon two different trends are observable for wind directions oblique (0°, 90°, 180° and 270°) or aligned (0°, 90°, 180° and 270°) with respect to the main axis of the street network.

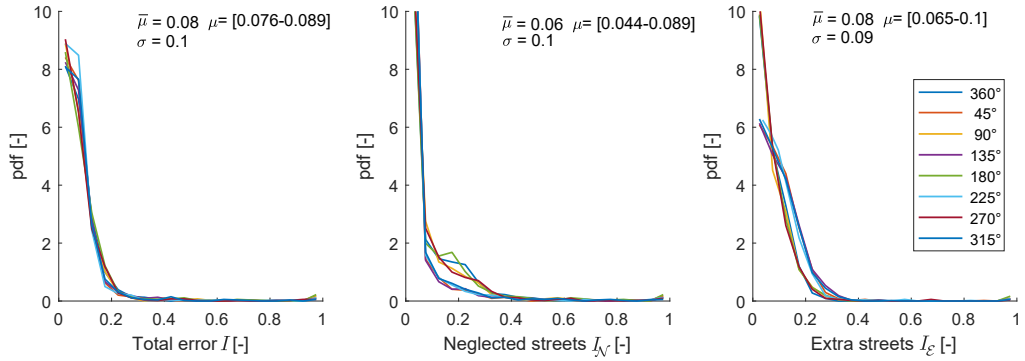

Figure 2.9: Probability density function of the error associated to the extra streets (I_{ε}), to the neglected streets ($I_{\mathcal{N}}$), and the total error (I) for different wind directions for the city of Lyon. The mean $\overline{\mu}$ and standard deviation σ calculated over the entire set of scenarios are reported numerically. The range of variation for the mean μ for the different wind directions is also shown.

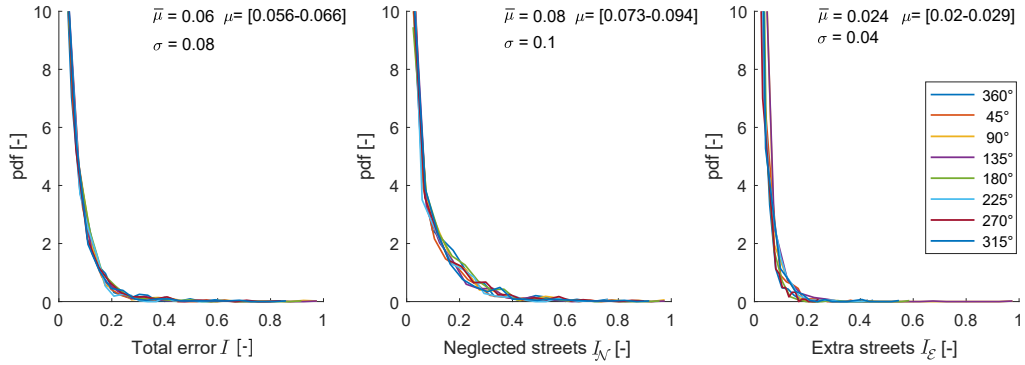

Figure 2.10: Probability density function of the error associated to the extra streets (I_{ε}), to the neglected streets ($I_{\mathcal{N}}$), and the total error (I) for different wind directions for the city of Firenze. The mean $\overline{\mu}$ and standard deviation σ calculated over the entire set of scenarios are reported numerically. The range of variation for the mean μ for the different wind directions is also shown.

The spatial distribution of the error index I is reported in Fig. 2.11 for the city

centre of Firenze and for a wind blowing from North to South. Streets whose zone of influence give an error index (I) greater than 0.3 are coloured in red. They are not concentrated in a particular part of the network but generally coincide with interruptions of the network connections (see for example the comparison between the zone of influence of SIRANE and the one identified by the network model in Fig. 2.12).

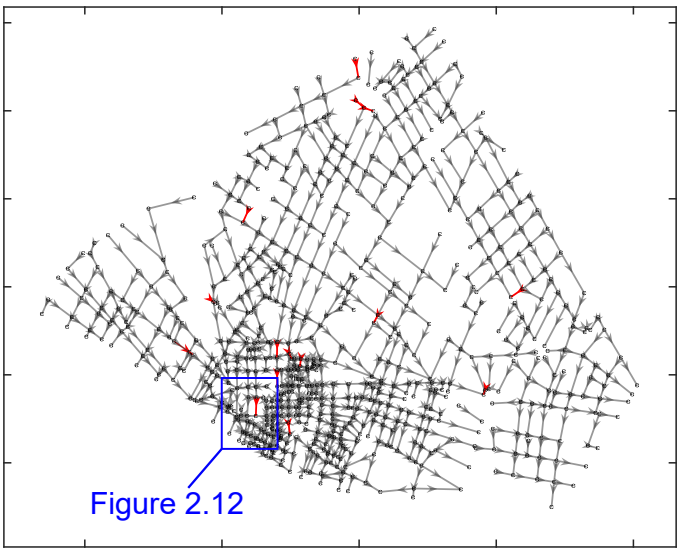

Figure 2.11: Street network of the city centre of Firenze. The links whose zone of influence is characterized by a total error index I greater than 0.3 are highlighted in red.

In short, the network model can capture the contaminated area with a satisfying degree of precision. However, the model tends to underestimate the extent of the contamination when the street network is interrupted. Conversely, in SIRANE the pollutant plume can bypass the buildings as the dynamics of dispersion above the buildings are simulated and, therefore, re-entrainment from the external flow towards the streets is taken into account.

We conclude by mentioning that the network model and SIRANE actually simulate different aspects of the propagation event. SIRANE aims to accurately estimate the average concentration in the streets. Conversely, the target of the network model is the delimitation of the zone of influence of a pollutant source. In particular, this zone is the worst case scenario of the propagation process. The assumptions underlying the model are in fact conservative (see for example the hypothesis for transport in street intersections in Section 1.2.2) to take into account all the potential propagation paths. For this reason, an experimental validation of the network model is desirable, allowing to investigate not only the average concentrations in each street, modeled by SIRANE, but also the rare events, captured by the higher moments of the probability density function of concentration [Cassiani et al., 2020].

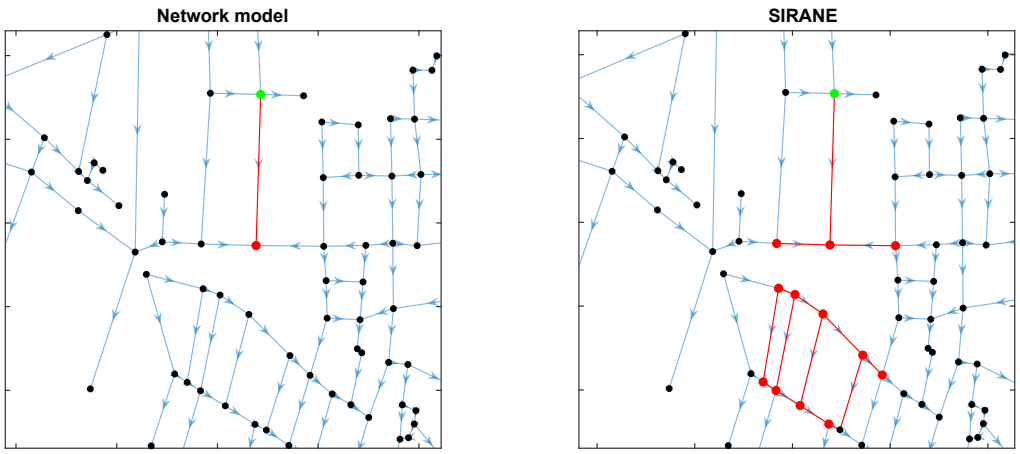

Figure 2.12: An example of the difference between the zone of influence estimated by the network model (left) and by SIRANE (right) due to interruption of the network connections. The green node is the first node of the source link, the red links are those belonging to the zone of influence in the two cases.

Chapter 3

A tailored centrality metric for confined spreading potential

The work described in this chapter has been derived from [Fellini et al., 2020b].

In previous chapters, we proposed a network perspective for the identification of the most critical areas for gaseous release in a city. In this chapter, we delve deeper into the subject and provide a formalism that comes closer to that of complex network theory and more suitable for its research community.

First, we define a fluid dynamic weight for network links, which translates the physics of the dispersion problem in the framework of the weighted complex networks. Then, we provide a tailored centrality metric for the detection of the best spreader nodes in the network. While the identification of best spreader nodes is a well-known classical problem in social, information and technology networks [Pastor-Satorras and Vespignani, 2001, Kitsak et al., 2010, Basaras et al., 2013], the uncritical application of traditional metrics to mass transport in a flow network reveals some drawbacks. Specifically, the mass conservation of the dispersed substance, the spatial constraints of the physical network, and the non-probabilistic nature of the contagion (meant as probability of infection between two linked nodes, e.g., [May and Lloyd, 2001]), make this problem original and evidence the need for a tailored centrality metric. Finally, the potential of the proposed approach is assessed by the construction of vulnerability maps of urban districts and by comparison of its performance with that of a more detailed propagation model.

3.1 Fluid dynamic weight for propagation cost

In the proposed network-based approach, the whole spatially-embedded transport domain for pollutant propagation is modelled as a directed and weighted network $\mathcal{G}(\mathcal{S},\mathcal{E},\mathbf{w})$, with node-set $\mathcal{S}$, edge-set $\mathcal{E}$ and weight matrix $\mathbf{w}$. Network

structure (Fig. 3.1) is given by abstracting street canyons as links and street intersections as nodes [Crucitti et al., 2006]. Link direction is given by the orientation of the longitudinal wind along the street, while link weight reflects the transport capacity of the street canyon.

Within this representation, the definition of the weight is crucial as it is the only expression for the physical propagation law. As common in space [Barthélemy, 2011] and flow [Ahujia et al., 1993] networks, links are seen here as distances between nodes, i.e. as leak terms for the transport process. Thus, referring to Eq. 1.26, we define the weight w_{ij} as the cost associated with traversing the link $(i,j) \in \mathcal{E}$, i.e. as the concentration decay along the corresponding street canyon:

$$w_{ij} = e^{\frac{L_{ij}U_{d,ij}}{U_{st,ij}H_{ij}}}, \tag{3.1}$$

where we recall that $\mathbf{L}$, $\mathbf{H}$, $\mathbf{U_{st}}$, and $\mathbf{U_d}$ are the matrices that stores, for each (i,j) link of the network, the length (L) and height (H) of the street canyon, and the longitudinal (u_{st}) and vertical (u_d) transport velocities. In a spreading perspective, the exponent in Eq. 3.1 can be interpreted as the effective distance between nodes [Brockmann and Helbing, 2013]. This distance increases with the average time necessary for the pollution front to propagate longitudinally along the street canyon ($L_{ij}/U_{st,ij}$), while decreases with the average time of vertical transfer of pollutants from the street to the external atmosphere ($H_{ij}/U_{d,ij}$).

3.2 Novel centrality metric

Given this network representation, the most dangerous locations for the release of airborne pollutants in a city are the best spreader nodes in a complex network. Many metrics are available in literature [Kitsak et al., 2010, Basaras et al., 2013, Zeng and Zhang, 2013, Du et al., 2015, Van Mieghem et al., 2017, Erkol et al., 2019] to detect best spreaders in SIR-like epidemics [Diekmann and Heesterbeek, 2000, Nåsell, 2002], e.g., the spreading of infectious diseases in a population, or information dissemination in a social environment. These epidemic processes have a stochastic nature since the spreading from one node to another occurs with a certain probability. Moreover, there is no decay of the spreading potential with distance from the source. On the contrast, the propagation of airborne pollutants is here modelled as a deterministic (i.e. contagion certainly takes place if two links are connected), mass-conservative and spatial transport process. Thus, the metrics proposed so far are not suitable, and a tailored centrality index for fluid-dynamic spreading potential has to be sought.

Given the physics of the process, we focus on distance-based centralities, like closeness and betweenness [Brandes, 2005], since the smaller the distance separating

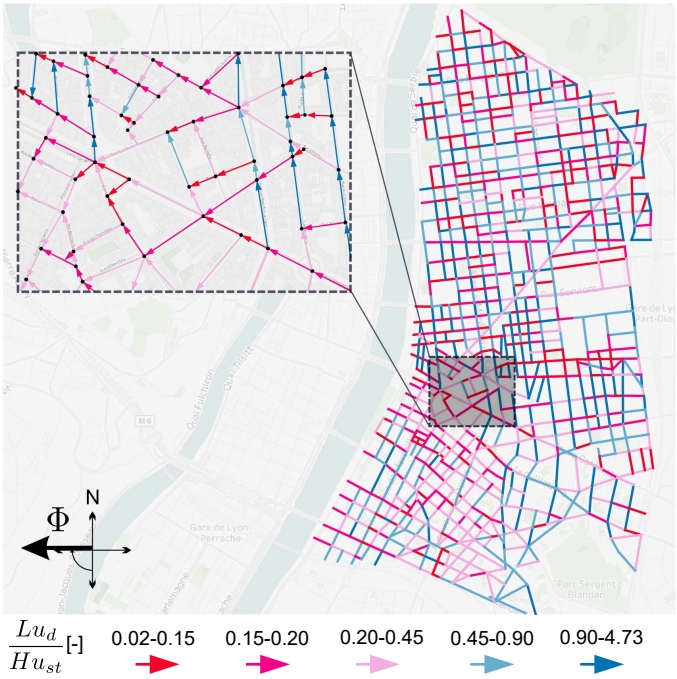

Figure 3.1: Network model of a district in Lyon for $\Phi = 90°$. For each link, the color (grayscale intensity) is a function of the exponent of the weight defined in Eq. 3.1.

the source node from the other nodes in the network, the greater the toxic concentration that will reach them. While betweenness [Freeman, 1977] captures nodes acting as bridges or bottlenecks in network flows [Ser-Giacomi et al., 2019], closeness centrality [Newman, 2010] is better suited for the identification of best spreader nodes. The closeness centrality of a node s is defined as $\mathcal{K}_{clos,s} = 1/\sum_{r\in\mathcal{S}} D_{sr}$, where D_{sr} is the length of the shortest path $\mathcal{D}$ between node s and a generic node r in the network, i.e. the path connecting the two nodes with the minimum number of edges [Newman, 2001]. For a weighted graph, $\mathcal{D}$ is the path that minimizes the sum of the weights of the traversed edges, and thus its length reads:

$$D_{sr} = |\mathcal{D}| = \min_{\mathcal{P}} \left[\sum_{(i,j)\in\mathcal{P}} w_{ij} : \mathcal{P} \text{ is path from } s \text{ to } r \right]. \tag{3.2}$$

In our perspective, given Eqs. 3.1 and 3.2, $\mathcal{D}$ is the critical propagation path between the two nodes as it minimizes the concentration decay. To sum up, the lower the concentration decay along the main propagation paths originated in s, the lower D_{sr}, the higher the closeness centrality of s ($\mathcal{K}_{clos,s}$). From this definition, the metric seems to capture the physics of the process well. But the farthest nodes from s have the longest shortest paths (D_{sr} is even ∞ for the unconnected couples of nodes) and thus the highest influence in the estimation of $\mathcal{K}_{clos,s}$. Conversely, in the physical

process, the farthest spots are hardly reached by the propagation plume, and therefore do not contribute to the danger associated with the source. To overcome this issue, we use the harmonic mean of the shortest paths by introducing the harmonic centrality [Marchiori and Latora, 2000, Rochat, 2009]: $\mathcal{K}_{harm,s} = \sum_{r\in\mathcal{S}} 1/D_{sr}$. In this way, the more node r is far from s, the longer the expected D_{sr}, the less its contribution to $\mathcal{K}_{harm,s}$. With this formulation, harmonic centrality takes into account the progressive concentration decay with distance from the source but still considers all the network nodes as affected by the spreading process. Conversely, the plume concentration along the shortest path becomes negligible at a certain point and the most distant nodes, despite being connected, should not be considered in the centrality estimation of the source. For this reason, we propose the metric $\mathcal{K}_s$ as a tailored harmonic centrality with threshold on shortest path:

$$\mathcal{K}_s = \sum_{r\in\mathcal{R}} \frac{1}{D_{sr}}, \tag{3.3}$$

with $r \in \mathcal{R}$ if

$$\frac{c_r}{c_s} = \prod_{(i,j)\in D} \frac{1}{w_{ij}} > \frac{c_{th}}{c_0}, \tag{3.4}$$

where $c_s = c_0$ is the source concentration, c_r is the concentration at the target node, and c_{th} is the predefined threshold concentration. Condition 3.4 follows from the physical model proposed above (see Eq. 1.26 and the assumptions for propagation in the intersections in Section 1.2.2) and it states that if the concentration along the shortest path between s and r ($\mathcal{D}$) falls below c_{th}, then r is excluded from the sum in Eq. 3.3. By means of the Heaviside function (Θ), Eqs. 3.3 and 3.4 can be rewritten together as:

$$\mathcal{K}_s = \sum_{r\in\mathcal{S}} \Theta\left[\prod_{(i,j)\in D} \frac{1}{w_{ij}} - \frac{c_{th}}{c_0}\right] \frac{1}{D_{sr}}. \tag{3.5}$$

The number of people exposed to the contamination is not considered in this metric to prevent the vulnerability analysis from being overwhelmed by the intrinsic temporal variability and unpredictability of citizens' distribution. However, this information could be easily integrated into the model, by modifying Eq.3.5:

$$\mathcal{K}_s = \sum_{r\in\mathcal{S}} \Theta\left[\prod_{(i,j)\in D} \frac{1}{w_{ij}} - \frac{c_{th}}{c_0}\right] \frac{P_{cum,sr}}{D_{sr}}, \tag{3.6}$$

where $P_{cum,sr}$ is the number of inhabitants along the shortest path $\mathcal{D}$. Since D_{sr} is defined in Eq. 3.2 as the overall propagation cost along the path, we can interpret the metric in Eq. 3.6 as a measure for the number of affected people weighted by the

concentration decay, i.e. the greater the ventilation of pollutants along the path, the higher D_{sr}, the less the impact of the contamination on the exposed inhabitants P_{sr}.

3.3 Centrality maps of urban networks and metric validation

By the proposed perspective, the spreading potential of a spot in a city is given by its centrality as a node in a flow network. Since the best spreading locations are here considered the most dangerous ones, vulnerability maps of urban areas are obtained straightforward as centrality maps. In Fig. 3.2, the vulnerability of the urban district in Lyon (France) is assessed for different wind directions. As for the analyses in Chapter 2, the study area is confined by physical boundaries (i.e. rivers, parks, railways) which act as discontinuity elements in the dispersion process, and therefore justify the network delimitation. The nature of street interconnections and the distribution of link weights (see Fig. 3.1) generate a strong heterogeneity in vulnerability, with marked differences even between neighboring nodes, and with a non-trivial location of the most vulnerable areas, i.e. the clusters of yellow (light gray) nodes. Moreover, the position of the critical nodes completely changes with the orientation of the wind. Fig. 3.3 evidences how different urban topologies exhibit distinctive behaviours to toxic emissions in the same meteorological scenario. The medieval structure of the city centre in Firenze (Italy) (panel b Fig. 3.3) seems to have a sheltering effect to gas dispersion compared to the regular plan in Lyon.

To assess the validity of the proposed metric, we compare the centrality $\mathcal{K}_s$ of a node to the extent of its zone of influence, i.e. the total length of the streets contaminated with a concentration above c_{th}, when the release takes place in the node. Neglecting the role of residential density in Eq. 2.1, we can define the extent of the zone of influence as $ZOI = \sum_i^N \sum_j^N Z_{ij}$. In comparing the two approaches, we wonder whether a centrality metric based solely on shortest paths can capture the dispersion potential of a node given in terms of its total contaminated area. From a computational point of view, the new centrality-based model brings clear advantages. In fact, existing and constantly improving algorithms developed in the field of complex network theory can be exploited to select the shortest paths and compute $\mathcal{K}_s$.

In Fig. 3.4, the node ranking based on $\mathcal{K}_s$ is compared to the one obtained from the extent of the zone of influence. For the urban districts of Lyon, scenarios with two distinct initial concentrations ($c_0/c_{th} = 10$ and 100) are assessed. In each panel, the results for eight different wind directions are reported together. The high correlation in terms of coefficient of determination R^2 (> 0.94) reveals a satisfactorily estimate of the spreading potential of a source node. In Tab. 3.1, the same correlation index is reported for the standard distance centrality metrics

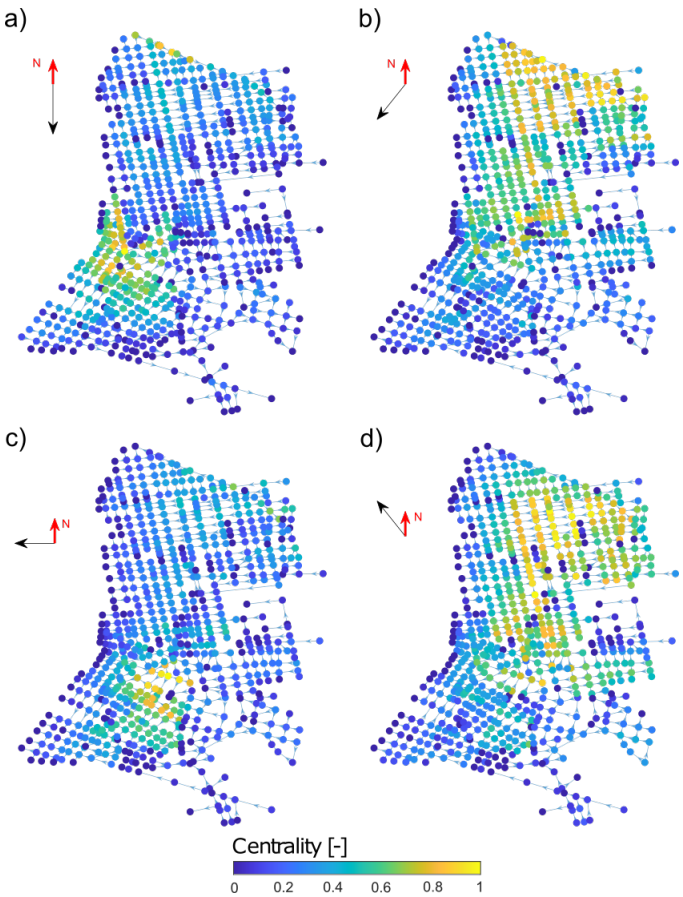

Figure 3.2: Vulnerability maps in terms of spreading potential centrality for an urban district in Lyon for different wind directions: $\Phi = 0°$ (a), 45° (b), 90° (c), and 135° (d). For each scenario, the centrality is normalized by its maximum value in the network.

considered above (for the sake of conciseness we show only results about the $c_0/c_{th} = 10$ scenario). Adopting the fluid-dynamic weight expressed in Eq. 3.1 and analysing the metrics in the same order followed for the definition of the new centrality $\mathcal{K}_s$ (Eq. 3.5), we observe a progressive increase in R^2. Although the performance of harmonic centrality is good in terms of R^2 (R^2=0.82), the proposed centrality metric provides much more reliable results for applications.

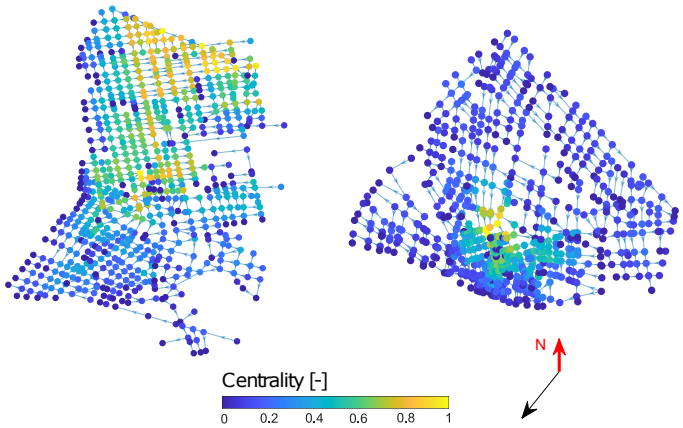

Figure 3.3: Vulnerability maps in terms of spreading potential centrality for an urban district in Lyon (a) and Firenze (b) for $\Phi = 45°$. For each city, the centrality is normalized by its maximum value in the network.

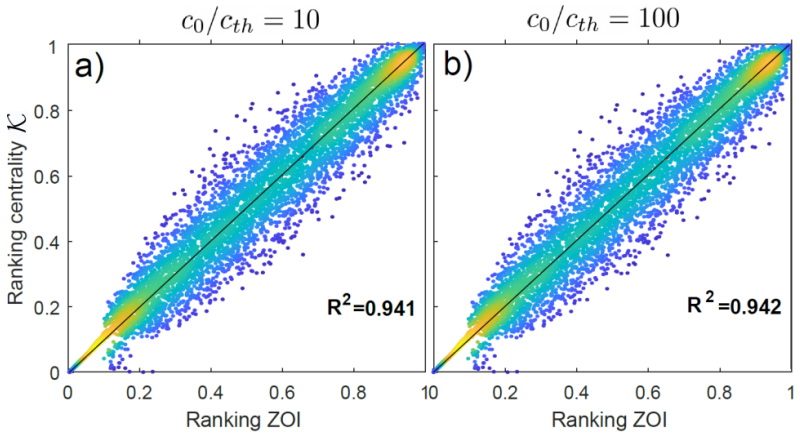

Figure 3.4: Ranking of centrality $\mathcal{K}_s$ vs. ranking of the extent of the zone of influence for $c_0/c_{th} = 10$ (left column) and $c_0/c_{th} = 100$ (left column) for the city of Lyon. The points correspond to the network nodes in multiple wind direction scenarios: $\Phi = 0°$, $45°$, $90°$, $135°$, $180°$, $225°$, $270°$, $315°$. The color of the nodes is related to point density.

Centrality	R^2
betweenness	0.26
closeness	0.54
harmonic	0.82
spreading centrality $\mathcal{K}$ (Eq.3.5)	0.94

Table 3.1: Results in terms of R^2 for the comparison between the ranking of the zone of influence and the ranking of different centrality metrics. As in Fig. 3.4.a, the scenarios with c_0/c_{th}=10 in a district of Lyon are considered.

Chapter 4

Structural fragility of cities to airborne releases

In the previous chapters, we have introduced a novel approach to identify the most vulnerable locations to the release of airborne pollutants in urban areas . In this chapter, we investigate which properties are responsible for this vulnerability, with focus on the geometrical and topological characteristics of the urban fabric.

In recent years, the link between urban morphology and air quality has been investigated with the observation of particular properties of the city as the urban shape [Fan et al., 2019], the packing density of buildings [Buccolieri et al., 2015, Peng et al., 2019] and geometric characteristics [Miao et al., 2020] of the street canyons. However, the way street connectivity and layout can affect urban ventilation is still uncharted territory.

In this chapter, we investigate these aspects and aim to shed light on one of the most challenging questions in the field of urban safety and planning: what makes a city or an urban area vulnerable to airborne releases? How much does topology, in which the history of a city is written, affect ventilation in the streets and thus the vulnerability of the city in case of a toxic release?

To answer these questions we start by adopting the complex network model for pollutant spreading in urban areas: the network structure represents the way the streets are interconnected, the direction of the network links corresponds to the main direction of the wind along each street, the rate of longitudinal transport and vertical loss of pollutants along a street are enclosed in the link weight. In this network representation, we can easily simulate the release of a toxic gas in each node of the network and identify the most vulnerable locations in a city as the best spreading nodes in the network, i.e. the nodes from which largest areas of the network are contaminated. The spreading potential of a node, and thus its vulnerability, can be assessed by means of the tailored centrality metric for pollutant propagation introduced in Chapter 3.

Within this formalism, both the structural and dynamic characteristics of the dispersion phenomenon are enclosed in a single system, that is a directed and weighted complex network with centrality values associated to the nodes. The aim of this work is to disassemble this information-rich object in order to identify the key drivers of pollutant propagation in the streets and to bring out the role of urban topology in the vulnerability of a city to airborne releases.

As a starting point, we analyse the outcomes of this network model and we compare the vulnerability of four districts in Lyon, Paris (France), Firenze (Italy) and New York (US). These urban areas were chosen as emblematic of different topologies, resulting from different historical urban layering. The historic centre of Firenze (panel b in Fig. 4.1) is mainly characterized by a dense urban fabric with a medieval signature of narrow and winding streets [Bini et al., 2016]. In Paris (panel c), Haussman's renovation plan at the end of the 19th century supplemented the North-South and East-West ancient crossroad by a second network of concentric large avenues [Barthelemy et al., 2013]. The rectilinear grid of Manhattan, New York, originates from 1811 [Salat et al., 2014, Baics and Meisterlin, 2019] and extends along the spine of Manhattan island (panel d). Despite the significant difference in size, a similar regular pattern is found in the modern urban area of Lyon (panel a), developed in the second half of the 19th century. In the insets of Fig. 4.1, we report for each city a polar histogram of the orientation of the streets. Although greater variability is observable for the orientation of the streets in the urban areas of Firenze (panel b) and Paris (panel c), two main orthogonal axes are found in the spatial structure of each city.

We promptly compute vulnerability maps for the selected urban areas by means of the centrality metric we introduced in Chapter 3. The nodes with the highest centrality values ($\mathcal{K}$) are the most vulnerable as they correspond to the best spreading locations in the urban fabric. The spreading potential of a node is evaluated based on the extent of the urban area that is contaminated when the release takes place in the node. On the other hand, the number of people exposed to the contamination is not taken into account in order to emphasize the intrinsic vulnerability of the urban structure. In this sense, the concept of vulnerability is here different from the one expressed by the vulnerability index $\mathcal{V}$ in Eq. 2.1, which also accounts for the residential density in the streets.

In Fig. 4.1, we report the vulnerability maps of the four urban areas for the indicative scenario of a wind blowing at an angle $\Phi = 45°$. In the insets of Fig. 4.1, the wind direction is indicated with a red arrow. Given the different orientation and structure of the street networks, Φ is here defined as a clockwise angle with respect to the main axis of the city, which is identified as the longest bar in the polar histogram of street orientation.

To extend the analysis to multiple meteorological scenarios, a compact representation of urban vulnerability in terms of cumulative distribution function (*cdf*) is shown in Fig. 4.2.a. For each city, we estimate the vulnerability of each node (seen

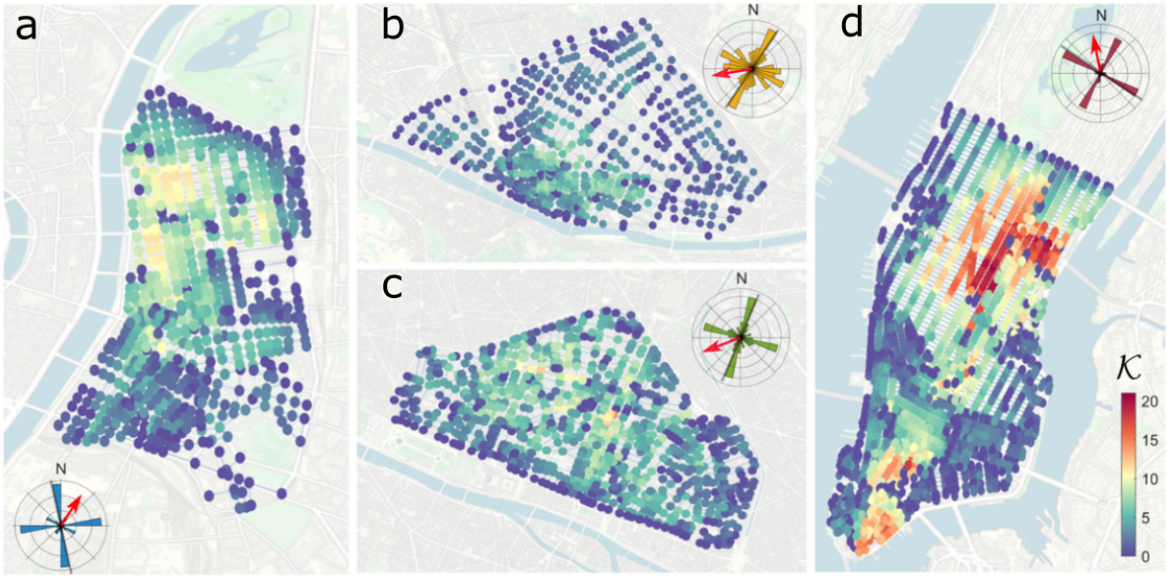

Figure 4.1: Vulnerability maps for (a) Lyon, (b) Firenze, (c) Paris, and (d) New York for a wind direction of 45° with respect to the main axis of the urban fabric. The polar histograms in the insets report the distribution of street orientation, while the red arrows represent the wind direction with respect to the street network.

as a spreading source) in the network for eight different wind directions ($\Phi = 0°$, 45°, 90°, 135°, 180°, 225°, 270°, 315°). In this way, we compute a characteristic *cdf* for each city. The intercept of the *cdf* represents the nodes with null vulnerability. These are usually located at the downwind edges of the delimited urban area, where a gaseous release is blown away by the wind without affecting other streets. According to the mean values (vertical dashed lines) of the distributions, New York is the most vulnerable city on average, while Firenze is the most protected. The vulnerability of New York and Lyon are the most sensitive to changes in wind direction, as shown by Fig. 4.2.b, where a polar histogram reports the mean vulnerability for each city for the eight directions of approaching wind. In general, the spreading potential is more effective when the wind is oblique ($\Phi = 45°$, 135°, 225°, and 315°) to the main orthogonal axes of the street network, as evidenced by the higher vulnerability observed for the dark gray sectors of Fig. 4.2.b.

The reasons for the different resilience of cities (and their patterning) to gas propagation are embedded in the centrality metric adopted to compute the above presented results. In the metric definition (Eqs.3.1-3.5), the key factors for node vulnerability can then be analytically recognized: the highest vulnerabilities are achieved when the set of reachable nodes from the source node is large, and the paths connecting the source and the reachable nodes ($\mathcal{D}$) are short, i.e. the propagation cost (w) along the paths is minimal. In other words, the spots in a city

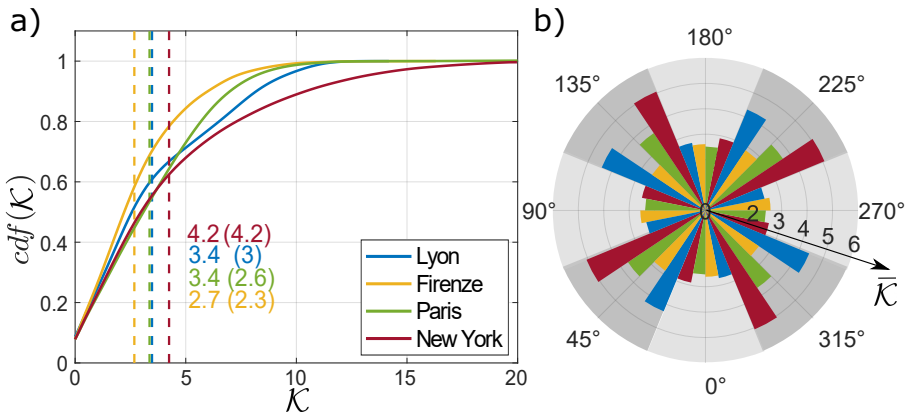

Figure 4.2: a) *Cdf* of node vulnerability for the different cities under eight different wind directions. The mean vulnerability is shown as a dashed line and reported numerically together with the standard deviation (in parentheses). b) Mean vulnerability of city networks for each wind direction.

with the highest spreading potential are those from which a toxic plume can reach many other locations with significant concentration. Going beyond the vulnerability results presented above, we aim to decompose the aforementioned elaborate and meaningful quantities (the set of reachable nodes, the shortest paths, the propagation cost) in elementary properties of the urban area in order to link the vulnerability of a city to its tangible characteristics.

We start by disassembling the propagation cost associated to each street, that describes the decay of concentration that the plume undergoes when it propagates along the street. As detailed in Eq. 3.1, the propagation cost is a function of the geometry of the street canyon, i.e. its length (L) and height (H), and of the mass transfer velocity of pollutants towards the atmosphere above roof level (u_d) and along the longitudinal (u_{st}) axis of the street. According to [Soulhac et al., 2008] and [Salizzoni et al., 2009], these two velocities can be parametrized as a function of the external wind intensity, the cosine ($\cos(\theta)$) of the angle between the wind direction and the orientation of the street, the geometry of the street canyon (its length, height and width W) and the aerodynamic roughness of building walls. Assuming constant wind forcing and aerodynamic resistance of the surfaces, the parameters L, H, W, $\cos(\theta)$, remain the relevant building blocks for the propagation cost along a street.

While propagation in a single street canyon (i.e. the propagation cost) has been easily broken down into its basic elements, the information enclosed in the shortest paths ($\mathcal{D}$) and in the set of reachable nodes from the source is much more challenging to trace back to evident properties of the city. These quantities depend

on the sequence of streets that must be traveled to connect a source node to the surrounding nodes, i.e. on the way the streets are interconnected. The information is thus primarily topological. However, we point out that the interconnectivity of the network is not frozen, but dynamic, as it is given by the reaction of the urban structure to the meteorological forcing, which is the direction of the external wind. Thus, we look for tailored and simple indicators that can express the topological component of the vulnerability by starting from the directed street network of a city, with the links directed according to the orientation of the approaching wind (link direction is simply obtained as projection of the external velocity along the axis of each street).

Focusing on a node as spreading source, we infer that the number of links in its downwind area gives a first estimate of the potential for a release in the node to affect many other locations in the network. We delimit this downwind area of the source node as its *n-hop* neighborhood [Smilkov and Kocarev, 2012, Maglaras and Katsaros, 2012], i.e. as the subnetwork composed by the nodes that are reachable from the source via at most n hops along the directed links (see Section 1.1). We propose the number of links in this neighborhood (r) as a suitable measure of reachability from the node. This reachability depends upon three features: i) the local structure of the street network, ii) the direction of the wind, and iii) the topological distance n. The topological distance n is chosen as the value that optimizes the correlation in the regression model that will be presented below, in Eq.4.1. For the analysis presented here, the neighborhood properties are suitable to predict the spreading potential of the node when $n = 8$, i.e. when the neighborhood is extended up to an $8 - hop$ topological distance from the node. Evidently, the extent of the neighborhood, n, depends on the initial concentration at the source node (c_0) and on the threshold concentration for contamination to be relevant (c_{th}). As the ratio c_0/c_{th} increases, the phenomenon involves a larger area. Accordingly, the optimal distance for the delimitation of the node neighborhood increases as well (Fig. 4.3).

Once the $n - hop$ neighborhood of a node is delimited, the number of links r is not exhaustive in giving information about the properties of the paths connecting the source to the other nodes of the neighborhood. For the same r, different structures of the neighborhood can take place (see Fig. 4.3.b), with consequent different outcomes for the propagation process that we are breaking down to basic components. The higher the branching of the neighborhood, the higher the potential concentration for the r links, as they are topologically closer to the source. This feature can be accounted for by means of a simple branching index (b) for the node neighborhood. The branching index assesses whether the neighborhood structure is more linear or more branched (see the two examples of neighborhood in Fig 4.3.b). It can be defined as the average outdegree (see Eq. 1.3) for the internal nodes belonging to the $n - hop$ neighborhood [Boccaletti et al., 2006].

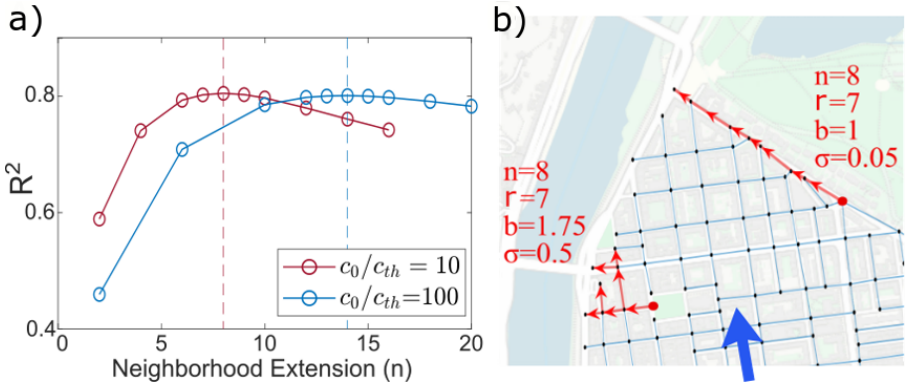

Figure 4.3: a) Coefficient of determination for the regression model as a function of the extent of the node neighborhood for two concentration scenario: $c_0/c_{th} = 10$ and $c_0/c_{th} = 100$. b) Estimate of the topological parameters (r, b, σ) for two different nodes of the street network in Lyon, for the same wind scenario (the orientation of the wind is reported as a blue arrow).

The disassembling analysis presented above suggests that the spreading potential of a node, and thus its vulnerability, mainly depends on the topological parameters r and b and on the geometrical characteristics of its neighborhood. We define here the geometrical parameters $\mathcal{L}$, $\mathcal{H}$, $\mathcal{W}$, Θ as the local averages (over the *n-hop* neighborhood) for the length (L), height (H), width (W), and orientation ($\cos(\theta)$) of the street canyons.
In adopting averaged geometrical properties, we are assuming that these characteristics are rather homogeneous in the surroundings of a node. While the height, width and length of the street canyons are actually quite uniform on a local scale, especially in European city centres, the same does not apply to the orientation of the streets. The streets of a neighborhood intersect each other at different angles (e.g., at 90° in grid plans), and the intensity of the wind in the streets changes strongly with their orientation. Low wind streets act as bottlenecks in the propagation paths, thus strongly influencing the spreading dynamics. For this reason, the standard deviation of street orientation in the neighborhood (σ) is expected to be an additional topological index of node vulnerability.

Notice that the *n-hop* distance can be considered as an additional topological parameter that takes into account the size of the toxic release. Since in this work the concentration scenario is fixed, this parameter keeps constant and is absorbed in the other predictors.

To assess whether the identified parameters are valuable basic elements of node vulnerability ($\mathcal{K}$), we perform a regression analysis adopting a simple (but versatile) non linear model of the form:

$$\mathcal{K}_{pred} = \alpha \mathcal{L}^{\beta} \mathcal{H}^{\gamma} \mathcal{W}^{\delta} \Theta^{\epsilon} r^{\zeta} b^{\eta} (1-\sigma)^{\lambda}. \tag{4.1}$$

We estimate the coefficients α to λ by means of a nonlinear least square technique (namely the *fitnlm* function in MATLAB) that minimizes the sum of the squares of the residuals between $\mathcal{K}$ and $\mathcal{K}_{pred}$. The p-values for the coefficients tend to zero, indicating that the relationships between the independent variables and the observations are statistically significant. Note that in Eq. 4.1 we adopt $1-\sigma$ as predictor, instead of σ, to avoid null entries, as σ takes value in [0 1). To explain the reason for this range for σ, we point out that the angle between the wind direction and the street axis (θ) is defined in $[-90^\circ\ 90^\circ]$. As a consequence, the cosine of the angle varies in [0 1] and its standard deviation (i.e. σ) varies in [0 1).

The scatter plot in Fig. 4.4 suggests that 80% of the spreading capacity ($\mathcal{K}$) of a spot in a city can be grasped from the basic geometrical and topological characteristics of the city that are included in the model for $\mathcal{K}_{pred}$. To identify the most influential parameters in the regression, we evaluate the gain in the coefficient of determination R^2 as they are progressively included in the model (red circles in the inset). The quantities are entered in order to optimize R^2 at each addition. Alternatively, the role of each parameter can be evaluated adopting the concept of unique contribution (triangles in the inset), i.e. the loss in the coefficient of determination induced by the exclusion of the parameter from the model [Judd et al., 2011]. Both analyses reveal r and σ as the main indicators for the vulnerability of a node. Actually, more than 60% of the total variance (panel a of Fig. 4.4) is explained by these two parameters, unveiling the crucial role of topology in governing the dynamics of pollutants in urban areas. The effect of the geometrical properties ($\mathcal{L}$, $\mathcal{H}$, $\mathcal{W}$, Θ) of the street canyons is secondary. Among these, the contribution of the building height ($\mathcal{H}$) is the most remarkable.

Given these results, it is enlightening to show some tangible examples of how the three simple indicators r, σ and $\mathcal{H}$ dominate urban vulnerability. We wonder which of these properties determine the distinct vulnerability of neighboring areas belonging to the same district, and which ones differentiate the resilience of cities with a different urban history.

In Fig. 4.5.a, the influence of the key parameters r, σ and $\mathcal{H}$ on the vulnerability of Midtown and Downtown Manhattan, for a wind direction $\Phi = 45^\circ$, can be grasped at a glance. In panel b, high street reachability (r) is observed in the central part of Midtown, in the heart of Downtown, and near Wall Street. An homogeneous distribution in the orientation of the streets with respect to the incident wind (low values for σ and thus high $1-\sigma$) is especially found in Midtown (panel c). Finally, in panel d, high-buildings ($\mathcal{H}$) distinguish the Financial District and East Midtown. In line with the results of the regression model shown in Fig. 4.4, a positive correlation is observable between the most vulnerable areas (circled areas comprising the nodes with highest $\mathcal{K}$ in panel a of Fig. 4.5) and those with the highest values for the three indicators. In these areas, high buildings inhibit the vertical exchange of pollutants between the streets and the atmosphere

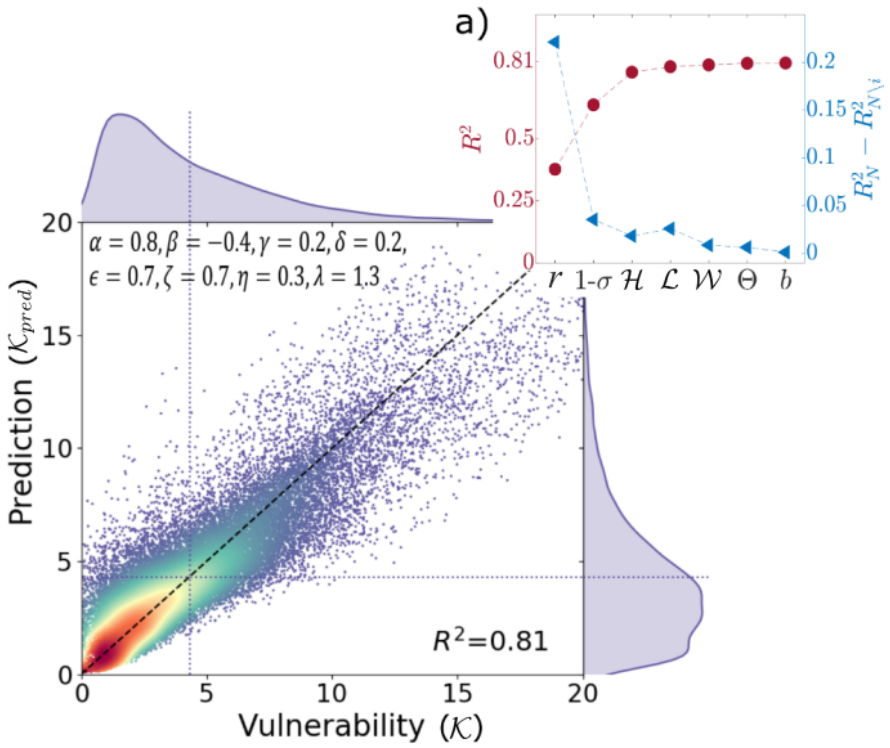

Figure 4.4: Correlation of node vulnerability with basic geometrical and topological parameters of the street network. Color (blue to red) is associated to point density. a) Left *y-axis*: trend of the coefficient of determination R^2 as the urban indicators are progressively included in the model. Right *y-axis*: unique contribution of the indicators.

above [Kovar-Panskus et al., 2002a, Fellini et al., 2020a], thus limiting concentration decay along the propagation paths and facilitating large-scale contamination. Moreover, the great number (r) of streets topologically close to the node increase the impact of the release. The effect of σ is significant especially for the vulnerability of Midtown. Here, since $\Phi = 45°$ and the street network is regular, the cosine of the wind-street angle θ is almost the same for all the streets. As a consequence, the standard deviation of $\cos(\theta)$ (i.e. σ) is low and the predictor $1 - \sigma$ is high. Physically, this entails that the wind flows with a similar intensity through the canyons and the propagation takes place along both the dominant and lateral segments [He et al., 2019], thus favoring the spread over large areas. Although high values of $\mathcal{H}$ and $1 - \sigma$ can be detected in the North-East corner of Midtown too, here the vulnerability is mitigated by a higher discontinuity in the urban pattern (low r). This feature, together with the great overlapping of red areas in panel a with those in panel b, evidences the key role of street reachability (r) in the heterogeneity of vulnerability between areas of the same district.

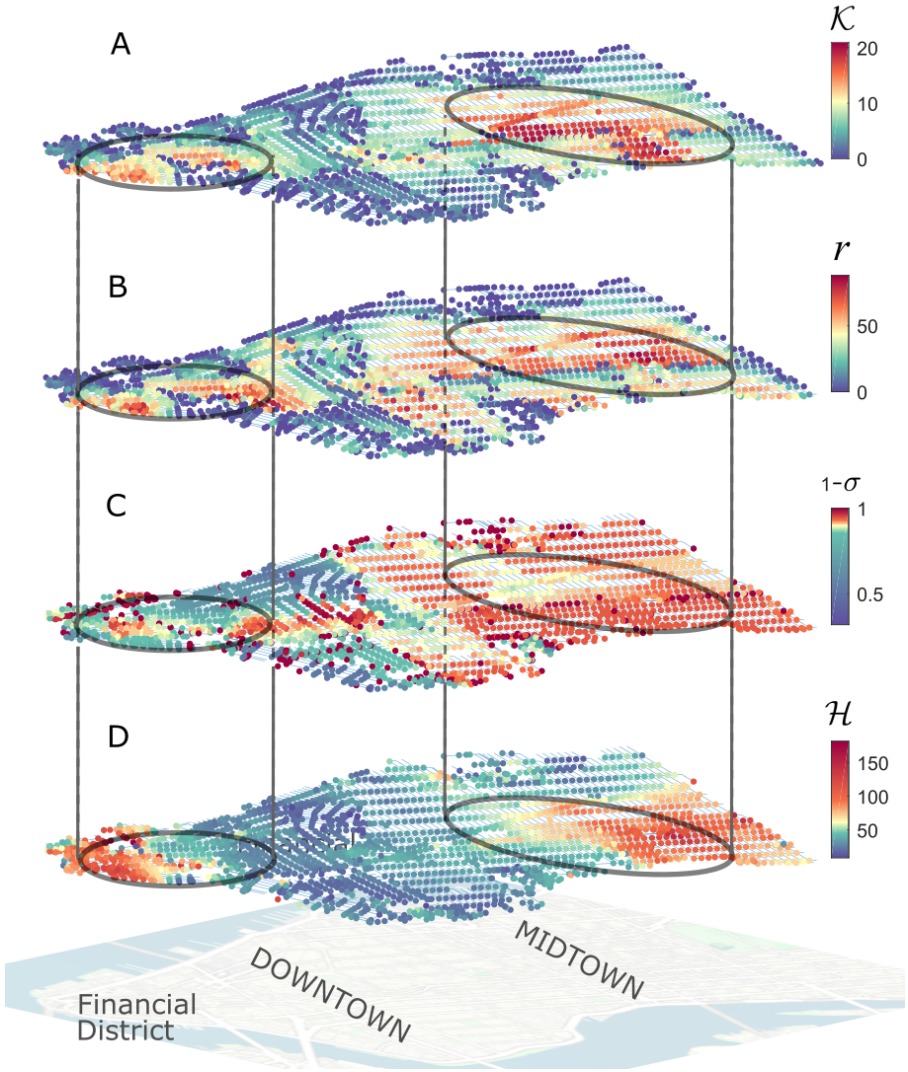

Figure 4.5: Street network of Midtown and Downtown Manhattan. Node color is associated to node vulnerability (expressed in terms of centrality $\mathcal{K}$), and to its key indicators: street reachability (r), inhomogeneity in street orientation (σ), and average height of buildings in the node neighborhood ($\mathcal{H}$).

From these observations, we can move to a broader view and investigate the structural fragility of a city as a whole. In Fig. 4.6.a-c, for each city, we report the probability density function (*pdf*) of the key parameters r, $1-\sigma$ and $\mathcal{H}$. The statistics are calculated over the eight different wind directions already presented in Fig. 4.2.b. In panel a, the distributions for the four cities are quite similar but the tails of the *pdfs* highlight that the highest values for street reachability (r) occur in the street networks of Lyon and New York. The homogeneity in street

orientation with respect to the wind (panel b), expressed by $1-\sigma$, exhibits a bimodal distribution and a slightly higher mean for the regular street network of New York. The two peaks are associated to distinctive wind scenarios, as will be discussed below. Also in this case, from the observation of the tails of the *pdfs*, we notice that high values of the vulnerability indicator (in this case $1-\sigma$) are more probable in Lyon and New York. Finally, the distribution of building height (panel c) presents the most marked difference between the considered architectures, with high-rise buildings contributing to the heavy *pdf* tail of Manhattan. Comparing these results with those in Fig. 4.2.a, Manhattan's greatest vulnerability appears to be due to the greater depth of the urban canyons (high $\mathcal{H}$) and the greater homogeneity, on average, in wind-street orientation (high $1-\sigma$). Conversely, the medieval structure of Firenze, with higher heterogeneity in street orientation (low $1-\sigma$) and low buildings (low $\mathcal{H}$), enhances street ventilation and hinders propagation over long distances. Moreover, the tails of the *pdfs* for r and $1-\sigma$ reveal the role of topology in the higher variability of vulnerability values (given by the standard deviation of the *pdfs* in Fig. 4.2) for the street networks of Lyon and Manhattan.

After discussing the behavior of the single parameters, we assess the synergistic contribution of the three quantities. To this aim, we define a simple correlation index $\rho = \widehat{r} \cdot (1-\widehat{\sigma}) \cdot \widehat{\mathcal{H}}$, where the hat denotes a *min-max normalization* of the parameters. For the urban areas of Manhattan, Lyon, Paris, and Firenze, ρ gives 0.039, 0.017, 0.012, and 0.011, respectively. This ranking complies with the ranking inferable in Fig. 4.2 for the average vulnerability of the cities. This result confirms that vulnerability occurs when the three parameters are correlated, as already evidenced in Fig. 4.5.

To make the picture more fascinating, it is worth noting that the role of topology, shown above as key, is not constant but dynamic, as it varies according to the direction of the wind impacting the urban fabric. In panels d to f of Fig. 4.6, the *pdfs* of r, $1-\sigma$ and $\mathcal{H}$ are distinguished for four wind directions ($\Phi = 0°$, 45°, 90° and 135°). For each angle, the statistics are calculated over the examined cities, together. Although wind orientation alters the direction of the network links, and thus the delimitation of the *n-hop* neighboring area of each node, street reachability (panel d) and building height (panel f) remain statistically invariant for the different wind directions, suggesting a rather isotropic structure of the urban fabric. On the other hand, the variability in street orientation with respect to the wind (panel e) presents two distinctive trends for wind directions aligned with or oblique to the main axes of the street network. To explain this behavior, we refer to the simple case of a grid-like urban plan, like Manhattan's plan. When $\Phi = 0°$ or 90°, the cosine of the angle (θ) between the street and the wind direction mostly switches between 0 (for the orthogonal streets) and 1 (for the streets aligned with the wind), resulting in a high standard deviation over the neighborhood (low $1-\sigma$). When $\Phi = 45°$ or 135°, instead, the incident angle $\cos(\theta)$ mainly takes intermediate values,

leading to higher values for $1-\sigma$. This distinctive behavior is clearly detectable in the two peaks observed for the regular grid of Lyon and New York in panel b. The left peak of the bimodal distribution corresponds to the scenarios with aligned wind directions, while the right peak occurs for oblique wind directions over the city. A more irregular street pattern in Firenze and Paris adds random contributions to the way the wind approaches the street, thus altering the bimodal shape (panel b). Going back to panel e, the greater homogeneity in wind-street orientation (higher $1-\sigma$) for $\Phi = 45°$ or $135°$ gives insights into the higher vulnerability found for the scenarios with these wind directions in almost all cities (dark gray sectors in Fig. 4.2.b). This result is confirmed by the correlation (ρ) between the three rescaled parameters ($\widehat{r}$, $1-\widehat{\sigma}$, $\widehat{\mathcal{H}}$). The correlation ρ is estimated separately for the different wind directions, but considering the nodes from the four urban areas together. For oblique wind directions, ρ is about double ($\rho = 0.035$) that for the aligned ones ($\rho = 0.018$).

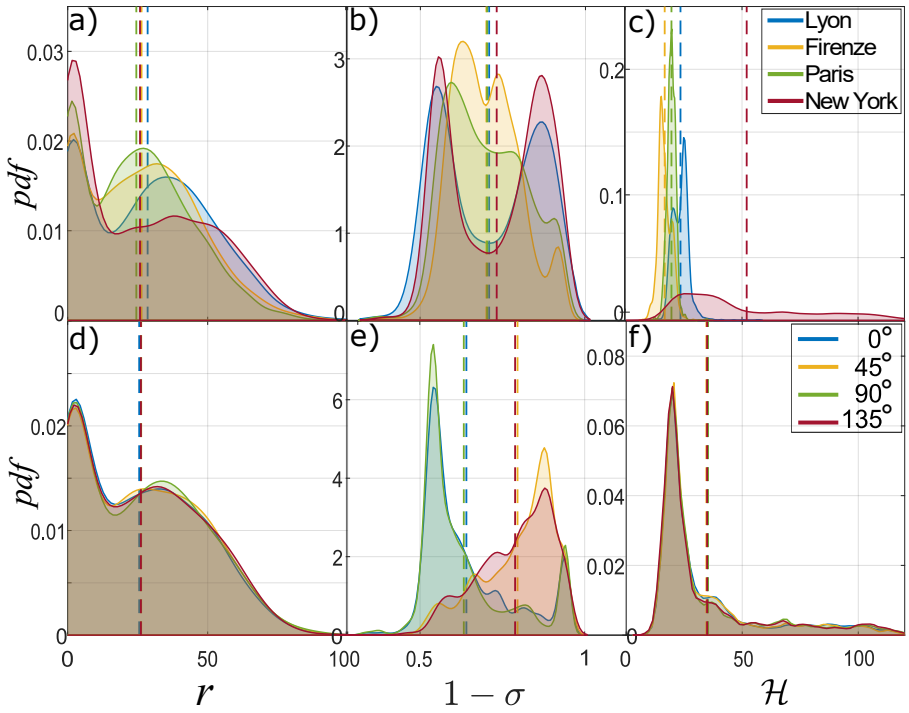

Figure 4.6: Probability density function of the key parameters r, $1-\sigma$, $\mathcal{H}$. In the first row, each *pdf* represents eight scenarios characterized by different wind directions over a single urban area. In the second row, each *pdf* includes vulnerability data from the four urban areas, for a specific wind direction.

Concluding remarks of Part I

We have presented a complex network approach to model diffusion processes in the urban atmosphere. Within the urban canopy, the wind flows along the street canyons and the transport of pollutants is strongly influenced by the structure of the city, i.e. by the orientation of the streets and by their interconnections. Based on these considerations, we have modelled the interaction between the city and the external wind as a weighted complex network whose links and nodes represent the streets and the street intersections, respectively. The direction of the links and their weights describe the direction and the intensity of the wind along the streets and the geometrical properties of the buildings that surround the street canyons.

Adopting a depth-first search analysis, we have implemented a spreading model on networks that simulates the propagation process from a point source. The developed method has proven useful for creating vulnerability maps that highlight the most vulnerable areas of a city, i.e. the areas from which the spread of a toxic substance, released at ground level, can harm more people.

The model proved to be fast-to-run and functional. In particular, the computational time was estimated to be up to 3 orders of magnitude lower than that of the well-known street network model SIRANE.

Starting from these results, we adopted a more adequate formalism and developed a centrality metric tailored on mass transport in flow networks. We derived the novel centrality following a physical-based rationale, and we assessed its effectiveness in the estimate of the spreading potential of a node. Besides the application to airborne releases in the urban canopy, the proposed centrality is suitable for the description of other confined (e.g., due to decay processes) spreading phenomena.

The formal foundation of dispersion as an epidemic on a network paved the way to the investigation of the key variables that drive the phenomenon. By disassembling the physical mechanisms in a set of simple factors, we found that the dispersion process is driven by the structural properties of the urban fabric. Two topological indicators of the area surrounding a node account for more than 60% of its spreading potential.

According to these findings, vulnerability is the result of the history of a city, its evolution and urbanization process. On the basis of this intrinsic fragility, practitioners such as urban planners and risk managers can act to control, prevent and

reduce risks related to airborne dispersion. In this sense, the proposed complex network approach is useful to rapidly assess the most vulnerable areas in a city, to analyse multiple scenarios that take into account various meteorological conditions, or different distributions of the residing population, and also temporary or permanent changes in the urban structure, such as the opening or closing of dead-end streets.

Part II

Street canyon ventilation

Introduction to Part II

The prediction of pollutant transfer within and above a street canyon is crucial to predict air quality in cities and develop urban dispersion models for operational purposes [Yamartino and Wiegand, 1986, Soulhac et al., 2011, Soulhac et al., 2012, Soulhac et al., 2017, Fellini et al., 2019]. The street canyon is the fundamental unit of the urban geometry. It is composed by a narrow street flanked by buildings on both sides, creating a canyon-like environment. In street canyons, the concentration of pollutants is high due to the presence of (ground level) vehicular and anthropogenic emissions and to the weak air ventilation caused by a recirculating motion between the buildings. The close proximity between emitters (vehicles, chimneys) and receptors makes these regions extremely vulnerable to health risks [Hertel et al., 2001]. Generally, the maximum concentration occurs when the wind blows perpendicular to the street canyon, inducing a recirculating flow that confines the transport of pollutants.

While horizontal advection at the lateral ends of a street canyon is the dominant ventilation mechanism [Carpentieri et al., 2012a] for longitudinal and oblique wind directions, when the wind is perpendicular to the street, the air quality mainly depends on the vertical pollutant exchange with the atmosphere above roof-level. This vertical transfer is influenced by different dynamical conditions and geometrical parameters of the street canyon. The effect of the cavity geometry on the flow dynamics within the canyon has become a classical case-study in fluid mechanics. A number of works [Hussain and Lee, 1980, Oke, 1988, Jeong and Andrews, 2002, Assimakopoulos et al., 2003] has demonstrated that the formation of secondary vortices in narrow cavities inhibits the canyon ventilation. The numerical studies of [Murena and Mele, 2016] and [Llaguno-Munitxa et al., 2017] evidenced the role of roughness elements (e.g., balconies) on the building walls in reducing the pollutant transfer from the street to the above atmosphere. In addition to the influence of large and small geometrical scales, the efficiency of street canyon ventilation has been investigated with respect to the role of the external turbulence [Salizzoni et al., 2009, Salizzoni et al., 2011], and the effect of traffic induced turbulence on dispersion processes within the street [Solazzo et al., 2008].

Besides the analysis of these dynamical mechanisms, a growing interest has been devoted to the study of buoyancy effects on the air flow within the canyon. Thermal fluxes generate buoyancy forces that have a relevant influence especially in low wind condition. These effects are primarily associated with solar radiation which induces temperature differences between the canyon walls of about 15 K at mid latitudes [Louka et al., 2002, Offerle et al., 2007]. A deep understanding of the interaction between wind and buoyancy forces within the streets is crucial for the implementation of natural or hybrid ventilation techniques [Hunt and Linden, 1999, Georgakis and Santamouris, 2006], for the improvement of energy performance in buildings [Santamouris et al., 2001], and for mitigating the heat island effect through

in-canyon vegetation [Alexandri and Jones, 2008, Lee et al., 2016] and urban planning [Theeuwes et al., 2014].

In this regard, the presence of vegetation inside street canyons is gaining interest in recent years, as vegetation has a deep and positive effect on urban microclimate. However, from the aerodynamic point of view, trees can obstruct the flow and reduce canyon ventilation.

In this part of the thesis, we focus on street canyon ventilation and we investigate how the canyon geometry, the differential heating of the building façades and tree planting in a street influence pollutant dispersion within the canyon.

Chapter 5

Effect of cross-section geometry and wall heating

The work described in this chapter has been partially derived from [Fellini et al., 2020a].

In this chapter, we investigate the combined effect of street canyon geometry, wall roughness and differential heating of the building façades on street canyon ventilation.

In the last decades, several numerical and experimental studies have been performed to investigate flow and dispersion dynamics in urban street canyons. However, few of those investigated the role of heat fluxes generated by temperature difference between the canyon walls.

Variations in the flow streamlines within a street canyon due to heat fluxes at the canyon walls and bottom were investigated numerically by RANS models (e.g., [Sini et al., 1996, Kim and Baik, 2001]). *Sini et al.* found that when a wind is blowing perpendicular to the canyon and the downstream wall is heated, two counter-rotating vortices are formed. The CFD simulations reported in [Xie et al., 2007] confirmed these findings but observed that these secondary structures were overestimated with respect to the wind-tunnel observations of [Kovar-Panskus et al., 2002b]. In [Solazzo and Britter, 2007], the authors simulated weak buoyancy effects in the canyon to estimate a typical vertical exchange velocity. More recently, LES simulations [Cai, 2012, Li et al., 2012, Li et al., 2016] provided insights into the turbulence structure within a heated canyon, and on the effect of three dimensional surface heating [Nazarian et al., 2018]. With numerical simulations, a great variety of scenarios can be analysed. However, these simulations are very sensitive to the domain size [Cui et al., 2004], to the sub-grid model and to the treatment of the boundary conditions.

Field studies on the effect of thermal fluxes in street canyons were conducted in different European and Asian cities [Nakamura and Oke, 1988, Louka et al., 2002,

Offerle et al., 2007, Niachou et al., 2008]. In these studies, the influence of thermal fluxes seemed to be limited to a thin layer close to the heated wall, and the occurrence of secondary recirculating structures was not detected.

Few wind-tunnel experiments were performed to investigate the role of wall heating on the flow structure within a street canyon. This is mainly due to practical difficulties in complying with the similarity criteria for the internal Froude number, i.e. the dimensionless number expressing the ratio of inertial to buoyancy forces (see Section 5.1.3). In fact, very large temperature differences within the canyon are required to reproduce realistic buoyancy conditions in wind tunnel models with high scaled street canyons. In [Uehara et al., 2000], the authors analysed the effects of atmospheric stability on the the flow within a street canyon, by heating the floor of the wind tunnel. *Kovar-Panskus et al.* proposed a wind-tunnel experiment with the direction of the wind normal to the canyon and a differential heating of the cavity walls [Kovar-Panskus et al., 2002b]. In the experiment, the downstream wall of a square canyon was heated and four external velocities were applied in order to generate different buoyancy conditions. They observed the formation of a stagnant flow at the bottom of the cavity, as the Froude number decreases. By means of PIV (Particle Image Velocimetry) measurements, *Allegrini et al.* investigated the flow field in a square cavity for a wider range of configurations: heating of the (i) upstream wall, (ii) downstream wall, (iii) canyon ground, and (iv) all three surfaces together [Allegrini et al., 2013]. The formation of a second counter-rotating vortex was evident for the configuration with the heating of the windward wall. In all cases, an increase in the turbulent kinetic energy inside the cavity was measured. Similar results for the flow field were found in [Marucci and Carpentieri, 2019], where in addition the effect of stratification in the approaching flow was analysed. By the release of a tracer from a ground level source, dispersion measurements were also performed.

Besides these recent works, the shortage of laboratory experiments represents a significant limitation for the validation of the widespread numerical studies. To date, we observe the lack of a comprehensive analysis of the combined effect of the street canyon geometry and the buoyancy conditions within it. These factors proved to be key in determining the fluid dynamical conditions in the street canyon.

By means of wind-tunnel experiments, we evaluate in this chapter how different geometry and heat conditions within a two-dimensional street canyon determine the flow and the dispersion of a passive scalar within the cavity itself. To this aim, the flow field for a wind perpendicular to the canyon is analysed for eight different aspect ratios of the cavity in isothermal conditions. The effect of roughness elements on the canyon walls is also investigated for these configurations. For a square and a narrow cavity, thermal effects are examined. The upwind and downwind walls are alternatively heated and different thermal fluxes are experimented. The spatial coherence of the turbulent field is investigated by means of PIV. Steady and unsteady measurements of concentration are performed in the cavity with a

Flame Ionisation Detector (FID) system, in order to investigate both the spatial distribution and the temporal evolution of pollutants released at the ground level.

The variety of experimental configurations, the different measured quantities and their analysis shed light on the fluid-dynamical mechanisms that govern the wash-out of a two-dimensional street canyon for a perpendicular wind direction.

5.1 Methodology

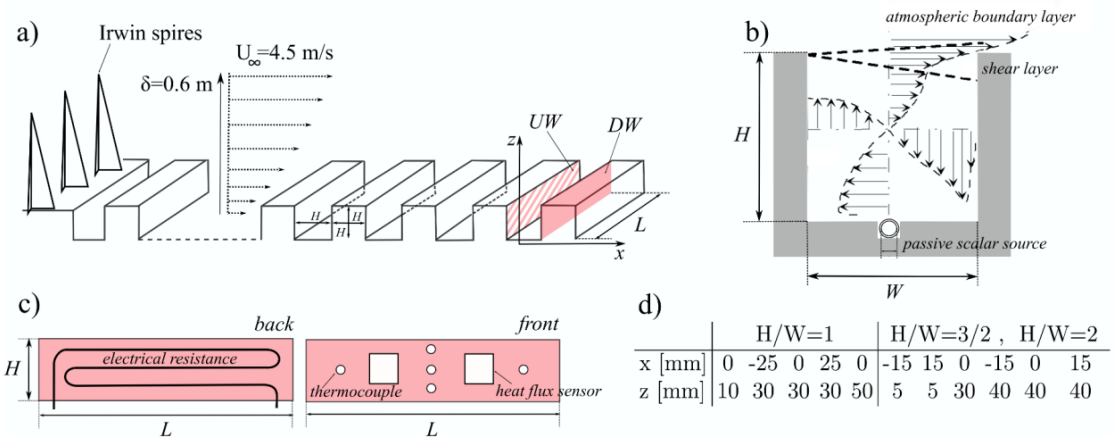

	H/W=1					H/W=3/2 , H/W=2					
x [mm]	0	-25	0	25	0	-15	15	0	-15	0	15
z [mm]	10	30	30	30	50	5	5	30	40	40	40

Figure 5.1: a) Overview of the wind tunnel installation with the position of the street canyon. b) Sketch of the canyon cross-section with the qualitative representation of the two-dimensional flow. The line source is located in a slot cut in the tunnel floor. c) Sketch of the set-up for the configurations with heating of the downwind wall (DW). d) Horizontal (x) and vertical (z) coordinates of the points where the wash-out curves were measured.

5.1.1 Experimental set-up

The experiments were performed in a closed-circuit wind tunnel (Fig. 5.1) at the laboratory LMFA (Laboratoire de Mécanique des Fluides et d'Acoustique) at the École Centrale de Lyon. The test section of this tunnel is 8 m long, 1 m high and 0.7 m wide. Irwin spires [Irwin, 1981] with a height of 0.4 m were placed at the entrance of the test section. A total of 65 aluminium bars were arranged normal to the wind direction, along the entire length of the wooden floor of the wind tunnel. The bars were of section 0.06 m x 0.06 m, with a length (L) of 0.7 m extending over the entire width of the tunnel, and with a spacing of 0.06 m between them. In this way, we obtained a regular set of parallel street canyons with a constant aspect ratio of one, with the exception of the canyon where the measurements were taken which

had a variable aspect ratio. This canyon was located 5 m downstream of the vortex generators, i.e. downwind of an urban canopy of about 40 canyons. In this way, the fully development of the approaching flow was guaranteed [Meroney et al., 1996, Pavageau and Schatzmann, 1999] and a neutral atmospheric boundary layer with depth $\delta = 0.6$ m was obtained. The blockage ratio of the model to the cross-section of the wind tunnel was 6%. Before starting the experiments, we ensured that the incident velocity field was two-dimensional by measuring velocity profiles upstream and downstream of the canyon at different transversal positions using a hot wire anemometer (see [Salizzoni et al., 2008] for a complete description of the velocity field in this experimental set-up). These velocity profiles confirmed that the flow field was uniform in the transverse direction, with variations of less than 1% for the mean flow and 5% for the turbulence quantities. Moreover, concentration measurements were performed along the longitudinal axis of the canyon at various heights (with the linear source of tracer placed at ground level) demonstrating the two-dimensional nature of the mean concentration field within the canyon.

The height (H) of the canyon in which the measurements were performed was 0.06 m (i.e. one tenth of the boundary layer height), while its width (W) varied between 0.03 m and 0.06 m.

The lower part of the vertical profile of the mean horizontal velocity that develops above the transversal bars can be modelled by the classic logarithmic profile introduced in Eq. 2. The incoming wind profile was kept constant in this study. The free stream velocity at the top of the boundary layer (U_∞) was kept fixed and equal to 4.5 m/s. The friction velocity $u_* = 0.22$ m/s was determined from the Reynolds stress profile, while $z_0 = 0.1$ mm and $d = 57$ mm were evaluated by fitting the logarithmic profile to the experimental data in the lower part of the boundary layer flow. Note that the incoming flow corresponds to that of Configuration 1 in [Salizzoni et al., 2008], to which the reader is addressed for further details on the statistics of the velocity field.

A pollutant release was simulated by the injection of ethane from a linear ground level source placed at the centre of the canyon. The linear source was a porous polymeric tube with diameter of 4 mm, located in a slot cut in the tunnel floor so as not to alter the velocity field (see Fig. 5.1.b). The tracer gas supply was monitored continuously using a Brooks flow meter, and the experiments were performed with a mass flux of 2.8 mg/s (0.14 l/min), giving a mass flow rate per unit of length $\dot{M}_q = 4$ mg/s·m.

To investigate buoyancy effects inside the canyon, each lateral wall of the street canyon was heated at a time. A heating mat was attached at the back of the heated wall, inside the lateral aluminium bar (as shown in Fig. 5.1.c). Constant and controlled heat fluxes from the thermal resistance were produced exploiting Joule heating.

Experiments with roughness elements to the side walls were performed to analyse the effect of small scale geometry on the cavity flow. In these experiments, a

corrugated cardboard sheet was fixed to one or the other lateral wall of the canyon.

5.1.2 Measurement techniques

The velocity field within the cavity and in the lowest part of the boundary layer was measured using a Particle Image Velocimetry (PIV) system. Two coupled YAG laser sources provided pairs of laser pulses at a frequency of 4 Hz. The visualization light sheet was perpendicular to the canyon axis and measured 1 mm in width. The flow was seeded with micron-sized droplets produced by a smog generator. The observation field measured approximately 0.12 m x 0.12 m (2H x 2H), and was filmed at a resolution of 1280 x 1024 pixels. Due to the reflection of the laser light on the cavity surfaces, velocity measurements very close to the walls had to be discarded. However, the disturbed area consisted of a thin layer of one to two millimetres near the walls, thus not compromising the analysis of the velocity field as a whole. The images were processed using cross-correlation. The interrogation window was fixed at 16 x 16 pixels, providing a spatial resolution of about 1 mm x 1 mm. The interrogation areas overlapped by 50% so that in total, each velocity field computation yielded a set of 240 x 240 vectors. The velocity field was recorded with 1000 double frame images at a frequency of 4 Hz, i.e. two images were captured each 0.25 seconds, with a time interval of 30 μs between the two shots. From these 1000 instantaneous velocity fields, we computed for each (x, z) point reliable flow statistics up to the third order moment of the velocity field. Fig. 5.2 shows the convergence of the mean ($\overline{u}$), variance (σ_u^2) and skewness (Sk_u) of the horizontal velocity with the increasing number of samples.

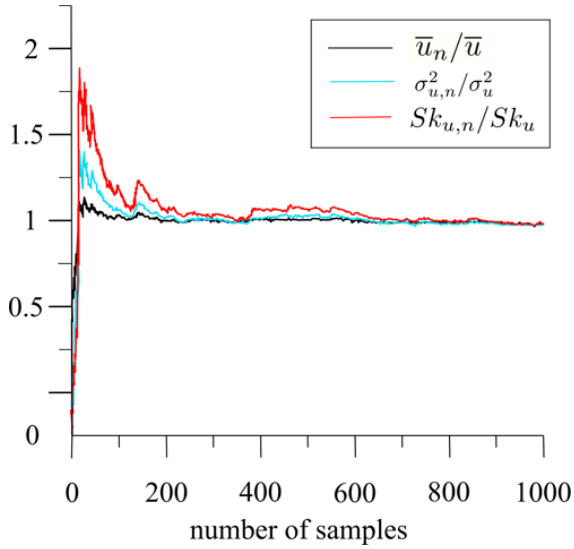

Figure 5.2: Convergence of the PIV statistics. $\overline{u}$, σ_u^2 and Sk_u are the mean, the variance and the skewness of the horizontal velocity calculated over 1000 samples at a fixed point; $\overline{u}_n$, $\sigma^2_{u,n}$ and $Sk_{u,n}$ are the same moments calculated over n samples.

By means of these measurements, we obtained the horizontal ($\overline{u}$) and vertical ($\overline{v}$) components of the mean velocity, their variances σ_u^2 and σ_v^2, and the mean vorticity field $\overline{\boldsymbol{\omega}} = (\partial\overline{v}/\partial x - \partial\overline{u}/\partial z)\widehat{\mathbf{y}}$. The turbulent kinetic energy field (TKE) was computed as TKE$= 0.5(\sigma_u^2 + \sigma_v^2)$. In this expression, the velocity variance in the third direction is missing as the velocity field is measured only in the plane perpendicular to the canyon axis. Notice that we follow here the notation proposed in the introduction of this thesis (Fig. 4), i.e. we use u, v to denote the components of the velocity vector along x and z.
While providing information on the spatial structure of the flow (e.g., the vorticity field), PIV system suffers some limitations when used to elaborate the turbulence statistics, since a lower number of samples per location is available compared to other measurement systems, as Hot Wire Anemometry (HWA) or Laser Doppler Anemometry (LDA) [Hyun et al., 2003]. Best practices were adopted to minimize the errors in the measurements [Adrian, 1997, Prasad, 2000]. Moreover, we tested the performances of the PIV system by comparing the vertical profile of TKE with measurements from an Hot Wire Anemometer system [Nironi, 2013]. Starting from these measurements, we estimated a percentage error almost everywhere below 5% (with peaks of 10%) for the TKE.

Concentration within the cavity was measured using a Flame Ionisation Detector (FID) system [Fackrell, 1980]. FID is commonly used for measurements in urban-like geometries [Pavageau and Schatzmann, 1999, Carpentieri et al., 2012a]. In FID systems, air containing hydrocarbons is aspirated continuously by means of a capillary tube, and injected in a hydrogen flame in a combustion chamber. Here,

the ions produced by combustion are detected by two electrodes and induce a current that is proportional to the concentration of hydrocarbons in the air. In this study, ethane was chosen as a passive tracer, since its molecular weight is nearly the same of air. To avoid the disruption of the local flow, a straight 30 cm long sampling capillary tube was mounted on the FID head, which was positioned above the test section so as not to affect the flow field. The sampling frequency of the FID signal was fixed at 1000 Hz [Nironi et al., 2015]. Due to the 30 cm long capillary tube, the frequency cut-off of the signal was around 400 Hz (Fig. 5.3), and thus the frequency response of the instrument was about 800 Hz [Marro et al., 2020]. Steady and unsteady experiments were carried out. In steady conditions, the in-

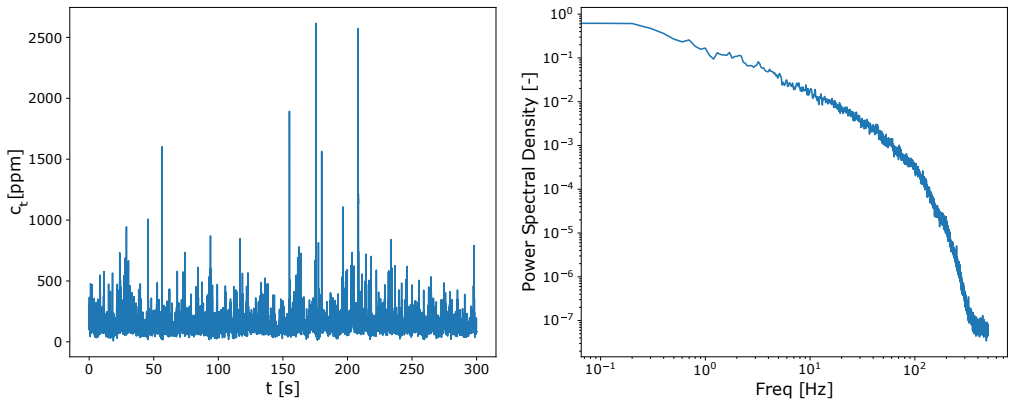

Figure 5.3: Concentration spectrum obtained from the FID signal measured in the centre of the cavity.

jection of ethane from the ground level source was kept constant and the mean concentration within the cavity was measured on a regularly spaced grid (1 cm x 1 cm). In each sampling point, a FID acquisition time of 60 seconds was sufficient to provide averaged statistics. $\overline{c}$ is used in the text to indicate the single-point time average of the concentration. The mean concentration field was then obtained by spatial interpolation between the sampling points. The experiments in unsteady conditions were performed to estimate the typical wash-out velocity of the cavity. As in [Salizzoni, 2006] and [Salizzoni et al., 2009], we measured the temporal evolution of ethane concentration at different positions within the cavity as it emptied. In Fig. 5.1.d, the position of the sampling points is reported. The experiment was performed as follows: (i) ethane was first injected into the canyon until the concentration field reached a stationary state; (ii) the injection of ethane was then interrupted by means of a valve; (iii) the temporal evolution of the concentration was recorded by the FID probe for a time interval of 15 seconds, in a single sampling point. For each sampling point, passages (i) to (iii) were repeated between 30 and 50 times to allow an ensemble average for the signal. By the subtraction of the

background concentration and the normalization to the initial value, i.e. the initial concentration in stationary conditions in the sampling point, the dimensionless (ensemble-averaged) wash-out curve was finally obtained.

For the experiments with heating of the side walls, the temperature difference ΔT between the walls were obtained by exploiting Joule heating at the thermal resistance fixed on the back of the heated wall (Fig. 5.1.c). Two heat flux sensors of size of 3 cm x 3 cm, thickness 0.3 mm, and sensitivity 5x10^{-3} $V/(W/m^2)$ were placed on the heated wall, on the side facing the canyon (as shown Fig. 5.1.c). For temperature measurements, 5 T-type thermocouples were placed on the heated wall (the position of the sensors is shown in Fig. 5.1.c) and a single thermocouple on the non-heated wall. Moreover, each heat flow sensor was also equipped with a thermocouple. Negligible effects in the immediate vicinity of the walls were observed in the flow field due to the installation of the thermocouples and the heat flux sensors.

The thermocouples and the heat flux sensors measured the temperature (T_w) and the thermal flux ($\dot{q}$) at the heated wall. Temperature remained on average constant over time ($\simeq \pm 1$ K). A maximum spatial difference of temperature of around ± 2 K degrees was observed along the longitudinal coordinate of the wall. The heat transfer coefficient (h_t) was also estimated from the Newton equation, which describes the heat transfer per unit surface through convection:

$$\dot{q} = h_t(T_w - T_0), \tag{5.1}$$

where $\dot{q}$ $[W/m^2]$ is the thermal flux per unit area, h $[W/m^2K]$ is the heat transfer coefficient, and T_w and T_0 $[K]$ are the wall and the reference temperature, respectively.

In Table 5.1, we report the aforementioned quantities for the configurations with heating of the downwind wall in both a square and a narrow cavity. For the temperature and the thermal flux at the heated wall, the average over the available sensors is reported.

Since a cooling system was not set up in the experiment, heating of the other surfaces of the cavity due to conduction -through the wooden floor of the wind tunnel- and radiation from the heated wall could not be avoided, but proved to be limited. Temperature measurements revealed a heating of the opposite wall of about 10% compared to that of the heated wall. This effect was more pronounced for the case of the narrow cavity but tended to decrease with T_w. Although acceptable for the purposes of the experiment, this heating slightly reduces the actual temperature difference between the walls, which is expressed as $\Delta T = T_w - T_0$ along this work.

5.1.3 Experimental conditions

Street canyon ventilation is expected to depend on the variables that characterize the turbulent flow within the street canyon. These are: the height (H) and the

	$\dot{q}$ $[W/m^2]$	T_w [K]	T_0 [K]	ΔT [K]	h_t $[W/m^2K]$
H/W=1	1031	371.2	301.0	70.1	14.7
	2250	472.2	301.7	170.4	13.2
H/W=1.5	735	369.3	301.2	68.1	10.8
	1321	437.8	299.8	138.0	9.6
	1659	468.7	302.4	166.2	10.0

Table 5.1: Thermal flux per unit area $\dot{q}$, temperatures of the heated wall (T_w) and of the external air (T_0), temperature difference (ΔT), and heat transfer coefficient (h_t) in the configurations with heating of the downwind wall.

width (W) of the canyon cross-section, the kinematic viscosity (ν) and the thermal (α) and mass (D_m) diffusivity of the fluid, a characteristic velocity scale ($\mathcal{U}$), the roughness height (h_r) of the canyon walls, the gravitational acceleration (g), the reference air temperature (T_0), and the surface temperature of the possible heated wall (T_w). Introducing the velocity u_d as the rate of vertical bulk exchange of pollutants between the street canyon and the overlying atmosphere, we can therefore seek to define the following dependence:

$$u_d = f(H, W, \nu, \alpha, D_m, \mathcal{U}, h_r, g, T_0, T_w), \tag{5.2}$$

which, according to the Buckingham Π theorem, can be expressed in the following non-dimensional form:

$$\frac{u_d}{\mathcal{U}} = f\left(\frac{H}{W}, \frac{h_r}{H}, Pr = \frac{\nu}{\alpha}, Sc = \frac{\nu}{D_m}, Re = \frac{\mathcal{U}H}{\nu}, Fr_i = \frac{\mathcal{U}}{\sqrt{gH\frac{\Delta T}{T_0}}}\right), \tag{5.3}$$

with $\Delta T = T_w - T_0$. The physics of the phenomenon depends on two geometrical parameters, and four dynamical parameters. The geometrical parameters are the aspect ratio (H/W) of the canyon cross-section and a characteristic roughness (h_r/H) of the canyon walls. These parameters account for the effect of large and small geometrical scales, respectively. The three dynamical parameters are the Prandtl (Pr), Schmidt (Sc), Reynolds (Re) and internal Froude (Fr_i) numbers. The definition of the velocity scale $\mathcal{U}$ in the Reynolds and Froude numbers is not trivial for a flow within a cavity. In [Kovar-Panskus et al., 2002b] and [Allegrini et al., 2013] $\mathcal{U}$ is assumed to be the velocity at the top of the external boundary layer flow (U_∞). However, this is not necessarily a characteristic scale for the flow in the canyon since the same U_∞ could produce different boundary layer flows, and therefore different canyon flows, depending on the roughness of the obstacles upwind the canyon. Other authors [Castro and Robins, 1977, Snyder, 1994] considered as velocity scale the wind speed at the building height (U_H). *Salizzoni et al.* observed that there is not a unique velocity scale that correctly characterizes the turbulent

flow within the canyon [Salizzoni et al., 2011]. They also found that the turbulent kinetic energy (TKE) within the cavity scales well on the friction velocity u_*. Since the wash-out process is expected to depend on the TKE [Salizzoni et al., 2009], we take, in this study, the friction velocity u_* as velocity scale.

The Prandtl and Schmidt numbers (see Equation 5.3) are almost constant within the range of temperature we consider in our experiments ($Pr \simeq 0.7$ and $Sc \simeq 0.9$). The Reynolds number undergoes slight variations due to small differences in the velocity profile realized in the wind-tunnel and to the increase of ν with temperature. In wall-heated configurations, sharp temperature gradients are measured in close proximity to the heated wall (within 0.5 cm from the wall), while the average temperature in the cavity increases by a maximum of 50 K with respect to the temperature outside the canyon. Taking into account the increase in ν with this temperature variation, we obtain Reynolds numbers based on the wind speed at the building height ($Re_H = U_H H/\nu$) in the range 5700-7200. In [Castro and Robins, 1977] and [Marucci and Carpentieri, 2019] it was shown that, for Re_H larger than 4000, no Reynolds number effects were discernible for the flow field within a cavity of unit aspect ratio. Considering a Reynolds number based on the free stream velocity ($Re_\infty = U_\infty H/\nu$), [Allegrini et al., 2013] obtained a Reynolds independent flow, in a square cavity, for Re_∞ above 13000. In our set-up, Re_∞ is in the range 14200-18000. The narrow street canyon is expected to be more vulnerable to the Re independency. However, in [Barlow and Belcher, 2002] the authors found a Re independent transfer velocity in a canyon with $H/W = 2$ for Re_H lower than those of this experiment. After these considerations, we can therefore assume that the flow is Reynolds independent in our experiment.

The experiments were performed for aspect ratios varying between 1 and 2. These are the typical geometries in European cities [Soulhac and Salizzoni, 2010]. The effect of roughness on the canyon walls was tested by adding small scale roughness elements on one or the other sidewall. Experiments with two different roughness scales (h_r) were performed: corrugated cardboard sheets with flute thickness of 2 mm ($h_r/H = 1/30$) and 5 mm ($h_r/H = 1/12$) were used to simulate an idealised façade roughness. Notice that a roughness scale of 5 mm on the 60 mm high canyon wall is representative of a characteristic balcony depth of 1.5 m in a street canyon with 20 m high side buildings [Murena and Mele, 2016]. Three heating configurations were investigated: (i) the isothermal case, (ii) the heating of the upwind (UW) wall, and (iii) the heating of the downwind (DW) wall. In the last two cases, different thermal fluxes were imposed at the heated wall. The resulting temperature differences ($\Delta T = T_w - T_0$) are reported in Table 5.2, with the corresponding Fr_i. The reference temperature T_0 ($T_0 \simeq 300$ K) varied from day to day, and was measured away from the street canyon.

It is worth noting that, since the velocity scale is different, the values of Fr_i considered here cannot be directly compared to those in [Kovar-Panskus et al., 2002b], [Allegrini et al., 2013], and [Marucci and Carpentieri, 2019]. However, taking U_∞

as velocity scale in order to compare the conditions of the different experiments, we obtain Fr_i values of an order of magnitude higher than those obtained in the above mentioned works, since the size of the canyon in our experiments is considerably smaller. Taking the Froude number as similarity criterion, our experimental conditions correspond to temperature differences from 4 to 15 Kelvin degrees in realistic street canyons flanked by 20-meter high buildings, and subject to a wind profile characterized by $u_* = 1$ m/s. These temperature differences are typically reached near sun-heated walls in Mediterranean cities [Louka et al., 2002, Offerle et al., 2007].

$\frac{H}{W}$	*No Roughness*							*Roughness*	
	No Heating	*DW Heating* (ΔT) [K]				*UW Heating* (ΔT) [K]		*UW*	*DW*
		70	140	170	240	140	240		
1	✓	$Fr_i = 0.62$	X	$Fr_i = 0.40$	$Fr_i = 0.34$	$Fr_i = 0.44$	$Fr_i = 0.34$	✓	✓
1.5	✓	$Fr_i = 0.57$	$Fr_i = 0.40$	$Fr_i = 0.37$	$Fr_i = 0.31$	$Fr_i = 0.45$	$Fr_i = 0.34$	✓	✓
1.3, 1.4, 1.6, 1.7, 1.8, 2	✓	X				X		✓	✓

Table 5.2: Experimental configurations. The check mark indicates the investigated experiments, while the X marks those not considered. The internal Froude number is specified for the configurations with differential heating of the walls. *UW* and *DW* stand for *Upwind* and *Downwind* wall, respectively.

5.2 Effect of large and small geometrical scale

5.2.1 Effect of the large geometrical scale

As well documented by previous experimental and numerical studies (e.g., [Mehta and Lavan, 1969, Hussain and Lee, 1980, Oke, 1988, Sini et al., 1996]), the topology of the mean velocity streamlines within the cavity varies with the canyon geometry. In our experiments, the mean flow shows that, for an aspect ratio H/W equal to 1, most of the cavity is filled by a large rotating cell, with its centre close to the cavity centre (Fig. 5.4.a). As the street aspect ratio increases, a second counter-rotating cell appears at the bottom of the cavity (Fig. 5.4.b-c). The velocities in this second vortex are much lower than those in the upper vortex. In our experiments, the transition from one main circulating cell to two counter-rotating cells emerges for an aspect ratio H/W greater than 1.8. For this aspect ratio, the sign of the vertical velocity profile in $x = 0$ (Fig. 5.5) changes three times, revealing that the second cell is fully established in the centre of the lower part of the canyon. A similar value (i.e. $H/W = 1.7$) was found numerically in [Sini et al., 1996], while in [Lee and Park, 1994] the authors found that this transition takes place for $H/W \simeq 2.1$. As will be discussed below, this transition depends on the amount of clockwise vorticity entering the canyon, i.e. on the approaching flow as well as

on the cavity aspect ratio. This explains why discrepancies on the H/W value for transition occur in the different studies.

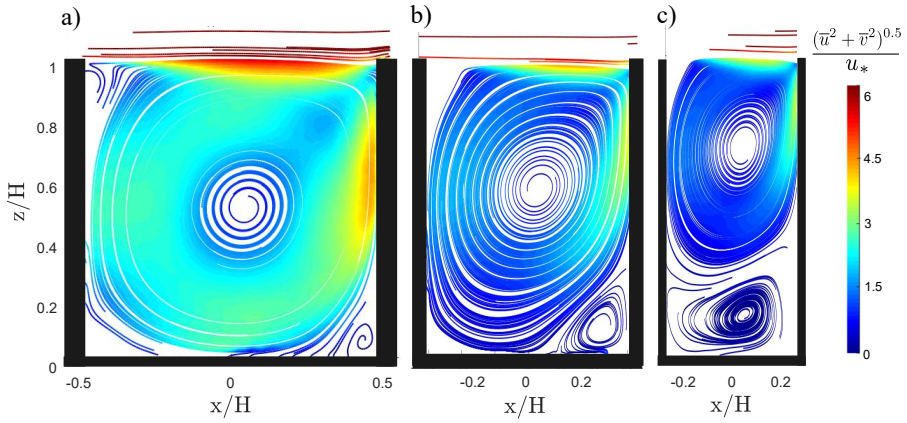

Figure 5.4: Streamlines of the mean velocity field for the aspect ratios (a) H/W=1, (b) H/W=1.5 and (c) H/W=2.

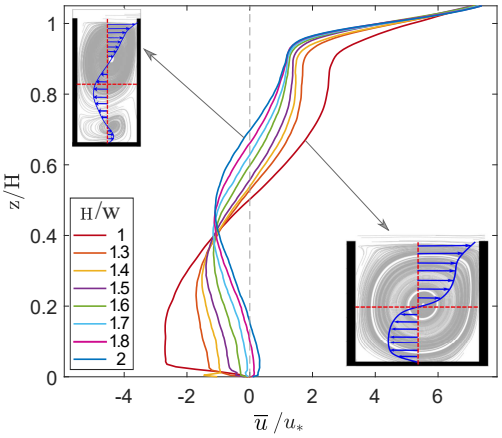

Figure 5.5: Vertical profile of the mean horizontal velocity at $x = 0$ for different aspect ratios.

In all the considered geometries, the turbulent kinetic energy within the cavity (Fig. 5.6) is up to an order of magnitude lower than in the external flow (i.e. for $z/H > 1$). This finding is in accordance with the experimental results obtained in [Salizzoni et al., 2011], [Allegrini et al., 2013] and [Marucci and Carpentieri, 2019]. In the here analysed configurations, the transversal bars are very close, so that the flow regime in the street canyon is a skimming flow [Oke, 1988]. In skimming flow, the size of the turbulent eddies that develop in the shear layer at the top of the cavity is limited to the horizontal spacing between the obstacles. Therefore, the

eddies in the shear layer are not sufficiently developed to couple with the turbulent eddies in the external flow [Leonardi et al., 2007, Salizzoni et al., 2011]. As a consequence, the shear layer shelters the flow within the cavity and the fluctuating flow within the canyon is isolated from the external flow. The main interaction between the cavity flow and the external flow is confined to the upper edge of the downwind wall. Here, a TKE plume spreads down into the cavity all along the canyon wall. For a square cavity, the plume reaches the downwind lower corner and it affects the entire cavity at the street level (panel a in Fig. 5.6). With increasing aspect ratios, the formation of the second counter-rotating cell inhibits the turbulence transfer in the lower part of the canyon (panel c).

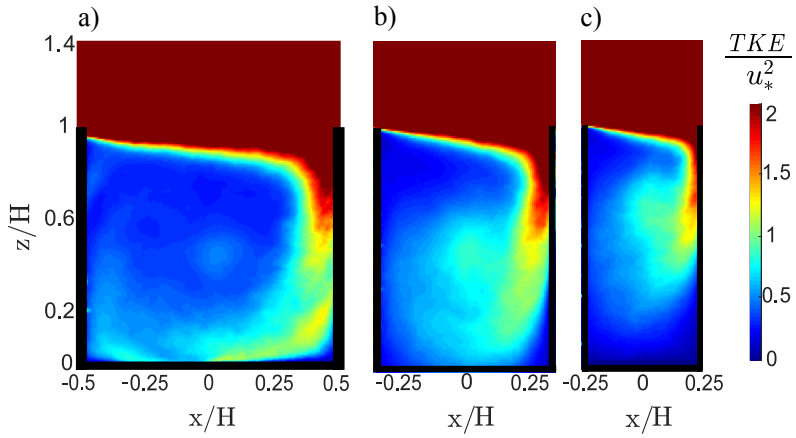

Figure 5.6: Turbulent kinetic energy for the aspect ratios (a) H/W=1, (b) H/W=1.5 and (c) H/W=2.

The formation of the second cell can be conveniently described in terms of vorticity more readily than in terms of velocity. The vorticity transport equation for a zero-divergence flow is

$$\frac{D\boldsymbol{\omega}}{Dt} = \boldsymbol{\omega} \cdot \nabla \mathbf{u} + \nu \nabla^2 \boldsymbol{\omega} - \mathbf{S_T} \times \mathbf{g}, \tag{5.4}$$

where $\boldsymbol{\omega}$ is the vorticity, $\mathbf{g}$ is the gravity vector, and $\mathbf{S_T}$ is a function of the temperature gradient: $\mathbf{S_T} = \nabla T/T$. The rate of change of vorticity (on the left-hand side of Equation 5.4) is therefore given by the stretching of vorticity due to flow velocity gradients (first term on the right-hand side), the diffusion of vorticity due to the viscous effects (second term on the right-hand side), and vorticity changes due to thermal gradients (last term of Equation 5.4). This latter is a source term given by the vector product between the thermal gradient and the gravity vector. Equation 5.4 is completed by appropriate vorticity conditions at boundaries [Banerjee et al., 2013, Olshanskii et al., 2015]. The main features of these boundary conditions can be grasped by observing the qualitative profile of the mean

velocity at the four boundaries of the domain (Fig. 5.7.a). The boundary layer that occurs along the walls of the cavity generates anticlockwise vorticity. Conversely, the shear layer at the top of the cavity generates a Kelvin-Helmholtz type instability leading to the formation of large-scale clockwise vortices that are entrained into the cavity. The same vorticity dynamics in a square cavity-driven flow were observed numerically [Chang et al., 2006, Shi et al., 2019] and experimentally [Lin and Rockwell, 2001, Mori and Naganuma, 2009] in previous works. To readily understand how the vorticity balance changes in a narrow cavity compared to a square one, a geometry-based interpretation is suggested. Given a constant height H of the canyon, the exchange surface (W) between the external flow and the canyon decreases when the aspect ratio H/W increases. As a consequence, the clockwise vorticity advected inside the cavity decreases as the cavity narrows. The anticlockwise vorticity at walls can be assumed proportional to the solid perimeter of the cavity ($2H + W$). This perimeter also decreases as H/W increases, but less rapidly than W. Consequently, as the aspect ratio increases, a surplus of anticlockwise vorticity accumulates at the bottom of the cavity (Fig. 5.7.c) and a second counter-rotating cell generates.
Note that assuming a change in the aspect ratio from 1 to 2 due to a doubling of H instead of a halving of W, the Reynolds number would double for the narrow cavity. In this case, changes in the vorticity balance due to different flow conditions are expected. Thus, the above presented geometry-based interpretation is valid under the hypothesis of a constant Reynolds number for the two geometries.

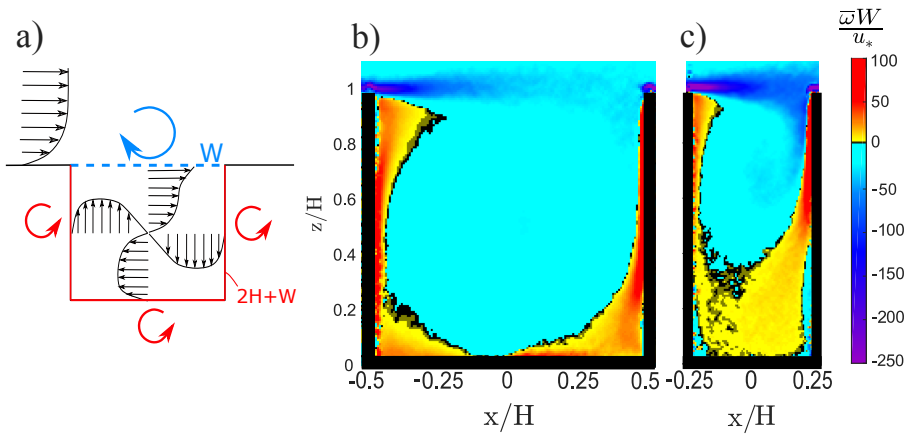

Figure 5.7: a) Qualitative representation of the mean velocity profile inside the cavity and of the vorticity boundary conditions. b-c) Mean vorticity field inside the cavity for aspect ratios $H/W = 1$ and $H/W = 2$.

After the analysis of the flow field within the cavity, we present below the results about the effect of the canyon geometry on pollutant dispersion. Fig. 5.8 shows the concentration field of the passive scalar released by the ground level source in stationary conditions. The non-dimensional concentration is expressed as

$\bar{c}u_*H/\dot{M}_q$, where $\bar{c}$ is the time averaged concentration of ethane in each point of the cavity (given in mg/m^3), and $\dot{M}_q$ is the mass flow injected at the linear source per unit of length (see Section 5.1.2). Fig. 5.8.a evidences the presence of fresh air at the downwind wall. As the aspect ratio of the cavity increases, higher concentrations of pollutants are measured at the pedestrian level compared to the mean concentration in the square cavity. For a cavity with $H/W = 2$ (Fig. 5.8.c), the concentration at street level is up to three times the concentration in the centre of the cavity. Thus, the formation of the second cell inhibits the transfer of pollutants from street level to the external flow, as already found in [Hussain and Lee, 1980], [Oke, 1988], and [Jeong and Andrews, 2002]. Moreover, we observe a different horizontal distribution of the mean concentration at street level in the two geometries. For H/W=1, pollutant concentration at the lower left corner is double compared to the right corner. Conversely, for H/W=2, 'air quality' is worse at the lower right corner with concentrations that are, also in this case, two times the concentrations measured at the other corner. This spatial distribution of the mean concentration for square and narrow cavities is in accordance with previous studies [Baik and Kim, 1999, Assimakopoulos et al., 2003, Liu et al., 2004]. In particular, the numerical simulations in [Assimakopoulos et al., 2003] and [Liu et al., 2004] showed similar values for the ratio of the concentrations measured in the two lower corners of the cavity.

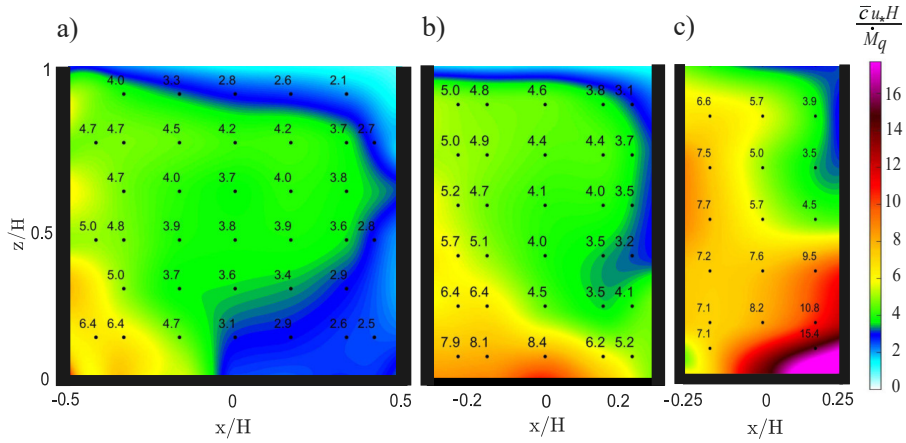

Figure 5.8: Mean concentration of the passive scalar inside the cavity for the aspect ratio (a) $H/W = 1$, (b) $H/W = 1.5$ and (c) $H/W = 2$.

A box model with two degrees of freedom for the cavity wash-out

The above presented results are confirmed by the analysis of the exchange processes inside the canyon for the different geometrical configurations.

The exchange between a street canyon, oriented perpendicular with respect to the wind, and the atmosphere aloft is traditionally described with box models with one degree of freedom [Hotchkiss, 1973, Johnson et al., 1973, Berkowicz, 2000, Soulhac, 2000, Kukkonen et al., 2001, Caton et al., 2003]. In these simple models, the canyon is described as a box with uniform pollutant concentration and a discontinuity surface at the top, where the exchange takes place.

The box model can be easily derived from the integration over the box volume of the advection-diffusion equation (Eq. 1.4). Following the same assumptions introduced in Section 1.2.1 and considering that u_{st} is here equal to zero, we obtain the mass balance for the box as:

$$V_{tot}\frac{dC}{dt} = Q + Su_d(C_{ext} - C), \tag{5.5}$$

where V_{tot} is the box volume, C is the mean concentration in the box, Q is a source term integrated over the entire volume, S is the exchange surface at the top of the box. The bulk exchange velocity u_d has been defined in Eq. 1.7 as the ratio between the vertical flux from the box (the cavity) towards the external flow and the concentration difference $(C - C_{ext})$.

To investigate ventilation dynamics in the cavity, we first analyse the wash-out curves from the unsteady experiments (see Section 5.1.2) measured at different positions for both a square (panel a) and a narrow (panel b) cavity (Fig. 5.9).

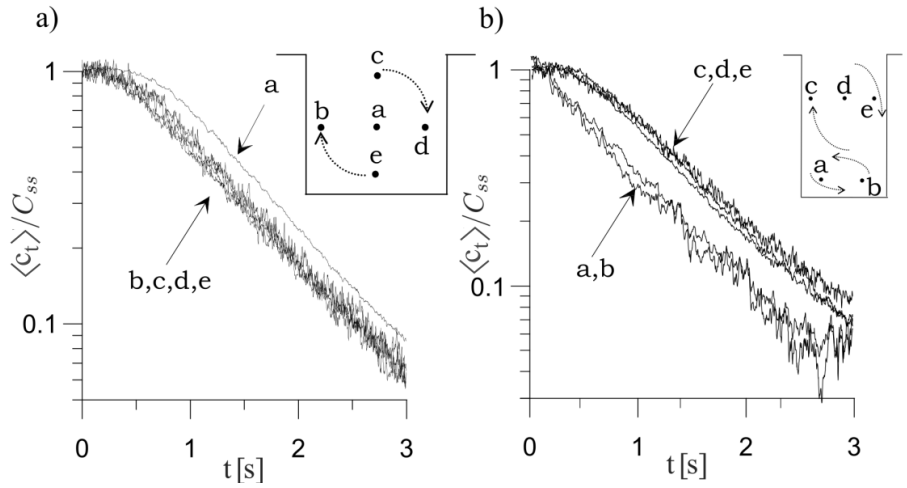

Figure 5.9: Dimensionless wash-out curves measured at different positions within a (a) square cavity with aspect ratio $H/W = 1$ and (b) a narrow cavity with aspect ratio $H/W = 2$.

For each sampling point (points a to e in the insets in Fig. 5.9), the wash-out curve is obtained as ensemble average ($\langle c_t \rangle$) of 30-50 experimental curves, and is

normalized by the mean concentration measured at that position in stationary conditions (C_{ss}). We observe that for both geometries all curves have an horizontal tangent for $t \to 0$. As discussed by [Salizzoni et al., 2009], this feature is not consistent with a one-degree of freedom model, based on the assumption of a perfect mixing within the canyon. In this sense the horizontal tangent indicates an initial mixing process acting on the non-uniform concentrations within the canyon. Moreover, the curves follow two characteristic trends depending on the position of the sampling point. In the square cavity (panel a), the time delay before the concentration decay is longer for the curve registered at the centre of the cavity (point *a*) with respect to those measured in the recirculating part of the flow (points *b*-*e*). The trend of these latter curves is very similar, instead. In the narrow cavity (panel b), the concentration in the upper part of the cavity (points *c*-*e*) decays later than in the bottom part of the cavity (points *a*-*b*). Notice that the non-stationary concentration in points *c*-*e* appears higher with respect to points *a*-*b* due to the normalization by the stationary concentration.

The wash-out curves are not identical in all the regions of the flow. Moreover, the mean concentration is far from being uniform within the canyon (Fig. 5.8). These two features evidence how the rate of pollutant transfer is not uniform inside the cavity and that more than one time scale is involved in the wash-out process. Since these experimental data cannot be interpreted with a box model with a single degree of freedom, we adopt the analytical model with two degrees of freedom proposed by [Salizzoni, 2006], [Salizzoni et al., 2009], and [Murena et al., 2011] for a square cavity. The model is here extended also to the case of a narrow cavity.

We consider the flow in the cavity as made up by two regions. The cavity wash-out is then described by means of a sequence of pollutant transfers between three regions, with different mean concentration within them. One region represents the external flow, the two other boxes give a rough description of the pollutant distribution inside the canyon.

In a square cavity the first box (box_1) represents the recirculating part of the flow which leads pollutant in touch with the shear layer at the top of the cavity, while the second box (box_2) represents the core of the flow inside the cavity (Fig. 5.10.a). The distinction between these regions is consistent with the different behaviour observed in Fig. 5.9.a for the the wash-out curve in point *a* with respect to the trend in points *b*-*e*. In a narrow cavity with two recirculating cells, the first box (box_1) represents the cell at the top of the cavity exchanging pollutants with the external flow, whereas the second box (box_2) represents the cell at the bottom of the cavity (Fig. 5.10.b), in accordance with the two trends observed in Fig. 5.9.b for the concentration measured in points *c*-*e* and *a*-*b*, respectively.

To model the temporal evolution of a passive scalar concentration within the cavity as it empties (after having stopped the injection from the source at street level), we can adopt Eq. 5.5 and write the mass balance for the two boxes within the cavity as:

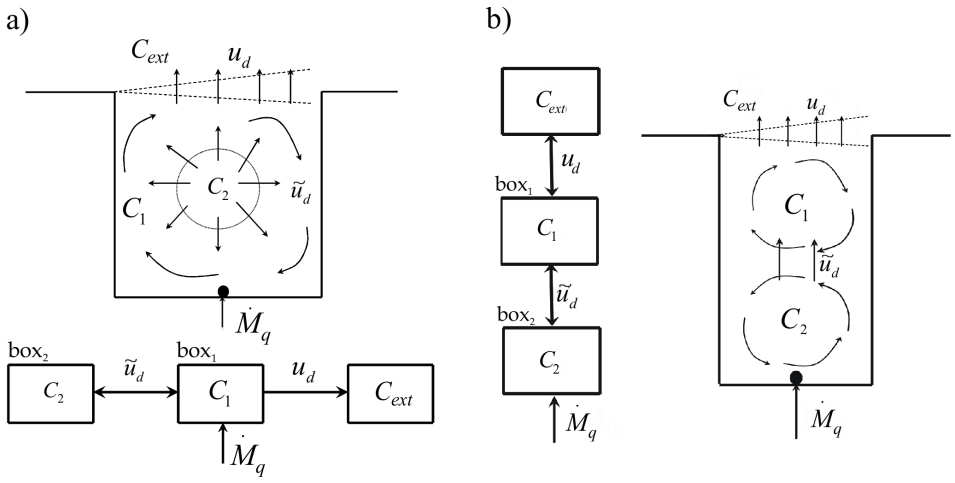

Figure 5.10: Simplified model of pollutant transfer from a ground level source within a square (a) and a narrow (b) cavity.

$$\begin{cases} V_1 \dfrac{dC_1}{dt} = & S_{10} u_d (C_{ext} - C_1) + S_{12} \tilde{u}_d (C_2 - C_1) \\ V_2 \dfrac{dC_2}{dt} = & S_{12} \tilde{u}_d (C_1 - C_2) \\ C_1(0) = & C_{1ss} \\ C_2(0) = & C_{2ss}. \end{cases} \tag{5.6}$$

where S_{10} is the exchange surface between box$_1$ and the external flow and S_{12} is the exchange surface between box$_1$ and box$_2$; V_1 and V_2, C_1 and C_2 are the volume and the mean concentration of box$_1$ and box$_2$, respectively. u_d and $\tilde{u}_d$ are the bulk exchange velocities between box$_1$ and the external flow, and between box$_1$ and box$_2$, respectively. C_{1ss} and C_{2ss} are the initial concentrations in the two boxes. These concentrations are those measured in stationary conditions, with a constant mass rate emitted from the source.

We set the volume of each box as a function of the total volume (per unit width) of the cavity ($V_{tot} = WH$) by means of a geometrical parameter β:

$$V_1 = \beta V_{tot}, \qquad V_2 = (1 - \beta) V_{tot}. \tag{5.7}$$

Evidently, S_{10} and S_{12} are equal to W in a narrow cavity. On the other hand, the exchange surface S_{12} in a square cavity depends on the extent of V_2 and thus on β. From geometrical considerations, it is easy to find the expression of S_{12} as a function of V_{tot} and β: $S_{12} = 2\sqrt{(1-\beta)\pi V_{tot}}$.

We then define a characteristic wash-out time for each box as

$$T_1 = \frac{\beta V_{tot}}{S_{10} u_d}, \qquad T_2 = \frac{(1-\beta) V_{tot}}{S_{12} \tilde{u}_d}, \tag{5.8}$$

that is the time for pollutants to exit box_1 and box_2, respectively.

Substituting (5.8) in (5.6), and approximating the external concentration C_{ext} to zero, we obtain:

$$\begin{cases} \frac{dC_1}{dt} = & -\frac{C_1}{T_1} + \frac{(1-\beta)}{\beta T_2}(C_2 - C_1) \\ \frac{dC_2}{dt} = & \frac{1}{T_2}(C_1 - C_2) \\ C_1(0) = & C_{1ss} \\ C_2(0) = & C_{2ss}. \end{cases} \tag{5.9}$$

This can be rewritten as:

$$\begin{cases} \frac{dC_1}{dt} = & AC_1 + \frac{D}{\beta}(C_2 - C_1) \\ \frac{dC_2}{dt} = & \frac{D}{(1-\beta)}(C_1 - C_2) \\ C_1(0) = & C_{1ss} \\ C_2(0) = & C_{2ss}, \end{cases} \tag{5.10}$$

where

$$A = -\frac{1}{T1}, \quad D = \frac{1}{T_2}(1-\beta). \tag{5.11}$$

Equation 5.10 is a system of linear first order differential equations that admits the general solution:

$$\mathbf{C} = a_1\mathbf{k_1}e^{r_1 t} + a_2\mathbf{k_2}e^{r_2 t}, \tag{5.12}$$

where a_1 and a_2 are two constants, while r_1 and r_2, $\mathbf{k_1}$ and $\mathbf{k_2}$ are respectively the eigenvalues and eigenvectors of the coefficient matrix of the linear system.

Once the eigenvalues and eigenvectors of the system are found, the solution displayed in Equation 5.12 is obtained in terms of $C_1(t, u_d, \tilde{u}_d, \beta, C_{1ss}, a_1, a_2)$ and $C_2(t, u_d, \tilde{u}_d, \beta, C_{2ss}, a_1, a_2)$. This solution can be rewritten in the two normalized functions $C_1'(t) = C_1/C_{1ss}$ and $C_2' = C_2(t)/C_{2ss}$. Then, applying the initial conditions ($C_1'(0) = 1$ and $C_2'(0) = 1$), the constants a_1 and a_2 are found. The final solution of the system reads:

$$\begin{cases} C_1'(t) = & \frac{\Gamma+2D\gamma-D-A\beta^2+A\beta+2D\beta-2D\beta\gamma}{2\Gamma}\exp\{t[\frac{D-\Gamma+A\beta^2-A\beta}{2\beta^2-2\beta}]\}- \\ & -\frac{-\Gamma+2D\gamma-D-A\beta^2+A\beta+2D\beta-2D\beta\gamma}{2\Gamma}\exp\{t[\frac{D+\Gamma+A\beta^2-A\beta}{2\beta^2-2\beta}]\} \\ C_2'(t) = & \frac{\Gamma+2D\gamma-D-A\beta^2+A\beta+2D\beta-2D\beta\gamma}{2\Gamma\gamma}\frac{A\beta^2-A\beta-2D\beta+D+\Gamma}{2D(1-\beta)}\cdot \\ & \cdot\exp\{t[\frac{D-\Gamma+A\beta^2-A\beta}{2\beta^2-2\beta}]\}+ \\ & +\frac{-\Gamma+2D\gamma-D-A\beta^2+A\beta+2D\beta-2D\beta\gamma}{2\Gamma\gamma}\frac{-A\beta^2+A\beta+2D\beta-D+\Gamma}{2D(1-\beta)}\cdot \\ & \cdot\exp\{t[\frac{D+\Gamma+A\beta^2-A\beta}{2\beta^2-2\beta}]\} \end{cases} \tag{5.13}$$

where Γ is

$$\Gamma = \sqrt{A^2\beta^4 - 2A^2\beta^3 + A^2\beta^2 - 4AD\beta^3 + 6AD\beta^2 - 2AD\beta + D^2}, \tag{5.14}$$

and $\gamma = \dfrac{C_{2ss}}{C_{1ss}}$.

The solution is valid for both square and narrow cavities and gives an analytical description of the temporal evolution of the mean concentration in box_1 and box_2 as a function of two free parameters, u_d and $\tilde{u}_d$. The velocity u_d is the bulk exchange velocity between box_1 and the external flow, while $\tilde{u}_d$ is the bulk exchange velocity between box_1 and box_2. The least squared method is applied to find the values of u_d and $\tilde{u}_d$ that minimize the difference between the experimental data and the analytical curves. To this aim, the parameters γ and β have to be first defined. γ is the ratio between the mean concentration in box_2 and box_1. β describes the extent of the two boxes.

Starting from the solution in stationary conditions of the analytical model shown in Equation 5.9, γ can be estimated equal to one for a square cavity, as demonstrated in [Salizzoni et al., 2009]. The evaluation of the geometrical parameter β appears quite difficult, instead. As proposed by [Salizzoni et al., 2009], β varies in the range [0.8, 0.9]. For a narrow cavity, γ is different from one, as the mean concentration in stationary conditions in the lower part of the cavity is higher than in the upper part of the cavity, as evidenced in Fig. 5.11.a. This difference in the spatial distribution of the concentration is useful to delimit the volume of the two boxes. Fig. 5.11 shows the trend of γ as a function of β for a narrow cavity with $H/W = 2$. For β around 0.7, γ reaches its maximum, i.e. the difference between the mean concentration in the two boxes is the highest and thus the two regions are well delimited. Following these considerations, the parameters β and γ for a narrow cavity are estimated.

In Fig. 5.12, the analytical wash-out curves are compared with the experimental data for a square (panel a) and a narrow cavity (panel b). To this aim, we consider

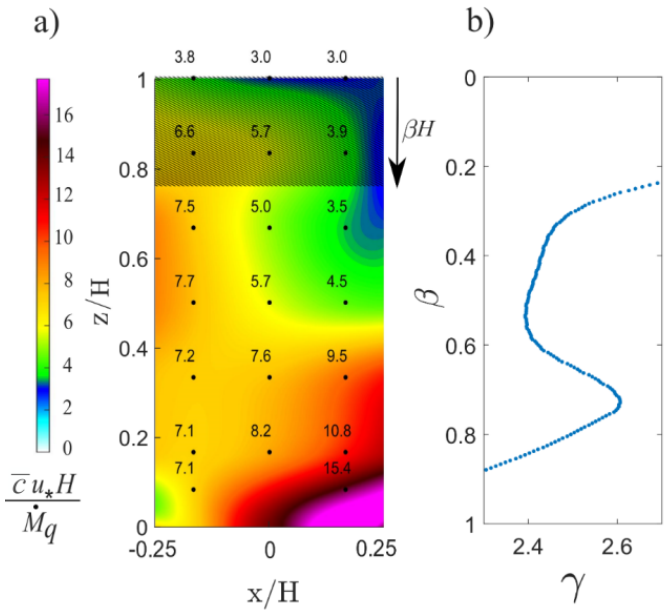

Figure 5.11: a) Mean concentration in a narrow cavity ($H/W = 2$) with a constant mass rate injected by a street level source. b) γ as a function of β for the delimitation of the two regions inside the cavity.

the experimental wash-out curve measured in a specific point as representative of the entire box volume. The good agreement between data and model demonstrates that the simplified two-box model gives a satisfactory description of the cavity wash-out. For both geometries, the estimated velocities u_d and $\tilde{u}_d$ are reported. These results show that, for a narrow cavity, u_d is more than twice $\tilde{u}_d$. The effective transport of pollutant particles from the bottom cell to the upper cell within the cavity is slow, while the wash-out towards the external atmosphere is rapid. Since pollutant release takes place at the pedestrian level, this slower transfer acts as a bottleneck for the entire ventilation process and a higher concentration develops at street level (Fig. 5.8.c). Conversely, in a square cavity, pollutants emitted at street level are directly transferred outside with velocity u_d. In this case, the low $\tilde{u}_d$ value reduces the transfer rate in the centre of the cavity with no significant effects on the street level dynamics.

Since the transition from one to two recirculating cells is crucial for the spatial distribution and the concentration of pollutants inside the cavity, in the following sections we will discuss the effect of wall roughness and heating on this transition.

5.2.2 Effect of the small geometrical scale

Experiments with two different roughness scales ($h_r = 2$ mm and $h_r = 5$ mm) at the lateral walls of the canyon were performed. Only the results obtained for

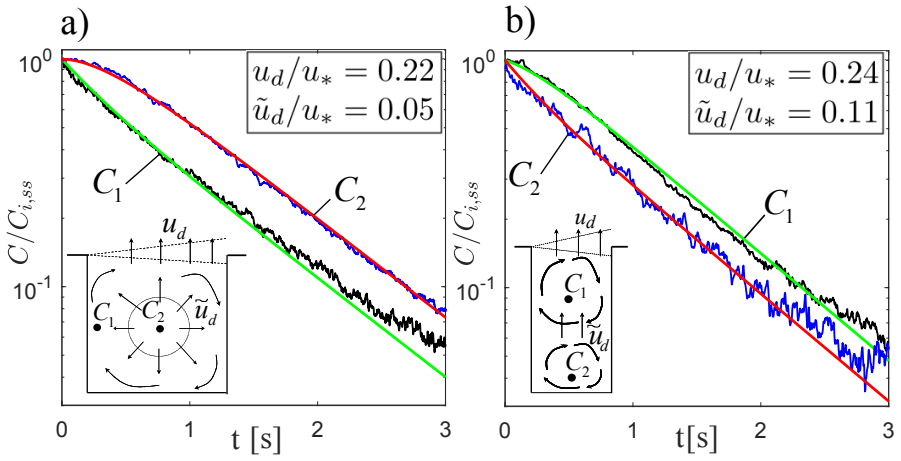

Figure 5.12: a) Experimental (black and blue lines) and analytical (green and red lines) wash-out curves in the recirculating region and in the centre of a square cavity. b) Experimental (black and blue lines) and analytical (green and red lines) wash-out curves at the top and the bottom of a narrow cavity. For both aspect ratios, the wash-out velocities (u_d and $\tilde{u}_d$) are reported.

roughness elements 5 mm high are shown and discussed here. A similar, but less pronounced, behaviour was observed with small roughness elements.

Figures 5.4 and 5.5 evidenced that, for a cavity with smooth walls, the aspect ratio $H/W = 3/2$ is close to the critical ratio for transition. For this geometry, the occurrence of roughness elements (with $h_r = 5$ mm) on the upwind wall of the cavity has slight effects on the mean velocity field (see Fig. 5.13.a compared to Fig. 5.4.b). Conversely, adding roughness to the downwind wall facilitates the formation of the second counter-rotating cell. In fact, the streamlines in Fig. 5.13.b reveal an incipient separation between the regimes of motion in the upper and lower part of the cavity. This behaviour is confirmed for different aspect ratios by the analysis of the vertical profile of the mean horizontal velocity in $x = 0$ (Fig. 5.13.c). With roughness elements on the upwind wall (dashed lines), the vertical profile slightly differs from the profile that is established in the cavity with smooth walls (dotted lines). With roughness on the downwind wall (continuous line) the vertical profile tends to the characteristic profile of a motion with two counter-rotating cells, as those observed in Fig. 5.5 for aspect ratios greater than 1.8.

As for the large geometrical scale, the effect of wall roughness can be interpreted in terms of vorticity. Wall roughness increases the mean velocity gradients near the walls. As a consequence, the vorticity flux from the wall towards the cavity (Fig. 5.7.a) is enhanced. However, for a rough upwind wall, the additional anticlockwise vorticity is more rapidly transferred outside the cavity, so that it does not significantly modify the vorticity balance in the domain. This is evidenced by panels d and e in Fig. 5.13 showing the vorticity field in a cavity with aspect ratio 3/2

with smooth walls and with roughness elements on the upwind wall, respectively. On the other hand, the additional anticlockwise vorticity generated at the rough downwind wall is advected along the streamlines of the mean velocity field in the core of the cavity, where it induces the formation of the counter-rotating cell. The increase in anticlockwise vorticity at the bottom of the cavity can be observed in the case of roughness elements on the downwind wall in Fig. 5.13.f.

The formation of secondary vortices in the street canyon due to the presence of roughness elements on building walls is confirmed by the numerical studies of [Murena and Mele, 2016] and [Llaguno-Munitxa et al., 2017], where a reduced turbulence intensity and a slower wash-out of the cavity were observed. However, these numerical studies did not analyse the effect of roughness on one wall at a time.

5.3 Effect of wall heating

5.3.1 Effect of upwind wall heating

The upwind wall of the cavity is heated and three temperature differences (ΔT) are experimented and discussed: 0 K, 140 K, and 240 K (Froude numbers are reported in Table 5.2). The effect of wall heating is investigated for a square cavity ($H/W = 1$) and for a narrow cavity with an aspect ratio $H/W = 3/2$. As observed in the previous sections, in this latter geometrical configuration the flow field is close to the transition from one to two recirculating cells.

Regardless the wall temperature, the mean velocity profiles (panels a and b in Fig. 5.14) evidence the presence of a shear layer at the cavity top, where the vertical profile of the horizontal component (black lines) reaches its maximum. The level of TKE (panels c and d in Fig. 5.14) is higher at the cavity top and along the downwind wall, where a TKE plume spreads down in the cavity from the external flow.

We observe negligible variations in the mean and fluctuating velocity fields, when the upwind wall is heated. This is found for both a square (panels a and c in Fig. 5.14) and a narrow (panels b and d Fig. 5.14) cavity. As will be discussed in Section 5.3.3, the heated air at the upwind wall is rapidly transferred outside the cavity, with very low effect on the recirculating flow field.

Other authors [Allegrini et al., 2013, Marucci and Carpentieri, 2019] found a slight increase of the mean motion and of the TKE inside a square cavity due to buoyancy effects at the upwind wall. This is likely to be due to the lower internal Froude number considered in their experiments, that, as mentioned in Section 5.1.3, is one order of magnitude lower than the Fr_i values experimented here. We remind that the Froude number is here limited by the scale of the experiment. The low height of the cavity H implies a high external velocity to satisfy Reynolds independence. These experimental conditions (low H and high u_*) lead to relatively

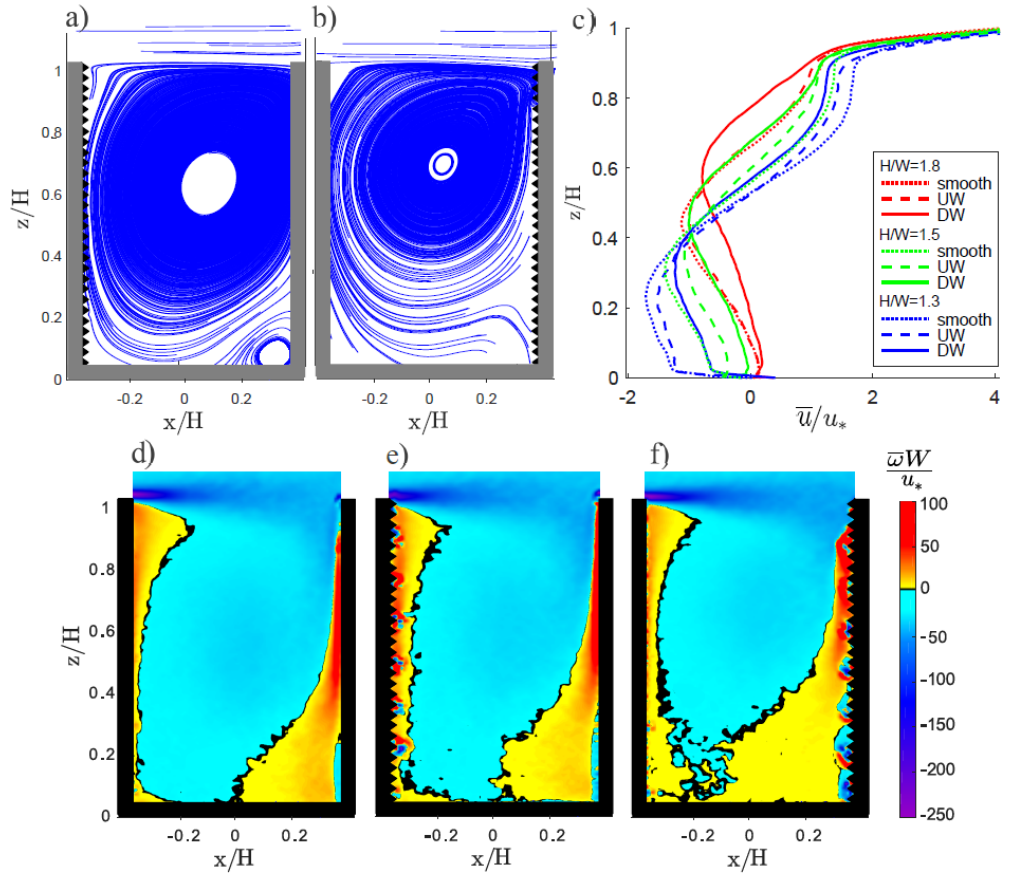

Figure 5.13: Effect on the mean velocity field of wall roughness at the (a) upwind (UW) and (b) downwind (DW) wall for a cavity with $H/W = 3/2$. (c) Vertical profile of the mean horizontal velocity in $x = 0$ for different aspect ratios and for different conditions of the walls: smooth walls (dotted lines), UW roughness (dashed lines) and DW roughness (continuous lines). Normalized vorticity field within a cavity with H/W=3/2 and with (d) smooth walls, (e) UW wall roughness, (f) DW wall roughness.

high Fr_i with respect to the above mentioned experiments.

5.3.2 Effect of downwind wall heating

The downwind wall of the cavity is heated and four temperature differences (ΔT) are considered: 0 K, 70 K, 170 K and 240 K (Froude numbers are reported in Table 5.2). When the downwind wall is heated, we observe diverse effects depending on the aspect ratio of the cavity.

For square cavities ($H/W = 1$), in the range of Fr_i considered in this study,

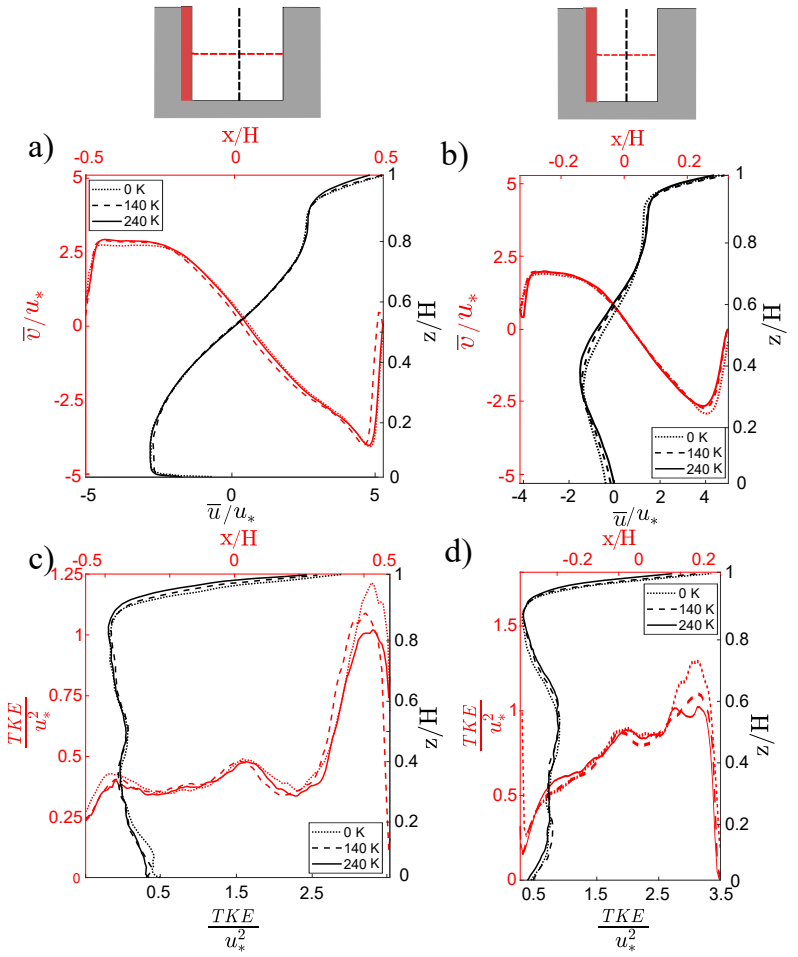

Figure 5.14: Upwind wall heating. Horizontal (red lines) and vertical (black lines) profiles of the vertical ($\overline{v}$) and horizontal ($\overline{u}$) components of the mean velocity (panels a and b) and of the TKE (panels c and d) within the cavity for the aspect ratios $H/W = 1$ (left panels) and 1.5 (right panels). We remind that we follow here the notation proposed in the introduction of this thesis (Fig. 4), i.e. we use u, v to denote the components of the velocity vector along x and z.

the heating of the downwind wall has negligible effects on the mean velocity field. Fig. 5.15.a shows the vertical profile of the mean horizontal velocity ($\overline{u}$) and the horizontal profile of the vertical velocity component ($\overline{v}$). The profiles at different temperature configurations tend to overlap. The heating of the downwind wall has evident effects on the fluctuating field, instead. An increment of around 400% and 200% is observed for the horizontal (Fig. 5.15.b) and vertical (Fig. 5.15.c) profiles of the TKE when ΔT increases from 0 to 240 K. These variations are significantly higher than the error associated with the estimate of the TKE by means of PIV (see Section 5.1.2). Even for the TKE variations measured for ΔT =70 K and 170

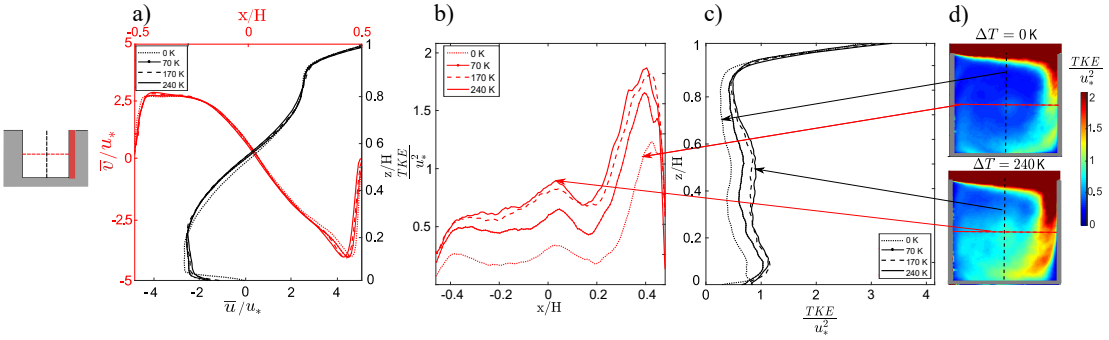

Figure 5.15: Downwind wall heating for a square cavity ($H/W = 1$). Horizontal (red lines) and vertical (black lines) profiles of the vertical ($\overline{v}$) and horizontal ($\overline{u}$) components of the mean velocity (a) and of the TKE inside the cavity (b and c). In d, the TKE field for the maximum heating configuration is compared to the configuration with no heated walls.

K, the measurement error is negligible. While the variation from ΔT =170 K to 240 K is subject to the greatest degree of uncertainty. For a square cavity, this increase in the turbulent fluctuations near the heated downwind wall is confirmed by [Allegrini et al., 2013] and [Marucci and Carpentieri, 2019]. However, with respect to our findings, they also observed a different mean flow structure with the formation of a secondary rotating vortex, probably due to the lower values of Fr_i imposed in their experiments.

To better investigate this discrepancy in results, we go beyond the observation of the velocity profiles of Fig. 5.15.a and we show in Fig. 5.16 the mean vertical velocity field within the whole cavity for $\Delta T = 0$ K (a), 70 K (b), 170 K (c), and 240 K (d). Significant variations between the different heating configurations are not detectable. To better catch any changes, in Fig. 5.17, we show the difference between the mean vertical velocity field at $\Delta T = 240$ K and at $\Delta T = 0$ K (i.e. the difference between the flow fields in panels d and a of Fig. 5.16). Near the cavity walls noticeable variations are observable. However, in these regions, velocity gradients are maximum. These variations are therefore due to a slight shift in the position of the main vortex rather than to structural changes in the mean flow field.

Concerning the dynamics of the passive scalar, the mean concentration of pollutants inside the cavity decreases with increasing ΔT when $H/W = 1$ (Fig. 5.18). This suggests a more efficient canyon ventilation. To further explore this behaviour, as customary, we turn to the analysis of the wash-out curves provided by the unsteady experiments. In Fig. 5.19, the concentration in both the lateral (panel a) and central (panel b) part of the cavity decays more rapidly as the thermal flux at the downwind wall is increased. The wash-out velocities (Table 5.3), estimated by the application of the model with two degrees of freedom, reveal that the heating

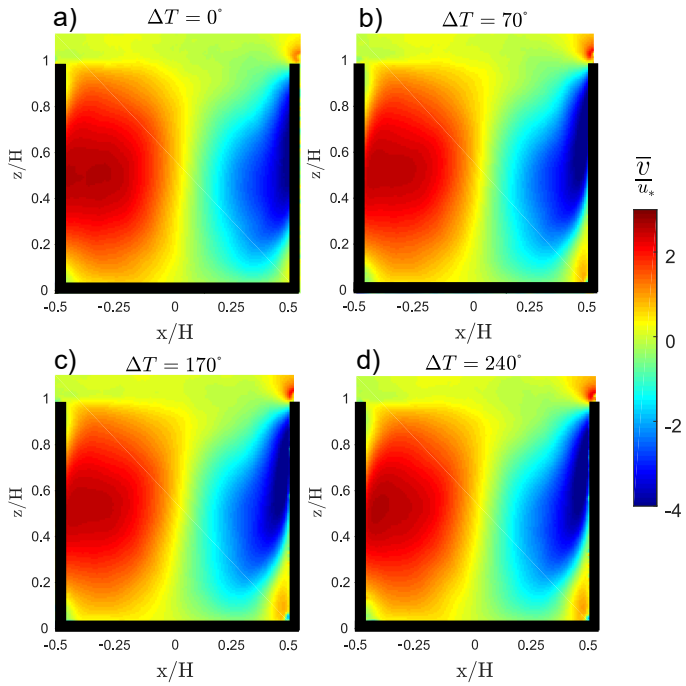

Figure 5.16: Mean field of the normalized vertical velocity for different heating conditions at the downwind wall of a square cavity.

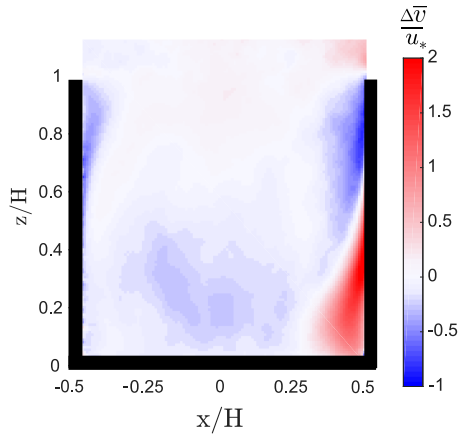

Figure 5.17: Variation in the mean field of the normalized vertical velocity, passing from $\Delta T = 0$ K, $\Delta T = 240$ K in a square cavity.

of the downwind wall enhances the wash-out velocities, $\tilde{u}_d$ and u_d. Notice that the results for $\Delta T = 240$ K are here not reported as the experiments in unsteady conditions for this configuration were not performed.

Thus, for a square cavity, the heating of the downwind wall increases the levels of TKE within the cavity and enhances the canyon ventilation, while the mean

motion is almost unaltered. Moreover, the values of the estimated wash-out velocities (u_d and $\tilde{u}_d$) are very low compared to the characteristic velocity scale for the mean advection in the cavity. These findings are in accordance with previous works [Salizzoni et al., 2009] suggesting that the cavity wash-out, in a perpendicular street canyon, is mainly regulated by the fluctuating component of the velocity field. These considerations will be discussed in detail in Section 5.4.

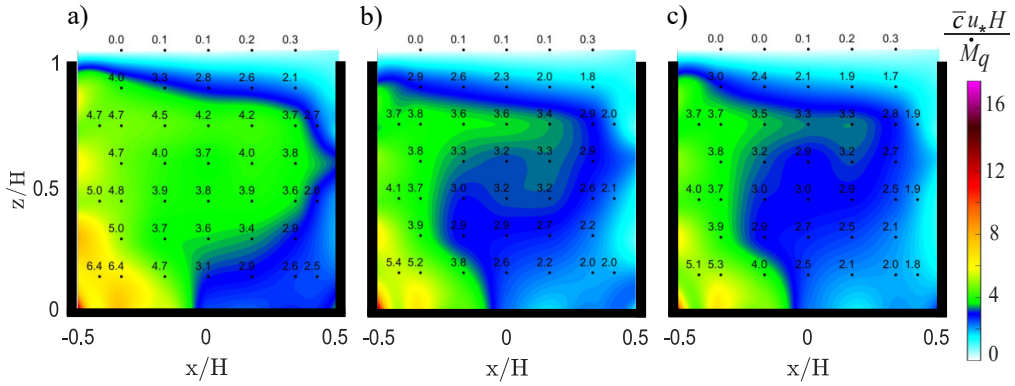

Figure 5.18: Concentration of a passive scalar released at street level in a square cavity for different heating of the downwind wall: (a) $\Delta T = 0$ K, (b) $\Delta T = 70$ K, and (c) $\Delta T = 170$ K.

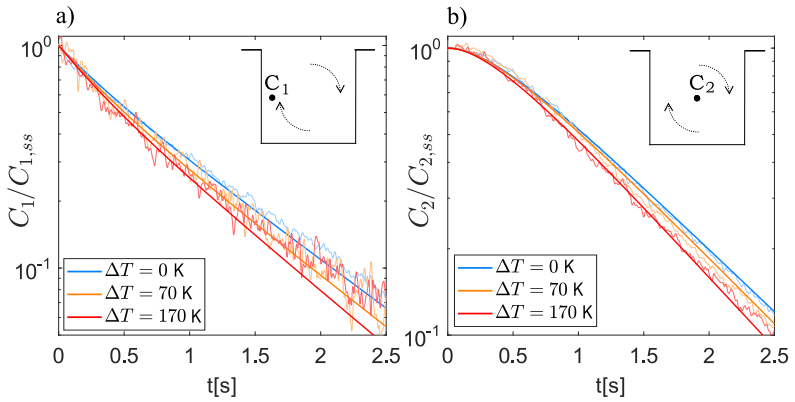

Figure 5.19: Dimensionless wash-out curves measured in the (a) lateral and (b) central part of a square cavity for different heating of the downwind wall. The analytical wash-out curves are above the experimental data (shaded lines).

In narrow cavities ($H/W = 1.5$), the heating of the downwind wall has remarkable effects on both the mean motion (panels a to c in Fig. 5.20) and the TKE inside the cavity (panels d to g in Fig. 5.20). The thermal gradient near the downwind wall facilitates the transition from one cell to two counter-rotating cells

Table 5.3: Variation of the wash-out velocities (u_d and $\tilde{u}_d$) as a function of the temperature difference ΔT in a square cavity.

	$\Delta T = 0$ K	$\Delta T = 70$ K	$\Delta T = 170$ K
	$Fr_i = \infty$	$Fr_i = 0.62$	$Fr_i = 0.40$
u_d/u_* [-]	0.22	0.33	0.35
$\tilde{u}_d/u_*$ [-]	0.050	0.066	0.069

(panel c). This behaviour is evidenced by the vertical profile of the mean horizontal velocity in $x = 0$ (panel b) that tends to the characteristic profile of a motion with two counter-rotating cells as ΔT increases and Fr_i decreases (see the cases of $H/W \geq 1.8$ in Fig. 5.5). As seen in Fig. 5.6, this transition inhibits the penetration of the TKE plume from the external flow into the cavity. Thus, the highest values of TKE at street level are reached for the no-heated configuration (dotted line in Fig. 5.20.e): as the temperature of the wall increases, the level of TKE enhances in the upper part of the canyon (panel d) while a low turbulence region develops at street level (panel e). As pointed out for the square cavity, the uncertainty in TKE measurements by means of PIV does not compromise the reliability of the observed trends.

The concentration of pollutants (Fig. 5.21) increases with ΔT at the street level, while the exchange at roof level does not seem to be compromised by the heat fluxes.

As shown for the square cavity (see Fig. 5.19 and Table 5.3), the analysis of the wash-out process provides further insights into the transport mechanisms. However, for the cavity with $H/W = 1.5$ the analytical model for the wash-out process must be applied more carefully. For $\Delta T = 0$ K, the model is applied as for the case of a square cavity, because a single vortex establishes in the cavity (see panel c in Fig. 5.20). For $\Delta T = 170$ K, two distinct vortices can be identified and thus the model with two boxes connected in series has to be used. In the transition ($\Delta T = 70$ K) neither of the two models is applicable since we cannot clearly identify the spatial extent of the two cells. Despite limitations in the application, the analysis of the wash-out curves reveals that u_d (i.e., the exchange velocity for the rotating cell in contact with the external flow) is enhanced by the heating of the wall (blue markers 4, 6 in Fig. 5.24). On the other hand, results about $\tilde{u}_d$ are not comparable between the configurations because they are representative of different transport regions: for $\Delta T = 0$ K, $\tilde{u}_d$ is the exchange velocity between two concentric cells, while for $\Delta T = 170$ K, $\tilde{u}_d$ is the exchange velocity between the bottom cell at the pedestrian level and the upper cell. However, the concentration fields reported in Fig. 5.21 suggest that the vertical exchange in the lower part of the cavity tends to decrease as the wall is heated.

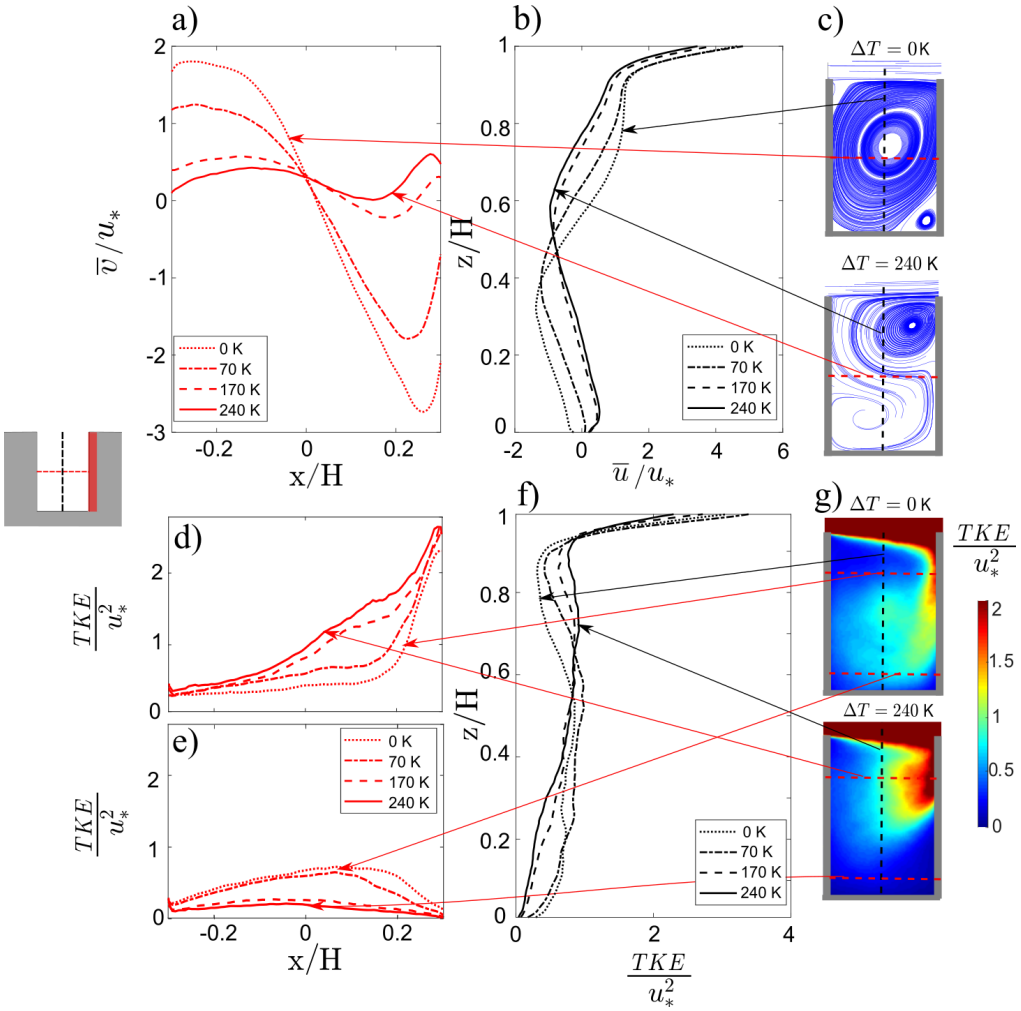

Figure 5.20: Downwind wall heating for a narrow cavity ($H/W = 1.5$). Horizontal (red lines) and vertical (black lines) profiles of the vertical ($\overline{v}$) and horizontal ($\overline{u}$) components of the mean velocity (a and b) and of the TKE (d to e) inside the cavity. In panels c and g, the mean velocity field and the TKE field for the configuration with $\Delta T = 240$ K is compared to the configuration with $\Delta T = 0$ K.

Differently from the square cavity, the role of TKE on canyon ventilation, compared to the role of the mean flow, can hardly be distinguished in a narrow cavity. Here, the topology of the mean flow has an evident effect on the distribution of the TKE and thus on canyon ventilation. However, the role of TKE in the pollutant transfer (found above for a square cavity) is in accordance with the results obtained here for a narrow cavity. The enhancement of the turbulent fluctuations in the upper part of the cavity (Fig. 5.20.d) accelerates the wash-out of pollutants at roof level, while the decreasing TKE levels in the bottom part of the cavity

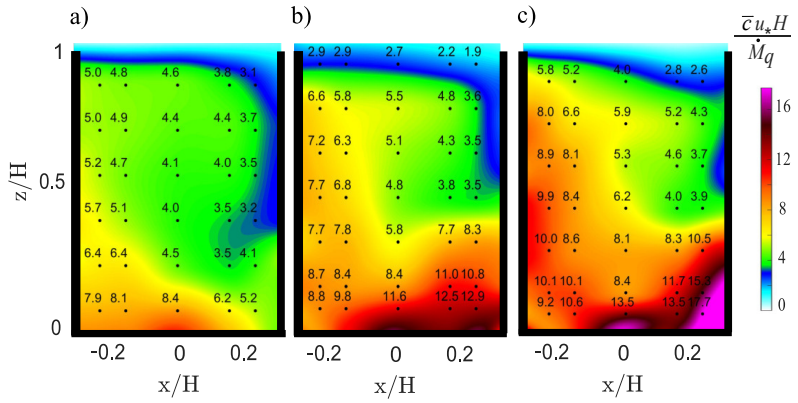

Figure 5.21: Concentration of a passive scalar released at street level in a narrow cavity for different heating of the downwind wall: a) $\Delta T = 0$ K, b) $\Delta T = 70$ K, and c) $\Delta T = 170$ K

(Fig. 5.20.e) inhibits the vertical transfer of pollutants from street level. Since the pollutant source is placed at street level, the slowing down of the transfer in the lower part of the cavity acts as a bottleneck for the entire ventilation process and thus, in steady conditions, the concentration of pollutants at street level increases with the temperature of the downwind wall (Fig. 5.21.c).

Criticisms to this interpretation can arise from the observation of the drastic variation in the mean velocity field with increasing heating of the downwind wall (panels a to c in Fig. 5.20). The turbulent kinetic energy in the core of the cavity varies as well, but it is almost constant at the top of the cavity (at $z/H = 1$), where the vertical transfer between the canyon and the external flow takes place. Here, the transfer velocity increases with ΔT (see u_d for cases 4, 5 and 6 in Fig. 5.24). In the first instance, these results suggest that the mean velocity field within the cavity, rather than the turbulent kinetic energy, has a role in canyon ventilation. For a better understanding of this mechanism, we analyse the mean vertical velocity ($\overline{v}$) at $z/H = 1$ (Fig. 5.22.a). The horizontal profile of $\overline{v}$ does not show significant variations with ΔT. As ΔT increases, the peak of the positive vertical velocity slightly shifts from the upwind wall towards the centre of the cavity, in accordance with the variation in the structure of the mean flow observed in Fig. 5.20.c-d. However, the average incoming and outgoing flow from the cavity is comparable for the different heating configurations. Thus, at $z/H = 1$ there are no significant variations in the mean flow with ΔT, and in the upper part of the cavity (Fig. 5.20.a) there is even a weakening of the mean flow. These results do not motivate the increase in the vertical exchange velocity u_d observed in Fig. 5.24.

As for the mean velocity, also the fluctuating component of the vertical flow (Fig. 5.22.b) does not show significant variations with ΔT at z/H=1, unlike the clear increase in the fluctuating component of the turbulent flow (TKE) observed

in the upper part of the cavity (Figures 5.20.d-g).

These results suggest that the mean velocity is not a driver for canyon ventilation (in the case of a wind direction perpendicular to the street) and that the transport of pollutants is not governed by the TKE at z/H=1, which is almost constant with ΔT but exhibits the highest values (with respect to all cavity) in each configuration. The global vertical exchange rather depends on the TKE within the entire cavity, and, in particular, it is strongly slowed down by the low TKE areas acting as bottlenecks.

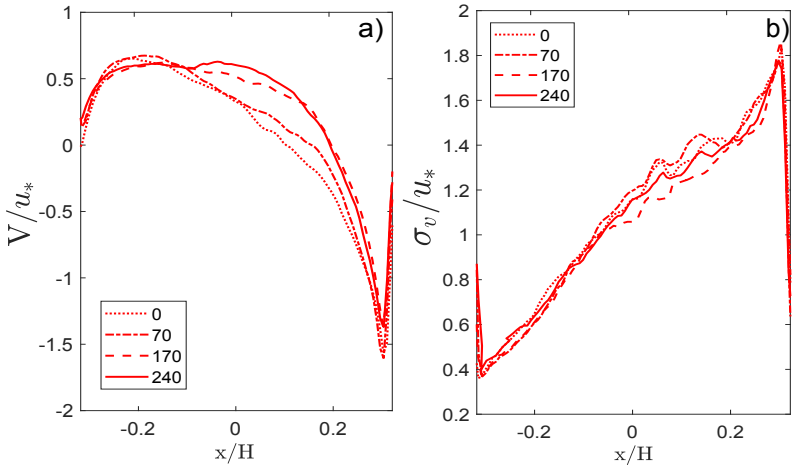

Figure 5.22: a) Horizontal profile of the normalized mean vertical velocity $\overline{v}$ at the cavity top (z/H=1). b) Horizontal profile of the normalized standard deviation of the vertical velocity σ_V at the cavity top (z/H=1).

5.3.3 Vorticity dynamics in a heated cavity

As for the role of aspect ratio and wall roughness (Section 5.2), the analysis of the vorticity dynamics within the cavity helps in clarifying the different flow behaviours observed for the heating of the upwind and downwind wall (Sections 5.3.1-5.3.2).

In the vorticity transport equation (Equation 5.4), the last term accounts for vorticity production due to thermal gradients. When the upwind wall is heated, the vector product between the opposite of the thermal gradient S_T and the gravity vector generates clockwise vorticity near the wall (Fig. 5.23.b). This additional vorticity is in accordance with the main vorticity field inside the cavity and, due to geometrical reasons, it is rapidly transferred outside the cavity with negligible effects on the mean and fluctuating velocity components. Indeed, the vorticity near the upwind heated wall in a square cavity (Fig. 5.23.a) exhibits a vertical profile with negligible variations for different buoyancy conditions.

Conversely, when the downwind wall is heated, the thermal gradient generates anticlockwise vorticity near the wall (Fig. 5.23.b). Fig. 5.23.c evidences a trend toward positive and thus anticlockwise vorticity near the downwind heated wall of a square cavity. Similarly to the case of a rough downwind wall (Section 5.2.2), the additional anticlockwise vorticity generated at the wall is advected in the core of the flow field. For a square cavity, this additional anticlockwise vorticity seems to only affect the fluctuating velocity field (Fig. 5.15.b-d), while, in a narrow cavity, it triggers the formation of the second cell (Fig. 5.20.a-c).

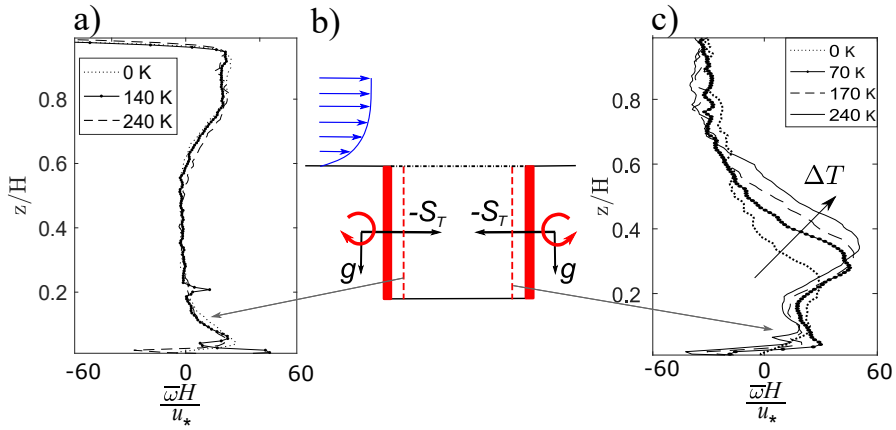

Figure 5.23: Schematic representation of the vorticity generation near the heated walls (b). Vertical profile of the vorticity near the upwind (a) and downwind (b) walls for a square cavity in the case of upwind wall heating and downwind wall heating, respectively.

5.4 Turbulent kinetic energy and canyon ventilation

The experimental results reported in Section 5.3.2 suggest a correlation between the increase in turbulent kinetic energy and the velocity of the wash-out process in an idealised 2D street canyon perpendicular to the wind direction. In the square cavity, TKE levels enhance within the entire cavity due to the heating of the downwind wall. At the same time, an acceleration is observed in the pollutant exchange between the cavity and the external atmosphere (u_d), and between the core and the outer part of the recirculating cell within the cavity ($\tilde{u}_d$). In the narrow cavity instead, thermal fluxes at the downwind wall induce the formation of two counter-rotating cells, and thus the TKE increases at the top of the cavity but decreases at street level. The results for the concentration field suggest that the vertical

exchange in the upper part of the cavity (u_d) is accelerated, while the exchange between the two internal cells ($\tilde{u}_d$) is inhibited.

Our interpretation for this higher efficiency of the turbulent transport in the ventilation of the perpendicular canyon is that this mechanism is responsible for the transfer of pollutant particles across the streamlines of the flow, in a dispersive motion that actually allows the particles to be intercepted by the shear layer at the roof top and brought outside the cavity. This interpretation is in line with the analysis reported in [Salizzoni et al., 2009]. In this previous work, the wash-out time varied with the intensity of the turbulent fluctuations within the cavity, induced in turn by a variation of the flow statistics of the external flow. Here, we are instead keeping the external flow unaltered but we are modifying the conditions within the cavity.

In light of the present experimental results and of the analysis proposed in [Salizzoni et al., 2009], we further investigate in this section the dependency of the wash-out velocity on the fluctuating component of the turbulent flow. To this aim, we first estimate the velocities u_d and $\tilde{u}_d$ for all the experimental configurations in which the model with two degrees of freedom can be applied, i.e. the configurations in which only one or two vortices are clearly established in the cavity. These include the experiments in a square cavity with different heat fluxes at the downwind wall (cases 1 to 3 in Fig. 5.24), and the case of an isothermal cavity with aspect ratio $H/W = 2$ (case 7). For $H/W = 3/2$, we consider the configurations with $\Delta T = 0$ K (the flow field has a single-vortex structure), $\Delta T = 140$ K and $\Delta T = 170$ K (the flow field has a two-vortex structure). These are cases 4 to 6 in Fig. 5.24. Other configurations are not considered as, in case of transition from one to two vortices, the model with two degrees of freedom fails to describe adequately the wash-out process.

Velocities u_d and $\tilde{u}_d$ are plotted against TKE levels inside the cavity. In particular, since each velocity describes the rate of pollutant transfer out of a specific region of the cavity (box_1 and box_2 in Fig. 5.10), we calculate for each one of these regions the spatial average of the TKE from PIV data. In Fig. 5.24, the spatially averaged TKE for each region is plotted against the corresponding wash-out velocity. For each configuration (numbers 1 to 7), the blue and orange markers report the results for box_1 and box_2, respectively. The error bars represent the uncertainty of the results associated with the two parameters γ and β of the wash-out model (see Section 5.10). As expected, results show a positive correlation between TKE and the wash-out velocity. Interestingly, a clear linear relationship can be observed for u_d (blue markers), i.e. for the velocity characterizing the exchange at the roof level. The interpretation of the behaviour of $\tilde{u}_d$ (orange markers) is less straightforward. For configurations with a single main vortex (1 to 4) the internal exchange velocity slowly grows with TKE. In configurations with two counter-rotating vortices (5-7), the non-dimensional exchange velocity $\tilde{u}_d$ is larger than in single-vortex configurations. A dependence with the local TKE levels is however less easy to enlighten,

also due to the non-negligible extent of the error bars, the limited number (only three) of data points available in the present analysis, and the lack of a perfect two-dimensionality of the flow in the lower cell. The existence of different trends of $\tilde{u}_d$ as a function of u_* further suggests that (differently from the case of u_d) this exchange process may be affected by the topology of the mean flow. Enlightening this feature would require a more in-depth analysis of the transport mechanisms and further measurements in a wider range of flow conditions.

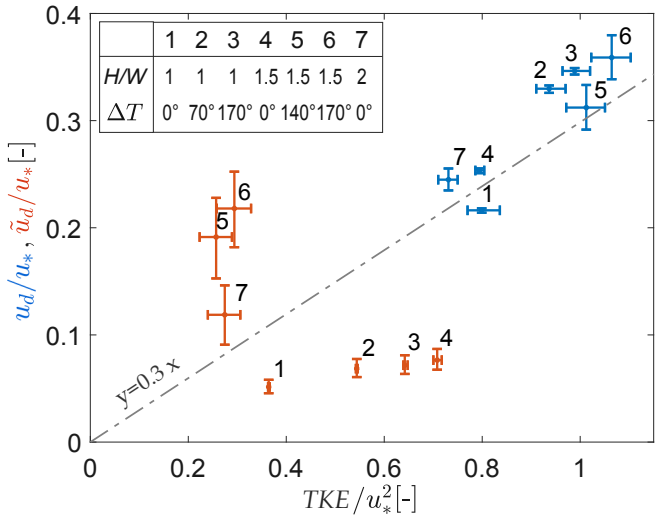

Figure 5.24: Wash-out velocity u_d (blue markers) and $\tilde{u}_d$ (orange markers) against the mean TKE in the corresponding region. Numbers 1-7 indicates the different experimental configurations. The dash-dotted line is the result of a linear regression through the origin of all the points shown in the chart.

Chapter 6

Effect of trees

Urban vegetation plays a key role for the livability of a city [Bozovic et al., 2017]. Beyond its aesthetic role, the presence of vegetation brings numerous environmental benefits in urban areas. Evapotranspiration from leaves and shading from trees have cooling effects that mitigate the urban heat island [Oliveira et al., 2011, Georgakis and Santamouris, 2017]. The large surface area per unit volume of vegetative structures facilitates particle deposition which acts as a sink for pollutant particles [Litschke and Kuttler, 2008]. Moreover, vegetation has a fundamental role in the hydrological cycle. Water interception by tree crowns retards and retains stormwater from entering the drainage system, thus reducing the risk of flash floods [Livesley et al., 2016].

While the social and environmental benefits of vegetation in cities are well recognized, the role of trees and shrubs on pollutant dispersion are still controversial [Janhäll, 2015]. The typical scenario is the presence of tree rows in street canyons. Trees, acting as obstacles, can obstruct the wind flow thus reducing canyon ventilation and leading to higher pollutant concentrations at the pedestrian level.

A pioneering series of wind tunnel experiments was performed by *Gromke et al.* to investigate this scenario. In their first studies, trees were modelled as a row of small-scale trees with spherical, permeable crowns on thin stems, placed in the middle of a street canyon [Gromke and Ruck, 2007]. The wind was perpendicular to the canyon axis. The flow field within the canyon and the concentration at the canyon walls were explored by varying different properties of the trees (crown diameter, tree height, tree spacing). A relevant increase of concentration at the upwind wall and a slight decrease of concentration at the downwind wall were observed. These variations were more marked when the canyon was occupied by the greatest volume of vegetation (large diameter of crowns and small distance between the trees). To better investigate the effect of tree crown porosity, in a later study, trees were replaced with a metallic cage filled with different amounts of synthetic wadding

material [Gromke and Ruck, 2009]. They found that concentrations are sensitive to crown porosity only in the high porosity range. Adopting the same metallic cages, *Buccolieri et al.* simulated a large street canyon (height to width ratio $H/W = 0.5$) with two rows of trees [Buccolieri et al., 2009, Buccolieri et al., 2011]. They also analysed the case of an approaching wind inclined by 45° with respect to the street axis. The aspect ratio of the canyon and the wind direction turned out to be more influential with respect to vegetation density and crown porosity. However, they evidenced that neglecting the presence of vegetation in the streets would lead to significant errors in the predictions.

While RANS tended to overestimate the concentration in the vegetated streets (e.g., [Gromke et al., 2008, Buccolieri et al., 2009, Buccolieri et al., 2011]), LES (e.g., [Salim et al., 2011]) provided a better agreement with the wind-tunnel experiments, but at a significantly higher computational cost.

Despite remarkable advances in numerical models, simulating complex and porous geometries such as trees and their effect on pollutant dispersion still represents a challenge. Wind tunnel experiments are thus highly recommended to improve and validate existing models.

In this chapter, we present the preliminary results of a wind tunnel experiment aimed at evaluating how tree planting influences the concentration field within a street canyon. An idealised urban district was simulated by an array of square blocks. Within this urban geometry, two rows of model trees were arranged at the sides of a street canyon oriented perpendicularly with respect to the wind direction. Three configurations with different spacing between the trees were considered. A passive scalar was injected from a line source placed at ground level to simulate traffic emissions. Concentration measurements were performed in several cross-sections of the street canyon to investigate the effect of trees on the spatial distribution of pollutants. Moreover, the exchange velocity between the street canyon and the overlying atmosphere was estimated to quantify the overall canyon ventilation under different planting densities. The preliminary results evidence the non-negligible role of trees in the dynamics of pollutant dispersion within the streets and strengthen the need for further experimental studies.

Section 6.1 presents the aerodynamic characterization of the model trees adopted in this study. Section 6.2 deals with flow and dispersion dynamics in a street canyon with vegetation.

6.1 Characterization of the model trees

To investigate the effect of trees in urban areas by means of wind tunnel experiments, buildings and vegetative structures need to be modelled in small scale. Similarity criteria are then necessary to transfer small-scale wind tunnel findings

to full-scale applications. For impermeable and rigid structures, like buildings, dynamical similarity between the experiment and the real application exists if the value of the Reynolds number is the same and if the model and the full-scale object are geometrically similar [Tritton, 2012]. On the other hand, less knowledge is available about the appropriate similarity criteria for vegetative structures. From a fluid dynamical point of view, vegetation is a complex porous medium made of branches and leaves giving rise to the development of boundary layers, wakes and recirculation zones [Gromke and Ruck, 2008]. Moreover, due to their flexibility, trees can sway with the wind and induce fluid-structure interactions.

In previous wind tunnel experiments, trees, windbreaks and canopies have been modelled by using the most varied materials, e.g., brushes, cotton balls, metal screens, plastic stripes, and plastic trees for model railway scenery. Aerodynamic validation of the adopted structures was done by analysing different fundamental features of the interaction between the trees and the flow field, as the drag coefficient, the characteristics of the wakes behind the trees [Meroney, 1968], the ratio between tree height and roughness length [Meroney, 1980], the leaf area density [Chen et al., 1995], or the sway frequency [Stacey et al., 1994]. More systematically, in [Gromke and Ruck, 2008] the authors analysed the aerodynamic characteristics of 12 small-scale modelled trees made of different materials and porosity. Measurements of the drag coefficient and of the flow field around the crowns evidenced the drag coefficient as a key scale parameter for the wind tunnel modelling of trees. *Manickathan et al.* compared the aerodynamic behaviour of model and natural trees in a wind tunnel [Manickathan et al., 2018]. They found that, together with the drag coefficient, the aerodynamic porosity of the tree crown is another vital parameter to compare natural and model trees. Moreover, at high wind speeds, model trees should also have reconfiguration characteristics, i.e. they should have flexible branches able to orientate along the wind direction.

In accordance with these studies, we mimicked natural trees with plastic trees for railway modelling and we characterized their aerodynamic behaviour by estimating their aerodynamic porosity and their drag coefficient. The trees were 8.5 cm high (h_T) and 4.5 cm wide (w_T), with crowns in plastic porous material on rigid plastic trunks.

6.1.1 Experimental set-up and measurement techniques for tree characterization

The drag coefficient of the model trees was measured in a small closed-circuit wind tunnel with a 30 cm x 30 cm test section. The tunnel was equipped with an external load cell with a precision of 0.01 N, positioned at one of its lateral walls (Fig. 6.1). Different layouts of trees were attached to a removable plate connected with the load cell. The plate was perfectly flush with the side wall of the tunnel but a lateral gap of about 1 mm between the plate and the wall guaranteed that

the plate was completely separated from the wind tunnel. The drag coefficient of different tree layouts was estimated for a varying wind velocity inside the tunnel, which was measured by means of a Pitot tube with a precision of 0.1 m/s.

Figure 6.1: Lateral view of the small closed-circuit wind tunnel at the Ecole Centrale de Lyon used for the characterization of tree drag coefficient.

The aerodynamic porosity of the model trees was measured in the atmospheric wind tunnel that will be described in detail in Section 6.2.1. Velocity measurements upwind and downwind a single tree were performed on a regular grid by means of the Pitot tube.

6.1.2 Aerodynamic porosity and drag coefficient of the model trees

Aerodynamic porosity (α_p) is defined [Guan et al., 2003] as the ratio of the average wind speed behind the obstacle (U_b) and the average speed of the approaching wind (U_0):

$$\alpha_p = \frac{\int_{A_c} U_b(x,y,z)dA_c}{\int_{A_c} U_0(x,y,z)dA_c}, \tag{6.1}$$

where A_c is the projected frontal area of the obstacle. In other words, aerodynamic porosity determines the portion of the flow that passes through the porous material with respect to the flow that diverges from the obstacle.

To estimate α_p, Eq. 6.1 can be adopted if velocity measurements can be directly performed. Alternatively, the aerodynamic porosity can be derived from the optical porosity (β_p) by using the empirical relationship found experimentally in [Guan et al., 2003]:

$$\alpha_p = \beta_p^{0.4}. \tag{6.2}$$

The optical porosity β_p is the ratio between the open surface of a porous material and its total surface. It is commonly used, since it can be easily estimated by elaborating digital photos. In this study, we adopted both methods and compared the results.

Fig. 6.1.a shows the frontal view of the model tree. Through a digital elaboration of the photo, we delimited the silhouette of the tree and obtained the cross-section, $A_c = 3.5 \cdot 10^{-3}\ m^2$. Then, we estimated the optical porosity, $\beta_p = 0.05$, as the ratio of the number of white pixels to the total number of pixels within the silhouette of the tree. Adopting Eq. 6.2, we finally derived the aerodynamic porosity, $\alpha_p = 0.30$.

To directly estimate α_p, we directly performed velocity measurements upstream and downstream a single tree. For each of these two positions, point velocities were measured on a regular and dense grid and a two-dimensional velocity field was obtained through spatial interpolation. The average velocity was then estimated by integrating the velocity field over the tree silhouette (Fig. 6.2.b) The mean speed upstream and downstream the tree were 4.95 m/s and 1.48 m/s, respectively. By means of Eq. 6.2, we thus obtained a value for the aerodynamic porosity very similar to the one found with the first method.

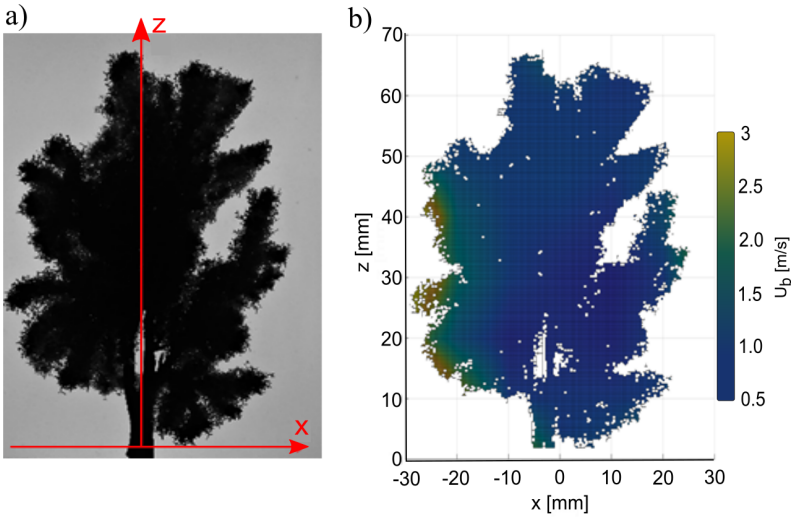

Figure 6.2: a) Frontal picture of the model tree. b) 2D velocity field downstream the tree obtained by spatial interpolation of point velocity measurements.

The drag coefficient is defined as:

$$c_d = \frac{2F}{\rho_a U_{ref}^2 A_c}, \tag{6.3}$$

where F is the drag force $[N]$, ρ_a is air density $[kgm^{-3}]$, U_{ref} is the reference velocity [m/s] for the approaching wind, and A_c is the projected frontal area of the tree $[m^2]$.

As explained in Section 6.2.1, the drag force F was measured by means of a load cell, while the velocity U_{ref} was measured with a Pitot tube.

In Fig. 6.3.a, we report the drag coefficient as a function of the wind intensity U_{ref} and of the Reynolds number Re for four different faces of a single model tree. Except for the values at low speed (where the relative precision of the measurement is poor), the drag coefficient rapidly converges to a constant value around 0.75. Natural trees undergo foliage reconfiguration and their drag coefficient decays with increasing wind speed [Manickathan et al., 2018]. This is not found in model trees that generally do not deform. Since the maximum velocity adopted in our experiments is around 5 m/s, we are here not interested in reproducing the flexibility of natural trees.

Fig. 6.3.b is adapted from [Manickathan et al., 2018] and reports the drag coefficient and the aerodynamic porosity for natural and model trees analysed in previous literature. With $c_d = 0.75$ and $\alpha_p = 0.5$, the model trees adopted in this study present aerodynamic properties in line with natural trees.

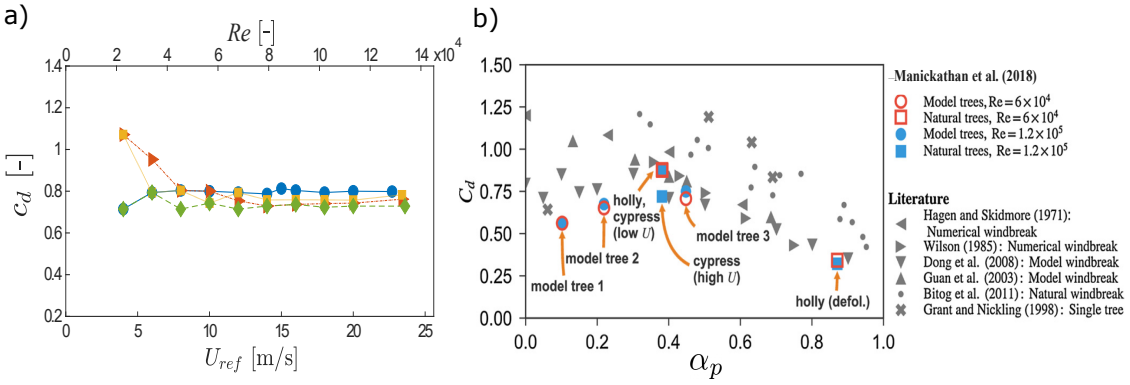

Figure 6.3: a) Drag coefficient as a function of Reynolds number and wind velocity for four different faces of a single model tree. b) Drag coefficient vs. aerodynamic porosity for various model trees and natural trees. From the study of Manickathan et al. (2018) [Manickathan et al., 2018].

6.2 Pollutant dispersion in a street canyon with vegetation

6.2.1 Experimental set-up

The experiments were performed in the atmospheric wind tunnel of the laboratory LMFA (Laboratoire de Mécanique des Fluides et d'Acoustique) at the École Centrale de Lyon. The aerodynamic circuit (panel a in Fig. 6.4) was composed by an axial fan which induces wind velocities between 0.5 and 6 m/s, flow diverging

and converging systems, and an upwind grid for the generation of homogeneous turbulence. A heat exchanger system regulated the air temperature with a precision of 5 K. The test section of the wind tunnel was 12 m long, 3.5 m wide and 2 m high. At a distance of 7 m from the beginning of the test section, a rotating platform with a diameter of 3.5 m could be oriented to simulate different approaching wind directions.

To simulate an idealized urban district (Fig. 6.5), the floor of the entire test section was overlaid with an array of square blocks (panel b in Fig. 6.4). The blocks were 50 cm wide and 10 cm high and made of wood and polystyrene. The spacing between the obstacles was 10 cm in the spanwise direction and 20 cm in the lengthwise direction. In this way, we obtained square street canyons ($H/W = 1$) aligned with the wind direction and larger streets ($H/W = 0.5$) perpendicular to them. The blockage ratio of the model to the cross-section of the wind tunnel was 5%.

A neutrally stratified boundary layer of approximately 1.3 m was generated by combining the effect of a row of 95 cm high Irwin spires [Irwin, 1981], placed at the beginning of the test section, and the building-like obstacles on the floor. Moreover, the obstacles were covered by 5 mm high bolts to generate further roughness and accelerate the full development of the boundary layer. The ratio between the height of the obstacles and the depth (δ) of the boundary layer was around 1/13, ensuring similarity between the simulated and the real urban case. The free stream velocity at the top of the boundary layer (U_∞) was kept constant at 5.5 m/s.

The reference street canyon was placed at the centre of the rotating platform and perpendicular to the wind direction. Its length (L), width (W) and height (H) measured 500 cm, 20 cm and 10 cm, respectively.

To simulate urban vegetation in the street canyon, the model trees described in Section 6.1 were aligned along two lateral rows 14 cm apart (Fig. 6.6). Three different configurations for the tree density were analysed: in Configuration 1, the street canyon was empty. In Configuration 2, five equally spaced trees were arranged along each lateral row. In Configuration 3, the lateral rows were composed of eight trees with no space between them. In a 1:200 scale, the reference street canyon matched fairly well a typical tree-lined boulevard, 40 m wide and flanked by 30 m high buildings, as in typical European city centres (e.g., Barcelona, Turin).

A tracer was emitted by a linear source located in a slot cut in the tunnel floor, in the centre of the reference street canyon. The source consisted of a stainless steel tube pierced with needles emitting the pollutant gas in a 1 cm wide and 40 cm long homogenization chamber, from which the gas was released homogeneously at street level. Ethane was chosen as a tracer, since it has approximately the same density than air. The source released a mixture of air and ethane (5% in volume) with a total flow rate of 4 l/min and a negligible injection velocity of about 0.017 m/s. The mass flow rate of ethane was $Q = 4.3$ mg/s, and consequently the mass flow rate per unit length ($\dot{M}_q$) was 10.8 mg/s·m.

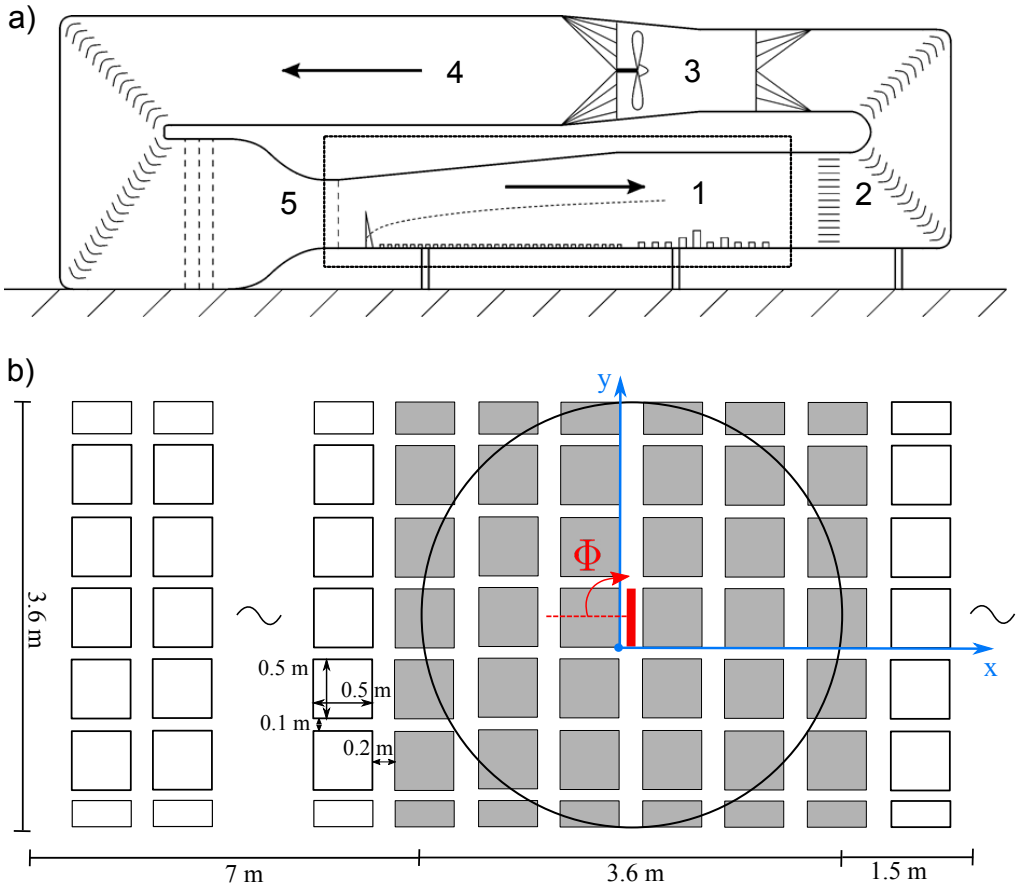

Figure 6.4: a) Wind tunnel at the Ecole Centrale de Lyon: 1 test section; 2 heat exchanger system; 3 fan; 4 diverging system; 5 converging system and generating turbulence grid. b) Sketch of the urban canopy in the test section of the tunnel. The red line represents the pollutant source. Φ is the angle of rotation of the rotating plate and thus the wind orientation with respect to the street canyon (here $\Phi = 90°$).

6.2.2 Measurement techniques

The concentration field within the reference street canyon was measured using the Flame Ionisation Detector (FID) system presented in Section 5.1.2. The measurements were performed in steady conditions: a constant flow rate of ethane was injected from the ground level source and the concentration within the cavity was measured at 116 sampling points distributed over 7 cross-sections (Fig. 6.7). Cross-sections A to D extended along the entire width of the canyon, while cross-sections E to G were narrowed to make space for the model trees. The convergence of the concentration statistics for the FID signal proved that an acquisition time of 2 minutes provides a good estimate of the mean concentration in a sampling point,

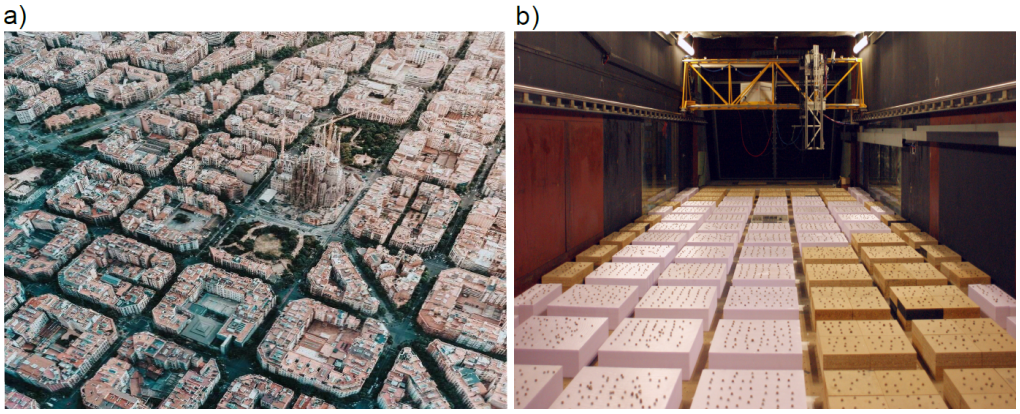

Figure 6.5: a) The urban canopy of Barcelona (Spain). b) The idealized urban district in the test section of the wind tunnel.

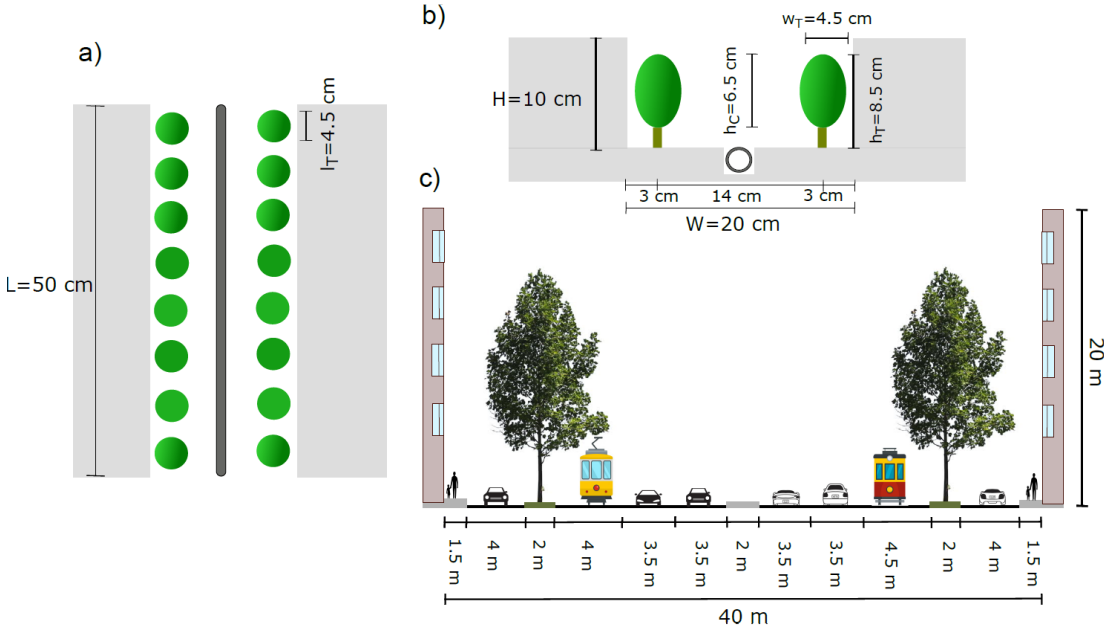

Figure 6.6: Plan (a) and section (b) of the street canyon model. c) Qualitative representation of a real street with the same proportions as the model.

while for the higher moments a longer acquisition time would be required.

The velocity field above the obstacles was characterized by means of a constant-temperature hot-wire anemometer. The technique is based on the heat transfer principle: the hot wire, maintained at a constant temperature, is cooled by the local flow. By measuring the current required to maintain constant the temperature of the wire, the heat lost is obtained and converted into a flow velocity in accordance with convective theory [Comte-Bellot, 1976]. Typically, the anemometer wire is

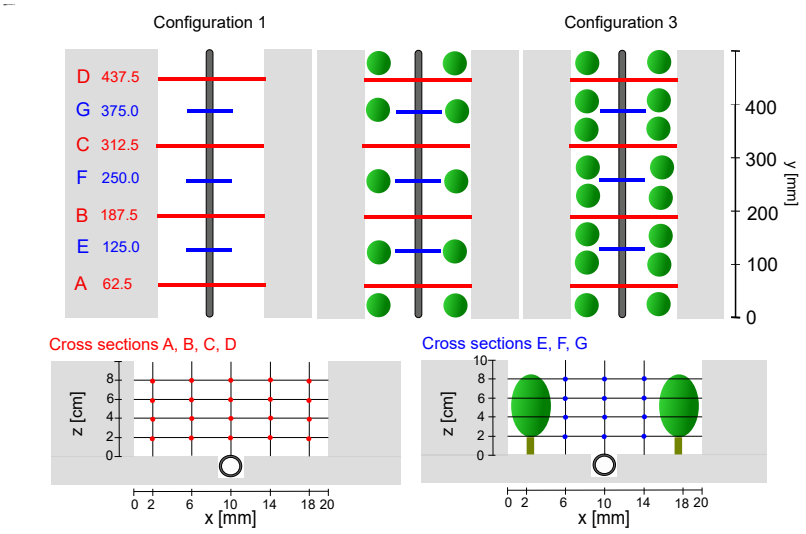

Figure 6.7: Sketch of the street canyon with the three different configurations of tree density. The scheme for concentration measurements is also reported.

made of platinum or tungsten and is 4∼10 μm in diameter and 1∼5 mm in length. The small size of the hot-wire element enables good spatial resolution of the velocity field and the correspondingly low thermal inertia ensures fast response. In this study, we adopted a 45° X-probe anemometer with two hot wires arranged in a X configuration, oriented at 45° to the direction of the flow. In this way, two velocity components of the velocity field were measured simultaneously. An acquisition time of 2 minutes at a frequency of 1000 Hz was adopted for each sampling point.

6.2.3 Characterization of the wind profile above the obstacles

To evaluate weather the boundary layer in the wind tunnel was representative of a well-developed urban boundary layer, we measured the vertical wind profile in different positions of the wind tunnel. For practical reasons concerning the installation of the hot-wire anemometer, the full characterization of the boundary layer was made only up to one meter from the wind tunnel floor. By means of subsequent measurements we however identified the height of the boundary layer $\delta = 1.3\ m$.

The evolution of the boundary layer along the central axis of the wind tunnel is shown in Fig. 6.8.a. The good overlapping between the curves reveals that the flow is fully developed when it approaches the reference canyon ($x = 0$), i.e. its development in the stream-wise direction is so slow that changes over the fetch can be neglected.

As mentioned in the Introduction of this thesis, we expect the lower part of the boundary layer to be composed of two layers: (i) the roughness sublayer, where the flow is strongly influenced by the individual roughness elements and presents horizontal inhomogeneity, and (ii) the inertial sublayer, where horizontal inhomogeneities are negligible and the mean velocity profile is well described by the logarithmic profile law (see Eq. 2).

To investigate the extent of the roughness sublayer, we measured the vertical profile of the flow variables at 4 different positions near the reference canyon, within a periodic unit of the urban canopy (see the inset in Fig. 6.8.b). The influence of the buildings is clear in the lower part of the profiles where a high scatter can be observed up to $z = 250$ mm. This height can be considered as the upper limit of the roughness sublayer and it's defined as the blending height z^*. Above this height, the curves tend to collapse to follow the logarithmic law profile characterized by three fundamental parameters: the aerodynamic roughness (z_0), the zero-plane displacement (d), and the friction velocity (u_*). Different techniques can be adopted to estimate these parameters. The friction velocity u_* can be inferred from the Reynolds shear stress profile ($-\langle u'v' \rangle$). Across the boundary layer, the total stress ($\tau = \rho_a u_*^2$) is given by the contributes of the viscous stress and the Reynolds stress. Except for a thin layer close to the wall, where viscous effects are dominant, the total stress almost matches with the Reynolds stress, which is observed to be almost constant in the surface layer. As a consequence, the value of $-\langle u'v' \rangle$ in the constant-stress region identifies the value of the surface stress at the wall: $\tau(0) = \rho_a u_*^2 = -\langle u'v' \rangle$. Following this method, we have analysed the vertical profile of the Reynolds stresses (Fig. 6.9.a) which was obtained as a spatial average over the four horizontal positions reported in the inset of Fig. 6.8. A constant-stress region was detected for $150 < z < 400$ mm. The corresponding value for u_* was estimated equal to 0.26 m/s. We then estimated the aerodynamic roughness z_0 and the zero-plane displacement d through a linear regression of the logarithmic law in the semi-log domain (Fig. 6.9.b). We obtained $z_0 = 0.8$ mm and $d = 96$ mm. The estimated parameters are in line with previous experimental studies [Rafailidis, 1997, Salizzoni, 2006, Garbero et al., 2010].

6.2.4 Considerations about the flow field in the street canyon

Differently from the experimental campaign presented in Chapter 5, the flow field in the street canyon was not directly characterized. However, we can derive its fundamental features from previous literature.

The aspect ratio (H/W) of the street canyon is 0.5. Thus, accordingly to [Oke, 2002], the flow developing between the obstacles is expected to be a *wake interference flow* (Fig. 3.c): the buildings are too far apart to form a skimming

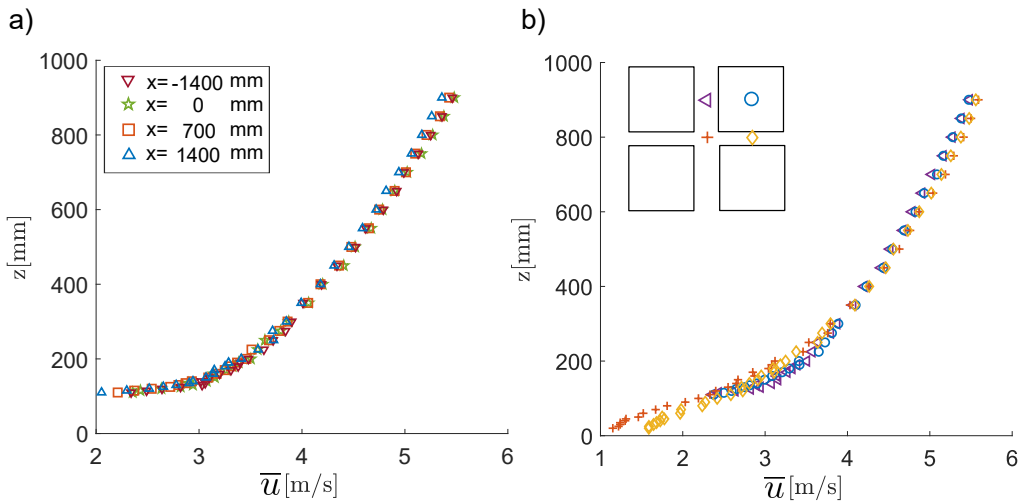

Figure 6.8: a) Vertical profile of the mean velocity along the streamwise direction of the wind tunnel. b) Vertical profiles of the mean velocity at 4 different position above the canopy, close to the reference canyon.

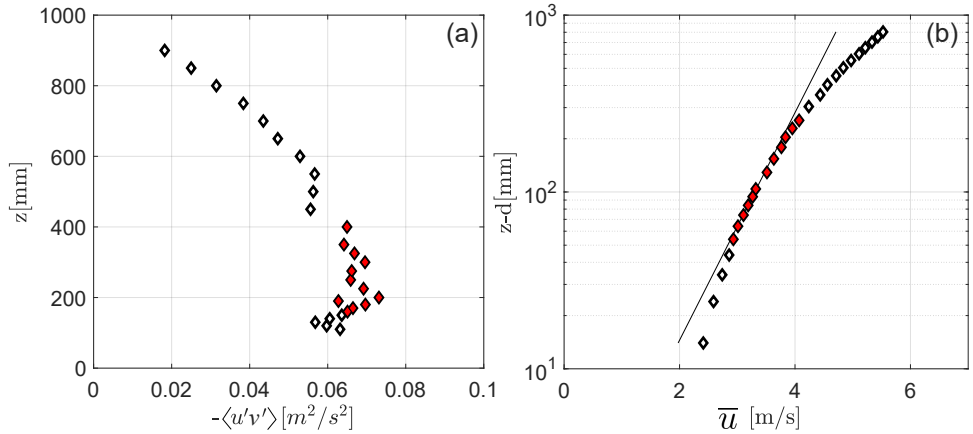

Figure 6.9: a) Vertical profile of the shear stress profile obtained as average over four different positions. The full symbols indicate the constant-stress region. b) Vertical profile of the mean velocity obtained as average over four different positions. The line represents the logarithmic law with $d = 96$ mm and $z_0 = 0.8$ mm. The full symbols indicate the region where the logarithmic law applies (inertial sublayer).

flow (Fig. 3.d), but they are close enough for the recirculation zone downstream of an obstacle to interact with the vortex located upstream of the next obstacle. For $H/W = 0.5$, the main clockwise vortex extends from one wall to the other (as in the skimming flow regime) while a tiny counter-rotating vortex appears close to the downwind wall [Sini et al., 1996]. In the wake interference regime the shear layer

at the roof level is highly unstable [Louka et al., 2000] and the canyon ventilation is regulated by the intermittent shedding of vortices from the external flow, whose length scale is proportional to the building height (H).

Another fundamental parameter for the characterization of the flow field within the canyon is its length. Differently from the experiments presented in Chapter 5, the canyon length is here finite with $L/H = 2.5$. In this configuration, corner eddies develop at the street edges and interact with the main vortex that occupies the middle part of the canyon 3.a. The flow field in the canyon is thus strongly three-dimensional.

Previous works [Soulhac, 2000], based on a similar experimental set-up, also evidenced the presence of a non-zero mean advective flow from the intersections towards the centre of the street (Fig. 6.10). Given this lateral inlet flow and given the continuity principle, the presence of a mean vertical flow out of the upper surface of the canyon (at the height of the roofs) was also expected and found though numerical simulations. However, referring to canyon ventilation, the intensity of these velocities was observed to be negligible compared to the exchanges induced by the turbulent fluctuations at the interfaces.

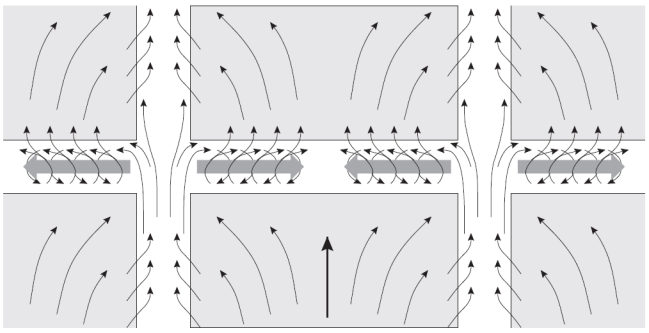

Figure 6.10: Transversal flux in finite streets perpendicular to the wind direction. Adapted from [Soulhac, 2000].

6.2.5 Pollutant concentration in the street canyon

For different configurations of tree density (Configurations 1 to 3 in Fig. 6.4), the passive scalar concentration within the canyon was measured by means of a Flame Ionization Detector (Section 6.2.2). Measurements were performed over 4 cross-sections (sections A to D) covering all the canyon width, and 3 narrower cross-sections (sections E to G) covering the central part of the canyon (Fig. 6.4).
Fig. 6.11 shows the concentration field in sections A to D, for the different configurations of tree density (rows a to c). The non-dimensional concentration is expressed as $\overline{c}u_*H/\dot{M}_q$, where $\overline{c}$ is the time averaged concentration of ethane in each sampling point, u_* is the friction velocity, H is the height of the canyon and

$\dot{M}_q$ is the mass flow rate of ethane for unit length. The two-dimensional fields were obtained by spatial interpolation of the concentration at the sampling points.

Regardless of the presence of vegetation and the position along the longitudinal axis of the canyon (y), the concentration at the upwind wall ($x \to 0$ mm) is considerably higher than that measured at the downwind wall ($x \to 200$ mm). This is evidenced by Fig. 6.12.b which shows the trend of pollutant concentration along the x axis, as an average along cross-sections A to D. This differential distribution of pollutants along the x axis can be explained by referring to the case of a square cavity (see Chapter 5): turbulent kinetic energy from the external flow spreads down into the canyon along the downwind wall. Here, TKE levels are maximum and the turbulent transport is enhanced. Due to the lower level of turbulent kinetic energy, the exchange is inhibited at the upwind wall, where pollutants accumulate, especially at the pedestrian level.

As trees are added in the street, concentration increases in each section (rows b-c in Fig. 6.11). This suggests that the presence of trees alters the turbulent field and inhibits the canyon ventilation. This trend is more pronounced in the end sections (sections A and D), where concentration at the upwind wall increases more than twice. These observations are confirmed by Fig. 6.12.b which shows the average concentration for each cross-sections as a function of the tree density. In the case without trees (blue line), the concentration is higher in the centre of the canyon (sections B and C), while the corner eddies that develop near the intersections (Fig. 3) provide additional turbulent exchange that favors the reduction of concentration in the extreme sections (sections A and D). In Configurations 2 and 3 (orange and green lines), the trend along y is the opposite: the highest concentrations are measured in the extreme sections (A and D), where the presence of trees hinders the lateral exchange induced by the corner eddies. Similar results were observed in the experimental study in [Gromke and Ruck, 2007]. On the other hand, differently from previous studies [Gromke and Ruck, 2007, Buccolieri et al., 2009], we do not observe a decrease in concentration at the downwind wall due to tree planting (see the trend for $x = 180$ mm in Fig. 6.12.a).

Finally, we show in Fig. 6.13.a the mean concentration estimated as spatial average on the entire domain of the canyon. The overall concentration of pollutants increases up to 33 % in Configuration 2, where 5 trees are arranged along each lateral row, and up to 47 % in Configuration 3, where the density of trees is the highest within the canyon (8 trees along each lateral row).

6.2.6 The wash-out velocity

The preliminary results presented above suggest that the flow field - and consequently the concentration field - inside the canyon is strongly three-dimensional.

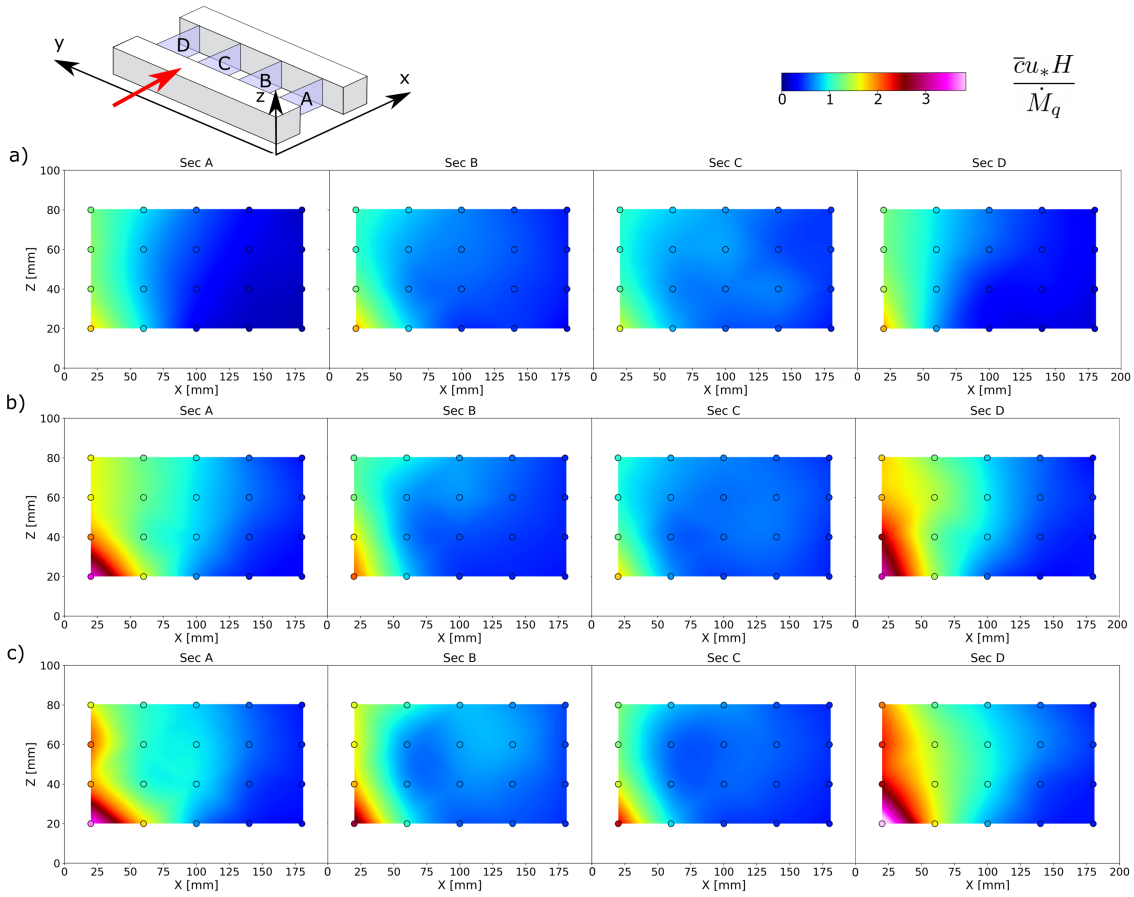

Figure 6.11: Concentration of ethane in cross-sections A to D for (a) Configuration 1 (no trees), (b) Configuration 2 (spaced trees), (c) Configuration 3 (packed trees). Circles indicate the position of the sampling points.

This is due primarily to the finite length of the canyon, and secondly to the presence of trees which act as three-dimensional obstacles.

Given the complexity of the flow field, we avoid to describe ventilation dynamics as a sequence of transfers between canyon regions. Thus, differently from the study presented in Chapter 5, we here adopt a box model with one degree of freedom to evaluate the wash-out velocity of the canyon.

The canyon is described as a unique box with mean concentration (C), a discontinuity surface at the roof height (of extent $L \cdot W$) and two lateral surfaces at the canyon edges (of extent $W \cdot H$). Following the same steps presented in Section 5.2.1, we can derive the mass balance for the canyon:

$$V_{tot}\frac{\partial C}{\partial t} + \int_0^H \int_0^W \left[\langle wc_t \rangle\right]_{y=0}^{y=L} dxdz + \int_0^L \int_0^W \left[\langle vc_t \rangle\right]_{z=H} dxdy = Q, \tag{6.4}$$

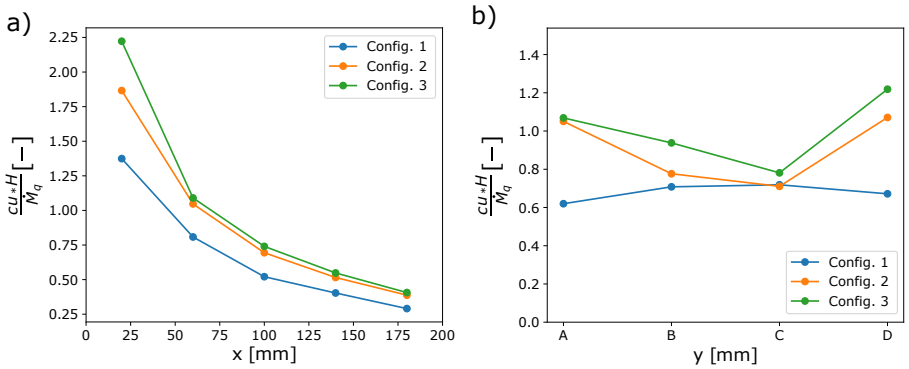

Figure 6.12: a) Mean concentration for sections at different x (oriented perpendicular with respect to the wind direction) as a function of tree density. b) Mean concentration for cross-sections A to D (i.e., at different y positions) as a function of tree density. Configuration 1 (no trees), Configuration 2 (spaced trees), Configuration 3 (packed trees).

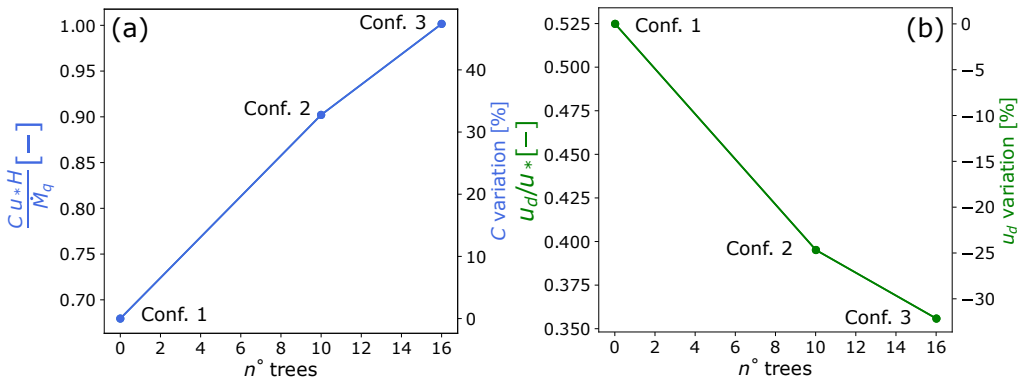

Figure 6.13: a) Average concentration of pollutants in the street canyon for different tree densities. b) Bulk transfer velocity between the street canyon and the external flow as a function of tree density.

where V_{tot} is the volume of the canyon, Q is the mass flow rate of ethane at the source (i.e. $\dot{M}_q$ multiplied by the source length), C is the mean concentration in the canyon, $\langle wc_t \rangle$ is the flux of passive scalar along the longitudinal direction y, and $\langle vc_t \rangle$ is the flux of passive scalar in the vertical direction. Differently from the case of an infinite canyon, presented in Chapter 5, the transfer at the canyon edges is barely negligible here. As for the vertical transfer, we can introduce a parametrization for the exchange at the canyon edges. Assuming the external concentration equal to

0, and recalling Eq. 1.7, we have:

$$u_d = \frac{1}{LWC}\int_0^L\int_0^W \left[\langle vc_t\rangle\right]_{z=H} dxdy \tag{6.5}$$

$$u_L = \frac{1}{HWC}\int_0^H\int_0^W \left[\langle wc_t\rangle\right]_{y=L} dxdz, \tag{6.6}$$

$$u_0 = -\frac{1}{HWC}\int_0^H\int_0^W \left[\langle wc_t\rangle\right]_{y=0} dxdz, \tag{6.7}$$

where u_L and u_0 represent the exchange velocities at the transversal sections in $y = L$ and $y = 0$, while u_d is the bulk exchange velocity in the vertical direction at roof level ($z = H$). Notice that when the wind is aligned with respect to the canyon, the pollutant flux along the canyon axis is mainly given by the mean transport ($\langle w\rangle\langle c_t\rangle$), and the fresh air entering the canyon at $y = 0$ gives a null contribution in the concentration budget. The velocity u_L is thus the only transfer velocity in the longitudinal direction and can be approximated with the mean velocity u_{st}, introduced in Chapter 1. On the other hand, for a perpendicular wind, the mean transport at the intersections can be neglected with respect to the turbulent one and the two transfer velocities u_L and u_0 can be assumed equal: $u_L \simeq u_0 \simeq u_t$. Thus, in stationary conditions, the balance in Eq. 6.4 becomes:

$$Q = LWu_dC + 2WHu_tC, \tag{6.8}$$

For the experiment presented here, both the exchange velocities (u_d and u_t) are unknown while the flow rate at the source Q is directly measured by a mass flow rate, and the FID measurements inside the street canyon provide the average concentration in the entire volume (C). To approximately estimate u_d from the available data, we assume that the same transfer velocity drives the turbulent exchange at the top and lateral sections. With this assumption, Eq. 6.9 becomes:

$$Q = (L + 2H)Wu_dC, \tag{6.9}$$

and u_d can be easily estimated for the different configurations of tree density. Fig. 6.13.b shows that the transfer velocity decreases up to 32% when two full rows of trees run along each side of the street.

The value of u_d in the case without trees (Conf. 1) is more than twice the value obtained by [Salizzoni, 2006] for an infinite canyon with the same aspect ratio (Configuration 3a in [Salizzoni, 2006]). Despite the approximations applied for the estimation of u_d, the difference in results between the two experimental studies confirms that the lateral intersections play an important role in the ventilation of the canyon. Concerning the role of vegetation, the presence of trees at the canyon edges seems to inhibit the lateral ventilation and may have a significant role in the exchange at roof level. We expect that the presence of trees introduces a new

characteristic length scale for the system, and that consequently the size of the dominant turbulent structures in the shear layer is reduced. This would weaken the coupling between the external and internal flow with a consequent inhibition of the vertical ventilation.

These hypotheses are the basis of a new experimental campaign currently underway. Coupled measurements of velocity and concentration at the discontinuity surfaces of the canyon are planned for a direct estimate of the exchange velocities u_d and u_L (see Eq. 6.5). Moreover, a spectral analysis of the vertical turbulent transport will reveal any change in the turbulent scales in the shear layer.

Concluding remarks of Part II

We have investigated the vertical exchange of pollutants between a street canyon and the external flow. We have considered the case of a wind blowing perpendicular to the axis of the street. To grasp the physical mechanisms that govern the canyon ventilation, we have performed multiple wind tunnel experiments covering a wide range of street canyon configurations. In particular, we have analysed different canyon geometries, thermal conditions at walls and the presence of vegetation within the canyon.

In accordance with previous works, results have evidenced that turbulent kinetic energy is the main driver for ventilation in a canyon perpendicular to the wind direction. The flow field within the canyon, and thus concentration levels, strongly depend on the condition imposed at the canyon walls.

As the aspect ratio of the cavity increases, the total anticlockwise vorticity fluxes at the cavity walls increase as well. This feature induces the formation of a second counter-rotating cell that hinders the penetration of turbulent kinetic energy from the external flow, thus inhibiting the canyon ventilation. As a consequence, in narrow canyons air quality at the pedestrian level is worsened.

Wall roughness enhances velocity gradients near the walls, inducing higher fluxes of anticlockwise vorticity. Adding roughness to the downwind wall facilitates the transition to two recirculating cells, while roughness elements at the upwind wall slightly influence the velocity field since the enhanced anti-clockwise vorticity is rapidly advected outside the cavity by the mean motion.

Thermal fluxes at the upwind wall have negligible effects on both the mean and TKE fields. Similarly to wall roughness, the heating of the upwind wall produces clockwise vorticity that is transferred outside the cavity before affecting the flow.

From the environmental point of view, the heating of the downwind wall has opposite effects depending on the street aspect ratio. In a square cavity, the thermal fluxes are not strong enough to modify the topology of the mean flow streamlines, but their effect is relevant on the intensity of the TKE, which is increased in the whole cavity. This increase in TKE seems to be associated to the acceleration of the wash-out from the canyon to the overlying atmospheric flow, with a resulting reduction of the passive scalar concentration within the canyon. As the aspect ratio of the cavity increases, the heating of the downwind wall has growing effects on the velocity field. For $H/W = 1.5$, the heating of the wall facilitates the formation of the second cell at the bottom of the canyon, thus slowing down the wash-out process. As a consequence, pollutants accumulate at street level with consequent deterioration of air quality.

The preliminary results about the effect of tree planting in streets suggest that the presence of trees causes a reduction of turbulence kinetic energy within the canyon and a lower transfer velocity towards the external flow, leading to higher concentration inside the canyon, especially at the upwind wall.

The comprehensive analysis of multiple configurations involving different physical aspects (geometry, roughness, heating, tree planting) displays how the different parameters interact, and traces a link between the acceleration in the wash-out process and the increase in the TKE levels, in accordance with the analysis of [Salizzoni et al., 2009].

However, further experimental studies are highly recommended. In particular, measurements of the turbulent and mean components of the vertical pollutant fluxes would be helpful to clarify the role of TKE in canyon ventilation.

Conclusions and perspectives

The aim of this thesis was to investigate the effect of urban form on pollutant dispersion in the urban atmosphere and to identify the dominant transport mechanisms.

The study focused on two spatial scales: the scale of the city and the scale of the single street canyon. At the city scale, pollutant propagation from a point source was modeled by adopting an innovative approach based on the theory of complex networks. The main result was the generation of vulnerability maps showing the places in a city with the highest potential for the spreading of airborne pollutants. Moreover, the new modelling approach unveiled the dominant role of urban topology in driving the propagation of pollutants over large distances.

An experimental approach was instead adopted to investigate dispersion dynamics within a single street canyon. We analysed how the vertical exchange between the canyon and the atmosphere above buildings varies with the canyon geometry, the conditions at the building walls, and the presence of obstacles within the canyon. Furthermore, our results proved that the vertical exchange is regulated by the turbulent kinetic energy field within the canyon.

General conclusions. Besides the specific results, the following general conclusions and observations can be drawn from this work.

- The urban form plays a key role in the breathability of cities. At the city/district scale, urban topology drives the propagation paths that are dominated by advection. The urban plan can therefore mitigate the impact of gaseous releases. At the scale of the single street, ventilation depends on the orientation with respect to the wind direction and on the geometry of the canyon. In particular, the vertical exchange is affected by the aspect ratio and the conditions at the building walls.

- The study and modeling of dispersion processes in the urban atmosphere requires a multi-scale approach, as the mechanisms involve multiple spatial and temporal scales. For this purpose, different techniques are generally adopted and may involve scientific communities with different expertise. In this context, knowledge sharing is a key aspect to bring together the different approaches and to create positive feedbacks in the scientific community. A

simple example of this synergistic effort is reported in this thesis: the experimental study is the basis for a parameterization of the vertical exchange velocity which represents one of the fundamental parameters in the simplified model of propagation at the city scale.

- Innovative techniques can be successfully adopted to develop operational modeling tools for predicting the transport of pollutants in large urban areas. In this sense, the theory of complex networks has proven to be a versatile tool with low computational cost. The rate at which new techniques and applications are developed in the field of complex networks (in particular, in the field of epidemic spreading on networks) makes this new perspective particularly promising.

- The results of this research provide preliminary indications and tools to urban practitioners and decision-makers. The proposed complex network model is useful to rapidly assess multiple risk scenarios of gaseous release, to identify the most critical areas of a city, and to plan temporary and permanent changes in the urban structure to mitigate the risk. Moreover, results from the experimental campaigns reveal the optimal architectural characteristics for street canyon ventilation, while indications for an efficient tree planting are still in progress.

Limitations and future research. Finally, we briefly suggest some ideas for future research that have arisen from both the limitations and the potential of this thesis.

- Despite the comparison with SIRANE (Section 2.4), an experimental validation of the complex network model is desirable. Wind tunnel experiments are planned in the near future for this purpose. Weaknesses of the model may lie in the assumptions for the exchange at street intersections and for the re-entrainment from the external flow towards the streets. As regards the first limitation, improvements could be obtained by adding a loss term for pollutants in the intersections, and a probability index associated with the different paths that depart from each intersection. Regarding the second limitation, a multilayer network could be constructed to simultaneously model the dynamics within the urban canopy and the dispersion above the buildings. The latter would be simulated on a continuous network as the buildings no longer act as obstacles for propagation. Vertical links between the two layers could be activated to simulate re-entrainment from the external flow towards the buildings.

- The proposed network approach can be easily adapted to deal with other crucial problems in urban environments. By reversing the direction of network links, the developed centrality metric can identify the nodes most easily

reachable by high concentration levels, instead of detecting the best spreader nodes. This shift of perspective from spreaders to receptors suggests applications in inverse modeling, such as the identification of a source position starting from concentration measurements in a certain number of nodes of the network. This problem can be related to the optimal placement of sensors in an air monitoring network to maximize the probability of intercepting dangerous dispersion events. Regarding these applications, it is worth mentioning that cities have great potential in providing data and measurements, thanks to the integration of sensors into existing infrastructure, the use of mobile sensors, and the involvement of citizens.

- A natural extension of this thesis is the development of a parameterization for the vertical exchange velocity that takes into account the factors investigated during the wind tunnel experiments: the aspect ratio of the canyon, the roughness and solar radiation on the building walls, and the presence of trees. This parameterization would be useful to improve city-scale operational models, including the one proposed in this thesis.

- The final chapter of this thesis paves the way for a series of experiments to investigate the effect of vegetation on canyon ventilation. To improve the study, we intend to initially remove street intersections and focus on the vertical exchange mechanism. Coupled measurements of velocity and concentration will be adopted for direct estimation of the exchange velocity and for investigating turbulent structures. Different arrangements of trees and different crown heights will be tested to evaluate the configuration that optimizes street canyon ventilation.

Bibliography

[Abraham et al., 2010] Abraham, I., Fiat, A., Goldberg, A. V., and Werneck, R. F. (2010). Highway dimension, shortest paths, and provably efficient algorithms. In *Proceedings of the twenty-first annual ACM-SIAM symposium on Discrete Algorithms*, pages 782–793. SIAM.

[Adrian, 1997] Adrian, R. (1997). Dynamic ranges of velocity and spatial resolution of particle image velocimetry. *Measurement Science and Technology*, 8(12):1393.

[Ahmad et al., 2005] Ahmad, K., Khare, M., and Chaudhry, K. (2005). Wind tunnel simulation studies on dispersion at urban street canyons and intersections—a review. *Journal of Wind Engineering and Industrial Aerodynamics*, 93(9):697–717.

[Ahujia et al., 1993] Ahujia, R., Magnanti, T. L., and Orlin, J. B. (1993). *Network flows: Theory, algorithms and applications*. New Jersey: Rentice-Hall.

[Albert et al., 2004] Albert, R., Albert, I., and Nakarado, G. L. (2004). Structural vulnerability of the north american power grid. *Physical review E*, 69(2):025103.

[Alexandri and Jones, 2008] Alexandri, E. and Jones, P. (2008). Temperature decreases in an urban canyon due to green walls and green roofs in diverse climates. *Building and environment*, 43(4):480–493.

[Allegrini et al., 2013] Allegrini, J., Dorer, V., and Carmeliet, J. (2013). Wind tunnel measurements of buoyant flows in street canyons. *Building and Environment*, 59:315–326.

[Arnfield, 2003] Arnfield, A. J. (2003). Two decades of urban climate research: A review of turbulence, exchanges of energy and water, and the urban heat island. *International Journal of Climatology*, 23(1):1–26.

[Artime et al., 2017] Artime, O., Ramasco, J. J., and San Miguel, M. (2017). Dynamics on networks: competition of temporal and topological correlations. *Scientific reports*, 7:41627.

[Assimakopoulos et al., 2003] Assimakopoulos, V. D., ApSimon, H., and Moussiopoulos, N. (2003). A numerical study of atmospheric pollutant dispersion in different two-dimensional street canyon configurations. *Atmospheric Environment*, 37(29):4037–4049.

[Baics and Meisterlin, 2019] Baics, G. and Meisterlin, L. (2019). The grid as algorithm for land use: a reappraisal of the 1811 manhattan grid. *Planning Perspectives*, 34(3):391–414.

[Baik and Kim, 1999] Baik, J.-J. and Kim, J.-J. (1999). A numerical study of flow and pollutant dispersion characteristics in urban street canyons. *Journal of applied meteorology*, 38(11):1576–1589.

[Banerjee et al., 2013] Banerjee, T., Katul, G., Fontan, S., Poggi, D., and Kumar, M. (2013). Mean flow near edges and within cavities situated inside dense canopies. *Boundary-layer meteorology*, 149(1):19–41.

[Barabási et al., 2016] Barabási, A.-L. et al. (2016). *Network science*. Cambridge university press.

[Barlow and Belcher, 2002] Barlow, J. F. and Belcher, S. E. (2002). A wind tunnel model for quantifying fluxes in the urban boundary layer. *Boundary-Layer Meteorology*, 104(1):131–150.

[Barthélemy, 2011] Barthélemy, M. (2011). Spatial networks. *Physics Reports*, 499(1-3):1–101.

[Barthelemy, 2016] Barthelemy, M. (2016). *The structure and dynamics of cities*. Cambridge University Press.

[Barthelemy et al., 2013] Barthelemy, M., Bordin, P., Berestycki, H., and Gribaudi, M. (2013). Self-organization versus top-down planning in the evolution of a city. *Scientific reports*, 3(1):1–8.

[Basaras et al., 2013] Basaras, P., Katsaros, D., and Tassiulas, L. (2013). Detecting capable spreaders. *Computer*, page 1.

[Batty, 2009] Batty, M. (2009). Cities as complex systems: Scaling, interaction, networks, dynamics and urban morphologies. *UCL Working Papers Series*.

[Batty, 2013] Batty, M. (2013). *The new science of cities*. MIT press.

[Batty and Longley, 1994] Batty, M. and Longley, P. A. (1994). *Fractal cities: a geometry of form and function*. Academic press.

[Belcher et al., 2015] Belcher, S., Coceal, O., Goulart, E., Rudd, A., and Robins, A. (2015). Processes controlling atmospheric dispersion through city centres. *Journal of Fluid Mechanics*, 763:51–81.

[Berkowicz, 2000] Berkowicz, R. (2000). Ospm-a parameterised street pollution model. *Environmental monitoring and assessment*, 65(1-2):323–331.

[Bettencourt, 2013] Bettencourt, L. M. (2013). The origins of scaling in cities. *science*, 340(6139):1438–1441.

[Bettencourt, 2020] Bettencourt, L. M. (2020). Urban growth and the emergent statistics of cities. *Science advances*, 6(34):eaat8812.

[Bettencourt et al., 2007] Bettencourt, L. M., Lobo, J., Helbing, D., Kühnert, C., and West, G. B. (2007). Growth, innovation, scaling, and the pace of life in cities. *Proceedings of the national academy of sciences*, 104(17):7301–7306.

[Bibri and Krogstie, 2017] Bibri, S. E. and Krogstie, J. (2017). Smart sustainable cities of the future: An extensive interdisciplinary literature review. *Sustainable*

Cities and Society, 31:183–212.

[Bini et al., 2016] Bini, M., Aiello, L., Capitanio, C., and Francini, C. (2016). *Immagine Urbana: Temi e progetti per lo spazio pubblico nel Centro Storico di Firenze*. DIDA.

[Blocken, 2015] Blocken, B. (2015). Computational Fluid Dynamics for urban physics: Importance, scales, possibilities, limitations and ten tips and tricks towards accurate and reliable simulations. *Building and Environment*, 91:219–245.

[Bo et al., 2017] Bo, M., Salizzoni, P., Clerico, M., and Buccolieri, R. (2017). Assessment of indoor-outdoor particulate matter air pollution: A review. *Atmosphere*, 8(8):136.

[Boccaletti et al., 2006] Boccaletti, S., Latora, V., Moreno, Y., Chavez, M., and Hwang, D.-U. (2006). Complex networks: Structure and dynamics. *Physics Reports*, 424(4-5):175–308.

[Borgatti et al., 2009] Borgatti, S. P., Mehra, A., Brass, D. J., and Labianca, G. (2009). Network analysis in the social sciences. *Science*, 323(5916):892–895.

[Bozovic et al., 2017] Bozovic, R., Maksimovic, C., Mijic, A., Smith, K., Suter, I., and Van Reeuwijk, M. (2017). Blue green solutions. a systems approach to sustainable and cost-effective urban development.

[Brandes, 2005] Brandes, U. (2005). *Network analysis: Methodological foundations*, volume 3418. Springer Science & Business Media.

[Brockmann and Helbing, 2013] Brockmann, D. and Helbing, D. (2013). The hidden geometry of complex, network-driven contagion phenomena. *Science*, 342(6164):1337–1342.

[Brunekreef and Holgate, 2002] Brunekreef, B. and Holgate, S. T. (2002). Air pollution and health. *The Lancet*, 360(9341):1233–1242.

[Buccolieri et al., 2009] Buccolieri, R., Gromke, C., Di Sabatino, S., and Ruck, B. (2009). Aerodynamic effects of trees on pollutant concentration in street canyons. *Science of the Total Environment*, 407(19):5247–5256.

[Buccolieri et al., 2011] Buccolieri, R., Salim, S. M., Leo, L. S., Di Sabatino, S., Chan, A., Ielpo, P., de Gennaro, G., and Gromke, C. (2011). Analysis of local scale tree–atmosphere interaction on pollutant concentration in idealized street canyons and application to a real urban junction. *Atmospheric Environment*, 45(9):1702–1713.

[Buccolieri et al., 2015] Buccolieri, R., Salizzoni, P., Soulhac, L., Garbero, V., and Di Sabatino, S. (2015). The breathability of compact cities. *Urban Climate*, 13:73–93.

[Cai, 2012] Cai, X.-M. (2012). Effects of wall heating on flow characteristics in a street canyon. *Boundary-layer meteorology*, 142(3):443–467.

[Carpentieri et al., 2012a] Carpentieri, M., Hayden, P., and Robins, A. G. (2012a). Wind tunnel measurements of pollutant turbulent fluxes in urban intersections. *Atmospheric Environment*, 46:669–674.

[Carpentieri et al., 2012b] Carpentieri, M., Salizzoni, P., Robins, A., and Soulhac, L. (2012b). Evaluation of a neighbourhood scale, street network dispersion model through comparison with wind tunnel data. *Environmental modelling & software*, 37:110–124.

[Carruthers et al., 2000] Carruthers, D., Edmunds, H., Lester, A., McHugh, C., and Singles, R. (2000). Use and validation of ADMS-Urban in contrasting urban and industrial locations. *International Journal of Environment and Pollution*, 14(1-6):364–374.

[Cassiani et al., 2020] Cassiani, M., Bertagni, M. B., Marro, M., and Salizzoni, P. (2020). Concentration fluctuations from localized atmospheric releases. *Boundary-Layer Meteorology*, pages 1–50.

[Castro and Robins, 1977] Castro, I. and Robins, A. (1977). The flow around a surface-mounted cube in uniform and turbulent streams. *Journal of fluid Mechanics*, 79(2):307–335.

[Caton et al., 2003] Caton, F., Britter, R., and Dalziel, S. (2003). Dispersion mechanisms in a street canyon. *Atmospheric Environment*, 37(5):693–702.

[Chang et al., 2006] Chang, K., Constantinescu, G., and Park, S.-o. (2006). Analysis of the flow and mass transfer processes for the incompressible flow past an open cavity with a laminar and a fully turbulent incoming boundary layer. *Journal of Fluid Mechanics*, 561:113–145.

[Chen et al., 1995] Chen, J., Black, T., Novak, M., and Adams, R. (1995). A wind tunnel study of turbulent airflow in forest clearcuts. *Wind and trees*, pages 71–87.

[Comin and da Fontoura Costa, 2011] Comin, C. H. and da Fontoura Costa, L. (2011). Identifying the starting point of a spreading process in complex networks. *Physical Review E*, 84(5):056105.

[Comte-Bellot, 1976] Comte-Bellot, G. (1976). Hot-wire anemometry. *Annual review of fluid mechanics*, 8(1):209–231.

[Crucitti et al., 2006] Crucitti, P., Latora, V., and Porta, S. (2006). Centrality in networks of urban streets. *Chaos: An Interdisciplinary Journal of Nonlinear Science*, 16(1):015113.

[Cui et al., 2004] Cui, Z., Cai, X., and J Baker, C. (2004). Large-eddy simulation of turbulent flow in a street canyon. *Quarterly Journal of the Royal Meteorological Society*, 130(599):1373–1394.

[Di Sabatino et al., 2013] Di Sabatino, S., Buccolieri, R., and Salizzoni, P. (2013). Recent advancements in numerical modelling of flow and dispersion in urban areas: A short review. *International Journal of Environment and Pollution 7*, 52(3-4):172–191.

[Diekmann and Heesterbeek, 2000] Diekmann, O. and Heesterbeek, J. A. P. (2000). *Mathematical epidemiology of infectious diseases: model building, analysis and interpretation*, volume 5. John Wiley & Sons.

[Donges et al., 2009] Donges, J. F., Zou, Y., Marwan, N., and Kurths, J. (2009). Complex networks in climate dynamics. *The European Physical Journal Special*

Topics, 174(1):157–179.

[Du et al., 2015] Du, Y., Gao, C., Chen, X., Hu, Y., Sadiq, R., and Deng, Y. (2015). A new closeness centrality measure via effective distance in complex networks. *Chaos: An Interdisciplinary Journal of Nonlinear Science*, 25(3):033112.

[Erkol et al., 2019] Erkol, Ş., Castellano, C., and Radicchi, F. (2019). Systematic comparison between methods for the detection of influential spreaders in complex networks. *Scientific Reports*, 9(1):1–11.

[Fackrell, 1980] Fackrell, J. (1980). A flame ionisation detector for measuring fluctuating concentration. *Journal of Physics E: Scientific Instruments*, 13(8):888.

[Fan et al., 2019] Fan, Y., Wang, Q., Yin, S., and Li, Y. (2019). Effect of city shape on urban wind patterns and convective heat transfer in calm and stable background conditions. *Building and Environment*, 162:106288.

[Fellini et al., 2020a] Fellini, S., Ridolfi, L., and Salizzoni, P. (2020a). Street canyon ventilation: Combined effect of cross-section geometry and wall heating. *Quarterly Journal of the Royal Meteorological Society*.

[Fellini et al., 2020b] Fellini, S., Salizzoni, P., and Ridolfi, L. (2020b). Centrality metric for the vulnerability of urban networks to toxic releases. *Physical Review E*, 101(3):032312.

[Fellini et al., 2019] Fellini, S., Salizzoni, P., Soulhac, L., and Ridolfi, L. (2019). Propagation of toxic substances in the urban atmosphere: A complex network perspective. *Atmospheric Environment*, 198:291–301.

[Field, 2014] Field, C. B. (2014). *Climate change 2014–Impacts, adaptation and vulnerability: Regional aspects*. Cambridge University Press.

[Freeman, 1977] Freeman, L. C. (1977). A set of measures of centrality based on betweenness. *Sociometry*, pages 35–41.

[Garbero et al., 2010] Garbero, V., Salizzoni, P., and Soulhac, L. (2010). Experimental study of pollutant dispersion within a network of streets. *Boundary-layer meteorology*, 136(3):457–487.

[Georgakis and Santamouris, 2006] Georgakis, C. and Santamouris, M. (2006). Experimental investigation of air flow and temperature distribution in deep urban canyons for natural ventilation purposes. *Energy and buildings*, 38(4):367–376.

[Georgakis and Santamouris, 2017] Georgakis, C. and Santamouris, M. (2017). Determination of the surface and canopy urban heat island in athens central zone using advanced monitoring. *Climate*, 5(4):97.

[Giustolisi et al., 2019] Giustolisi, O., Ridolfi, L., and Simone, A. (2019). Tailoring centrality metrics for water distribution networks. *Water Resources Research*, 55(3):2348–2369.

[Goulart et al., 2018] Goulart, E. V., Coceal, O., and Belcher, S. E. (2018). Dispersion of a passive scalar within and above an urban street network. *Boundary-Layer Meteorology*, 166(3):351–366.

[Graedel, 1999] Graedel, E. T. (1999). Industrial ecology and the ecocity. *The Bridge*, 29(4):10–15.

[Gromke et al., 2008] Gromke, C., Buccolieri, R., Di Sabatino, S., and Ruck, B. (2008). Dispersion study in a street canyon with tree planting by means of wind tunnel and numerical investigations–evaluation of cfd data with experimental data. *Atmospheric Environment*, 42(37):8640–8650.

[Gromke and Ruck, 2007] Gromke, C. and Ruck, B. (2007). Influence of trees on the dispersion of pollutants in an urban street canyon - Experimental investigation of the flow and concentration field. *Atmospheric Environment*, 41(16):3287–3302.

[Gromke and Ruck, 2008] Gromke, C. and Ruck, B. (2008). Aerodynamic modelling of trees for small-scale wind tunnel studies. *Forestry*, 81(3):243–258.

[Gromke and Ruck, 2009] Gromke, C. and Ruck, B. (2009). On the impact of trees on dispersion processes of traffic emissions in street canyons. *Boundary-Layer Meteorology*, 131(1):19–34.

[Guan et al., 2003] Guan, D., Zhang, Y., and Zhu, T. (2003). A wind-tunnel study of windbreak drag. *Agricultural and forest meteorology*, 118(1-2):75–84.

[Gulyás et al., 2015] Gulyás, A., Bíró, J. J., Kőrösi, A., Rétvári, G., and Krioukov, D. (2015). Navigable networks as nash equilibria of navigation games. *Nature communications*, 6:7651.

[Güneralp et al., 2017] Güneralp, B., Zhou, Y., Ürge-Vorsatz, D., Gupta, M., Yu, S., Patel, P. L., Fragkias, M., Li, X., and Seto, K. C. (2017). Global scenarios of urban density and its impacts on building energy use through 2050. *Proceedings of the National Academy of Sciences*, 114(34):8945–8950.

[Hall, 1998] Hall, P. G. (1998). Cities in civilization.

[Hamlyn et al., 2007] Hamlyn, D., Hilderman, T., and Britter, R. (2007). A simple network approach to modelling dispersion among large groups of obstacles. *Atmospheric Environment*, 41(28):5848–5862.

[Harman and Belcher, 2006] Harman, I. and Belcher, S. (2006). The surface energy balance and boundary layer over urban street canyons. *Quarterly Journal of the Royal Meteorological Society*, 132(621):2749–2768.

[He et al., 2019] He, Y., Tablada, A., and Wong, N. H. (2019). A parametric study of angular road patterns on pedestrian ventilation in high-density urban areas. *Building and environment*, 151:251–267.

[Heinrich and Wichmann, 2004] Heinrich, J. and Wichmann, H.-E. (2004). Traffic related pollutants in Europe and their effect on allergic disease. *Current Opinion in Allergy and Clinical Immunology*, 4(5):341–348.

[Hertel et al., 2001] Hertel, O., De Leeuw, F. A., Jensen, S. S., Gee, D., Herbarth, O., Pryor, S., Palmgren, F., Olsen, E., et al. (2001). Human exposure to outdoor air pollution (IUPAC technical report). *Pure and Applied Chemistry*, 73(6):933–958.

[Hillier and Hanson, 1989] Hillier, B. and Hanson, J. (1989). *The social logic of space*. Cambridge university press.

[Hotchkiss, 1973] Hotchkiss, R. S. (1973). Air pollution transport in street canyons. *Prepared for EPA*.

[Hunt and Linden, 1999] Hunt, G. and Linden, P. (1999). The fluid mechanics of natural ventilation—displacement ventilation by buoyancy-driven flows assisted by wind. *Building and Environment*, 34(6):707–720.

[Hunter et al., 1990] Hunter, L. J., Watson, I., and Johnson, G. (1990). Modelling air flow regimes in urban canyons. *Energy and Buildings*, 15(3-4):315–324.

[Hussain and Lee, 1980] Hussain, M. and Lee, B. (1980). A wind tunnel study of the mean pressure forces acting on large groups of low-rise buildings. *Journal of Wind Engineering and Industrial Aerodynamics*, 6(3-4):207–225.

[Hyun et al., 2003] Hyun, B., Balachandar, R., Yu, K., and Patel, V. (2003). Assessment of piv to measure mean velocity and turbulence in open-channel flow. *Experiments in Fluids*, 35(3):262–267.

[Iacobello et al., 2019a] Iacobello, G., Marro, M., Ridolfi, L., Salizzoni, P., and Scarsoglio, S. (2019a). Experimental investigation of vertical turbulent transport of a passive scalar in a boundary layer: Statistics and visibility graph analysis. *Physical Review Fluids*, 4(10):104501.

[Iacobello et al., 2018] Iacobello, G., Scarsoglio, S., Kuerten, J., and Ridolfi, L. (2018). Spatial characterization of turbulent channel flow via complex networks. *Physical Review E*, 98(1):013107.

[Iacobello et al., 2019b] Iacobello, G., Scarsoglio, S., Kuerten, J., and Ridolfi, L. (2019b). Lagrangian network analysis of turbulent mixing. *Journal of Fluid Mechanics*, 865:546–562.

[Irwin, 1981] Irwin, H. (1981). The design of spires for wind simulation. *Journal of Wind Engineering and Industrial Aerodynamics*, 7(3):361 – 366.

[Janhäll, 2015] Janhäll, S. (2015). Review on urban vegetation and particle air pollution–deposition and dispersion. *Atmospheric environment*, 105:130–137.

[Jeong and Andrews, 2002] Jeong, S. J. and Andrews, M. J. (2002). Application of the k–ε turbulence model to the high Reynolds number skimming flow field of an urban street canyon. *Atmospheric environment*, 36(7):1137–1145.

[Johnson et al., 1973] Johnson, W., Ludwig, F., Dabberdt, W., and Allen, R. (1973). An urban diffusion simulation model for carbon monoxide. *Journal of the Air Pollution Control Association*, 23(6):490–498.

[Judd et al., 2011] Judd, C. M., McClelland, G. H., and Ryan, C. S. (2011). *Data analysis: A model comparison approach*. Routledge.

[Kennedy et al., 2007] Kennedy, C., Cuddihy, J., and Engel-Yan, J. (2007). The changing metabolism of cities. *Journal of industrial ecology*, 11(2):43–59.

[Kim and Baik, 2001] Kim, J.-J. and Baik, J.-J. (2001). Urban street-canyon flows with bottom heating. *Atmospheric Environment*, 35(20):3395–3404.

[Kitsak et al., 2010] Kitsak, M., Gallos, L. K., Havlin, S., Liljeros, F., Muchnik, L., Stanley, H. E., and Makse, H. A. (2010). Identification of influential spreaders in complex networks. *Nature physics*, 6(11):888.

[Kovar-Panskus et al., 2002a] Kovar-Panskus, A., Louka, P., Sini, J.-F., Savory, E., Czech, M., Abdelqari, A., Mestayer, P., and Toy, N. (2002a). Influence of geometry on the mean flow within urban street canyons–a comparison of wind tunnel experiments and numerical simulations. *Water, air and soil pollution: focus*, 2(5-6):365–380.

[Kovar-Panskus et al., 2002b] Kovar-Panskus, A., Moulinneuf, L., Savory, E., Abdelqari, A., Sini, J.-F., Rosant, J.-M., Robins, A., and Toy, N. (2002b). A wind tunnel investigation of the influence of solar-induced wall-heating on the flow regime within a simulated urban street canyon. *Water, Air and Soil Pollution: Focus*, 2(5-6):555–571.

[Kozen, 1992] Kozen, D. C. (1992). Depth-first and breadth-first search. In *The Design and Analysis of Algorithms*, pages 19–24. Springer.

[Kukkonen et al., 2001] Kukkonen, J., Valkonen, E., Walden, J., Koskentalo, T., Aarnio, P., Karppinen, A., Berkowicz, R., and Kartastenpää, R. (2001). A measurement campaign in a street canyon in Helsinki and comparison of results with predictions of the ospm model. *Atmospheric Environment*, 35(2):231–243.

[Kumar et al., 2015] Kumar, P., Morawska, L., Martani, C., Biskos, G., Neophytou, M., Di Sabatino, S., Bell, M., Norford, L., and Britter, R. (2015). The rise of low-cost sensing for managing air pollution in cities. *Environment international*, 75:199–205.

[Larson and Odoni, 1981] Larson, R. C. and Odoni, A. R. (1981). *Urban operations research*.

[Lee and Park, 1994] Lee, I. and Park, H. (1994). Parameterization of the pollutant transport and dispersion in urban street canyons. *Atmospheric Environment*, 28(14):2343–2349.

[Lee et al., 2016] Lee, S.-H., Lee, H., Park, S.-B., Woo, J.-W., Lee, D.-I., and Baik, J.-J. (2016). Impacts of in-canyon vegetation and canyon aspect ratio on the thermal environment of street canyons: numerical investigation using a coupled WRF-VUCM model. *Quarterly Journal of the Royal Meteorological Society*, 142(699):2562–2578.

[Lee Jang Sub, 2008] Lee Jang Sub (2008). Complexcity – paris.

[Leonardi et al., 2007] Leonardi, S., Orlandi, P., and Antonia, R. A. (2007). Properties of d-and k-type roughness in a turbulent channel flow. *Physics of fluids*, 19(12):125101.

[Li et al., 2016] Li, X.-X., Britter, R., and Norford, L. K. (2016). Effect of stable stratification on dispersion within urban street canyons: A large-eddy simulation. *Atmospheric environment*, 144:47–59.

[Li et al., 2012] Li, X.-X., Britter, R. E., Norford, L. K., Koh, T.-Y., and Entekhabi, D. (2012). Flow and pollutant transport in urban street canyons of different aspect ratios with ground heating: large-eddy simulation. *Boundary-layer meteorology*, 142(2):289–304.

[Li et al., 2006] Li, X.-X., Liu, C.-H., Leung, D. Y., and Lam, K. M. (2006). Recent

progress in cfd modelling of wind field and pollutant transport in street canyons. *Atmospheric Environment*, 40(29):5640–5658.

[Lin and Rockwell, 2001] Lin, J.-C. and Rockwell, D. (2001). Organized oscillations of initially turbulent flow past a cavity. *Aiaa Journal*, 39(6):1139–1151.

[Litschke and Kuttler, 2008] Litschke, T. and Kuttler, W. (2008). On the reduction of urban particle concentration by vegetation–a review. *Meteorologische Zeitschrift*, 17(3):229–240.

[Liu et al., 2004] Liu, C.-H., Barth, M. C., and Leung, D. Y. (2004). Large-eddy simulation of flow and pollutant transport in street canyons of different building-height-to-street-width ratios. *Journal of Applied Meteorology*, 43(10):1410–1424.

[Livesley et al., 2016] Livesley, S., McPherson, E. G., and Calfapietra, C. (2016). The urban forest and ecosystem services: impacts on urban water, heat, and pollution cycles at the tree, street, and city scale. *Journal of environmental quality*, 45(1):119–124.

[Llaguno-Munitxa et al., 2017] Llaguno-Munitxa, M., Bou-Zeid, E., and Hultmark, M. (2017). The influence of building geometry on street canyon air flow: Validation of large eddy simulations against wind tunnel experiments. *Journal of Wind Engineering and Industrial Aerodynamics*, 165:115–130.

[Louka et al., 2000] Louka, P., Belcher, S., and Harrison, R. (2000). Coupling between air flow in streets and the well-developed boundary layer aloft. *Atmospheric Environment*, 34(16):2613–2621.

[Louka et al., 2002] Louka, P., Vachon, G., Sini, J.-F., Mestayer, P., and Rosant, J.-M. (2002). Thermal effects on the airflow in a street canyon - Nantes' 99 experimental results and model simulations. *Water, air and soil pollution: Focus*, 2(5-6):351–364.

[Lynch, 1984] Lynch, K. (1984). *Good city form*. MIT press.

[Lyon, 2015] Lyon, B. (2015). The Opte Project. www.opte.org. Accessed: 2020-08-13.

[MacKenzie, 2020] MacKenzie, D. (2020). Is it super-spreading? *New Scientist (1971)*, 245(3270):5.

[Maglaras and Katsaros, 2012] Maglaras, L. A. and Katsaros, D. (2012). New measures for characterizing the significance of nodes in wireless ad hoc networks via localized path-based neighborhood analysis. *Social Network Analysis and Mining*, 2(2):97–106.

[Manickathan et al., 2018] Manickathan, L., Defraeye, T., Allegrini, J., Derome, D., and Carmeliet, J. (2018). Comparative study of flow field and drag coefficient of model and small natural trees in a wind tunnel. *Urban Forestry & Urban Greening*, 35:230–239.

[Marchiori and Latora, 2000] Marchiori, M. and Latora, V. (2000). Harmony in the small-world. *Physica A: Statistical Mechanics and its Applications*, 285(3-4):539–546.

[Marro et al., 2020] Marro, M., Gamel, H., Méjean, P., Correia, H., Soulhac, L.,

and Salizzoni, P. (2020). High-frequency simultaneous measurements of velocity and concentration within turbulent flows in wind-tunnel experiments. *Experiments in Fluids*, 61(12):1–13.

[Marucci and Carpentieri, 2019] Marucci, D. and Carpentieri, M. (2019). Effect of local and upwind stratification on flow and dispersion inside and above a bi-dimensional street canyon. *Building and Environment*, 156:74–88.

[May and Lloyd, 2001] May, R. M. and Lloyd, A. L. (2001). Infection dynamics on scale-free networks. *Physical Review E*, 64(6):066112.

[Mayer, 1999] Mayer, H. (1999). Air pollution in cities. *Atmospheric Environment*, 33(24-25):4029–4037.

[McLeish, 2017] McLeish, C. (2017). Recasting the threat of chemical terrorism in the EU: The issue of returnees from the syrian conflict. *European Journal of Risk Regulation*, 8(4):643–657.

[Mehta and Lavan, 1969] Mehta, U. B. and Lavan, Z. (1969). Flow in a two dimensional channel with a rectangular cavity. *Journal of Applied Mechanics*, 36:897–901.

[Meroney, 1968] Meroney, R. N. (1968). Characteristics of wind and turbulence in and above model forests. *Journal of Applied Meteorology*, 7(5):780–788.

[Meroney, 1980] Meroney, R. N. (1980). Wind-tunnel simulation of the flow over hills and complex terrain. *Journal of Wind Engineering and Industrial Aerodynamics*, 5(3-4):297–321.

[Meroney et al., 1996] Meroney, R. N., Pavageau, M., Rafailidis, S., and Schatzmann, M. (1996). Study of line source characteristics for 2-d physical modelling of pollutant dispersion in street canyons. *Journal of wind Engineering and industrial Aerodynamics*, 62(1):37–56.

[Miao et al., 2020] Miao, C., Yu, S., Hu, Y., Bu, R., Qi, L., He, X., and Chen, W. (2020). How the morphology of urban street canyons affects suspended particulate matter concentration at the pedestrian level: An in-situ investigation. *Sustainable Cities and Society*, 55:102042.

[Moreno et al., 2004] Moreno, Y., Nekovee, M., and Pacheco, A. F. (2004). Dynamics of rumor spreading in complex networks. *Physical review E*, 69(6):066130.

[Mori and Naganuma, 2009] Mori, T. and Naganuma, K. (2009). Experimental investigation of the three-dimensional nature of turbulent flow over a rectangular cavity. *Journal of Fluid Science and Technology*, 4(3):746–757.

[Murena et al., 2011] Murena, F., Di Benedetto, A., D'Onofrio, M., and Vitiello, G. (2011). Mass transfer velocity and momentum vertical exchange in simulated deep street canyons. *Boundary-layer meteorology*, 140(1):125.

[Murena and Mele, 2016] Murena, F. and Mele, B. (2016). Effect of balconies on air quality in deep street canyons. *Atmospheric Pollution Research*, 7(6):1004–1012.

[Nakamura and Oke, 1988] Nakamura, Y. and Oke, T. R. (1988). Wind, temperature and stability conditions in an east-west oriented urban canyon. *Atmospheric*

Environment (1967), 22(12):2691–2700.

[Namdeo and Colls, 1996] Namdeo, A. and Colls, J. (1996). Development and evaluation of SBLINE, a suite of models for the prediction of pollution concentrations from vehicles in urban areas. *Science of the Total Environment*, 189:311–320.

[Nåsell, 2002] Nåsell, I. (2002). Stochastic models of some endemic infections. *Mathematical Biosciences*, 179(1):1–19.

[Nazarian et al., 2018] Nazarian, N., Martilli, A., and Kleissl, J. (2018). Impacts of realistic urban heating, part I: spatial variability of mean flow, turbulent exchange and pollutant dispersion. *Boundary-layer meteorology*, 166(3):367–393.

[Newman, 2010] Newman, M. (2010). *Networks: An introduction*. Oxford university press.

[Newman, 2018] Newman, M. (2018). *Networks*. Oxford university press.

[Newman, 2001] Newman, M. E. (2001). Scientific collaboration networks. ii. shortest paths, weighted networks, and centrality. *Physical Review E*, 64(1):016132.

[Newman, 2002] Newman, M. E. (2002). Spread of epidemic disease on networks. *Physical Review E*, 66(1):016128.

[Niachou et al., 2008] Niachou, K., Livada, I., and Santamouris, M. (2008). Experimental study of temperature and airflow distribution inside an urban street canyon during hot summer weather conditions. part II: Airflow analysis. *Building and environment*, 43(8):1393–1403.

[Nironi, 2013] Nironi, C. (2013). *Concentration fluctuations of a passive scalar in a turbulent boundary layer*. PhD thesis, Ecole Centrale de Lyon.

[Nironi et al., 2015] Nironi, C., Salizzoni, P., Marro, M., Mejean, P., Grosjean, N., and Soulhac, L. (2015). Dispersion of a passive scalar fluctuating plume in a turbulent boundary layer. part i: Velocity and concentration measurements. *Boundary-layer meteorology*, 156(3):415–446.

[Offerle et al., 2007] Offerle, B., Eliasson, I., Grimmond, C., and Holmer, B. (2007). Surface heating in relation to air temperature, wind and turbulence in an urban street canyon. *Boundary-Layer Meteorology*, 122(2):273–292.

[Oke, 1982] Oke, T. R. (1982). The energetic basis of the urban heat island. *Quarterly Journal of the Royal Meteorological Society*, 108(455):1–24.

[Oke, 1988] Oke, T. R. (1988). Street design and urban canopy layer climate. *Energy and Buildings*, 11:103–113.

[Oke, 2002] Oke, T. R. (2002). *Boundary layer climates*. Routledge.

[Oliveira et al., 2011] Oliveira, S., Andrade, H., and Vaz, T. (2011). The cooling effect of green spaces as a contribution to the mitigation of urban heat: A case study in lisbon. *Building and environment*, 46(11):2186–2194.

[Olshanskii et al., 2015] Olshanskii, M. A., Heister, T., Rebholz, L. G., and Galvin, K. J. (2015). Natural vorticity boundary conditions on solid walls. *Computer Methods in Applied Mechanics and Engineering*, 297:18–37.

[Pastor-Satorras and Vespignani, 2001] Pastor-Satorras, R. and Vespignani, A. (2001). Epidemic spreading in scale-free networks. *Physical Review Letters*,

86(14):3200.

[Pavageau and Schatzmann, 1999] Pavageau, M. and Schatzmann, M. (1999). Wind tunnel measurements of concentration fluctuations in an urban street canyon. *Atmospheric Environment*, 33(24-25):3961–3971.

[Pei and Makse, 2013] Pei, S. and Makse, H. A. (2013). Spreading dynamics in complex networks. *Journal of Statistical Mechanics: Theory and Experiment*, 2013(12):P12002.

[Peng et al., 2019] Peng, Y., Gao, Z., Buccolieri, R., and Ding, W. (2019). An investigation of the quantitative correlation between urban morphology parameters and outdoor ventilation efficiency indices. *Atmosphere*, 10(1):33.

[Polletta and Jasper, 2001] Polletta, F. and Jasper, J. M. (2001). Collective identity and social movements. *Annual review of Sociology*, 27(1):283–305.

[Porta et al., 2006] Porta, S., Crucitti, P., and Latora, V. (2006). The network analysis of urban streets: A dual approach. *Physica A: Statistical Mechanics and its Applications*, 369(2):853–866.

[Prasad, 2000] Prasad, A. K. (2000). Particle image velocimetry. *Current Science-Bangalore-*, 79(1):51–60.

[Rafailidis, 1997] Rafailidis, S. (1997). Influence of building areal density and roof shape on the wind characteristics above a town. *Boundary-layer meteorology*, 85(2):255–271.

[Rinaldo et al., 2006] Rinaldo, A., Banavar, J. R., and Maritan, A. (2006). Trees, networks, and hydrology. *Water Resources Research*, 42(6).

[Robins et al., 2002] Robins, A., Savory, E., Scaperdas, A., and Grigoriadis, D. (2002). Spatial variability and source-receptor relations at a street intersection. *Water, Air and Soil Pollution: Focus*, 2(5-6):381–393.

[Rochat, 2009] Rochat, Y. (2009). Closeness centrality extended to unconnected graphs: The harmonic centrality index. Technical report.

[Roth, 2000] Roth, M. (2000). Review of atmospheric turbulence over cities. *Quarterly Journal of the Royal Meteorological Society*, 126(564):941–990.

[Salat et al., 2014] Salat, S., Bourdic, L., and Labbe, F. (2014). Breaking symmetries and emerging scaling urban structures: A morphological tale of 3 cities: Paris, new york and barcelona. *ArchNet-IJAR: International Journal of Architectural Research*, 8(2):77.

[Salim et al., 2011] Salim, S. M., Cheah, S. C., and Chan, A. (2011). Numerical simulation of dispersion in urban street canyons with avenue-like tree plantings: comparison between rans and les. *Building and Environment*, 46(9):1735–1746.

[Salizzoni, 2006] Salizzoni, P. (2006). *Mass and momentum transfer in the urban boundary layer*. PhD thesis, Ecully, Ecole centrale de Lyon.

[Salizzoni et al., 2011] Salizzoni, P., Marro, M., Soulhac, L., Grosjean, N., and Perkins, R. J. (2011). Turbulent transfer between street canyons and the overlying atmospheric boundary layer. *Boundary-layer meteorology*, 141(3):393–414.

[Salizzoni et al., 2009] Salizzoni, P., Soulhac, L., and Mejean, P. (2009). Street canyon ventilation and atmospheric turbulence. *Atmospheric Environment*, 43(32):5056–5067.

[Salizzoni et al., 2008] Salizzoni, P., Soulhac, L., Mejean, P., and Perkins, R. J. (2008). Influence of a two-scale surface roughness on a neutral turbulent boundary layer. *Boundary-layer meteorology*, 127(1):97–110.

[Santamouris et al., 2001] Santamouris, M., Papanikolaou, N., Livada, I., Koronakis, I., Georgakis, C., Argiriou, A., and Assimakopoulos, D. (2001). On the impact of urban climate on the energy consumption of buildings. *Solar energy*, 70(3):201–216.

[Scaperdas, 2000] Scaperdas, A.-S. (2000). *Modelling air flow and pollutant dispersion at urban canyon intersections*. PhD thesis, Imperial College London (University of London).

[Scarsoglio et al., 2017] Scarsoglio, S., Cazzato, F., and Ridolfi, L. (2017). From time-series to complex networks: Application to the cerebrovascular flow patterns in atrial fibrillation. *Chaos: An Interdisciplinary Journal of Nonlinear Science*, 27(9):093107.

[Schlueter-Kuck and Dabiri, 2017] Schlueter-Kuck, K. L. and Dabiri, J. O. (2017). Coherent structure colouring: identification of coherent structures from sparse data using graph theory. *Journal of Fluid Mechanics*, 811:468–486.

[Schneide et al., 2018] Schneide, C., Pandey, A., Padberg-Gehle, K., and Schumacher, J. (2018). Probing turbulent superstructures in rayleigh-bénard convection by lagrangian trajectory clusters. *Physical Review Fluids*, 3(11):113501.

[Ser-Giacomi et al., 2019] Ser-Giacomi, E., Baudena, A., Rossi, V., Vasile, R., Lopez, C., and Hernández-Garcıa, E. (2019). From network theory to dynamical systems and back: Lagrangian betweenness reveals bottlenecks in geophysical flows. *arXiv preprint arXiv:1910.04722*.

[Ser-Giacomi et al., 2015] Ser-Giacomi, E., Rossi, V., López, C., and Hernandez-Garcia, E. (2015). Flow networks: A characterization of geophysical fluid transport. *Chaos: An Interdisciplinary Journal of Nonlinear Science*, 25(3):036404.

[Seto et al., 2017] Seto, K. C., Golden, J. S., Alberti, M., and Turner, B. L. (2017). Sustainability in an urbanizing planet. *Proceedings of the National Academy of Sciences*, 114(34):8935–8938.

[Shi et al., 2019] Shi, L., Wang, Y., Jin, Y., Zhang, G., and Zhang, D. (2019). Parametrical study and turbulence analysis of high-speed flows around an open cavity using large eddy simulation. *Fluid Dynamics Research*, 51(3):035503.

[Sini et al., 1996] Sini, J.-F., Anquetin, S., and Mestayer, P. G. (1996). Pollutant dispersion and thermal effects in urban street canyons. *Atmospheric environment*, 30(15):2659–2677.

[Smilkov and Kocarev, 2012] Smilkov, D. and Kocarev, L. (2012). Influence of the network topology on epidemic spreading. *Physical Review E*, 85(1):016114.

[Snyder, 1994] Snyder, W. (1994). Some observations of the influence of stratification on diffusion in building wakes. In Castro, I. and Rockliff, N., editors, *Stably Stratified Flows and Dispersion over Topography*, pages 301–324. Claredon Press.

[Solazzo and Britter, 2007] Solazzo, E. and Britter, R. (2007). Transfer processes in a simulated urban street canyon. *Boundary-Layer Meteorology*, 124(1):43–60.

[Solazzo et al., 2008] Solazzo, E., Cai, X., and Vardoulakis, S. (2008). Modelling wind flow and vehicle-induced turbulence in urban streets. *Atmospheric Environment*, 42(20):4918–4931.

[Solé et al., 2010] Solé, R. V., Corominas-Murtra, B., Valverde, S., and Steels, L. (2010). Language networks: Their structure, function, and evolution. *Complexity*, 15(6):20–26.

[Soulhac, 2000] Soulhac, L. (2000). *Modélisation de la dispersion atmosphérique à l'intérieur de la canopée urbaine*. PhD thesis, Ecole Centrale de Lyon.

[Soulhac et al., 2009] Soulhac, L., Garbero, V., Salizzoni, P., Mejean, P., and Perkins, R. (2009). Flow and dispersion in street intersections. *Atmospheric Environment*, 43(18):2981–2996.

[Soulhac et al., 2017] Soulhac, L., Nguyen, C. V., Volta, P., and Salizzoni, P. (2017). The model sirane for atmospheric urban pollutant dispersion. part iii: Validation against no2 yearly concentration measurements in a large urban agglomeration. *Atmospheric environment*, 167:377–388.

[Soulhac et al., 2008] Soulhac, L., Perkins, R. J., and Salizzoni, P. (2008). Flow in a street canyon for any external wind direction. *Boundary-Layer Meteorology*, 126(3):365–388.

[Soulhac et al., 2003] Soulhac, L., Puel, C., Duclaux, O., and Perkins, R. (2003). Simulations of atmospheric pollution in greater lyon an example of the use of nested models. *Atmospheric Environment*, 37(37):5147–5156.

[Soulhac and Salizzoni, 2010] Soulhac, L. and Salizzoni, P. (2010). Dispersion in a street canyon for a wind direction parallel to the street axis. *Journal of Wind Engineering and Industrial Aerodynamics*, 98(12):903–910.

[Soulhac et al., 2011] Soulhac, L., Salizzoni, P., Cierco, F.-X., and Perkins, R. (2011). The model SIRANE for atmospheric urban pollutant dispersion; part I, presentation of the model. *Atmospheric Environment*, 45(39):7379–7395.

[Soulhac et al., 2012] Soulhac, L., Salizzoni, P., Mejean, P., Didier, D., and Rios, I. (2012). The model sirane for atmospheric urban pollutant dispersion; part ii, validation of the model on a real case study. *Atmospheric environment*, 49:320–337.

[Soulhac et al., 2013] Soulhac, L., Salizzoni, P., Mejean, P., and Perkins, R. (2013). Parametric laws to model urban pollutant dispersion with a street network approach. *Atmospheric Environment*, 67:229–241.

[Stacey et al., 1994] Stacey, G., Belcher, R., Wood, C., and Gardiner, B. (1994). Wind flows and forces in a model spruce forest. *Boundary-Layer Meteorology*, 69(3):311–334.

[Theeuwes et al., 2014] Theeuwes, N., Steeneveld, G., Ronda, R., Heusinkveld, B., Van Hove, L., and Holtslag, A. (2014). Seasonal dependence of the urban heat island on the street canyon aspect ratio. *Quarterly Journal of the Royal Meteorological Society*, 140(684):2197–2210.

[Tominaga and Stathopoulos, 2012] Tominaga, Y. and Stathopoulos, T. (2012). CFD modeling of pollution dispersion in building array: Evaluation of turbulent scalar flux modeling in RANS model using LES results. *Journal of Wind Engineering and Industrial Aerodynamics*, 104:484–491.

[Tominaga and Stathopoulos, 2016] Tominaga, Y. and Stathopoulos, T. (2016). Ten questions concerning modeling of near-field pollutant dispersion in the built environment. *Building and Environment*, 105:390–402.

[Tritton, 2012] Tritton, D. J. (2012). *Physical fluid dynamics*. Springer Science & Business Media.

[Tsonis et al., 2006] Tsonis, A. A., Swanson, K. L., and Roebber, P. J. (2006). What do networks have to do with climate? *Bulletin of the American Meteorological Society*, 87(5):585–596.

[Tucker, 2000] Tucker, J. B. (2000). *Toxic terror: Assessing terrorist use of chemical and biological weapons*. MIT Press.

[Uehara et al., 2000] Uehara, K., Murakami, S., Oikawa, S., and Wakamatsu, S. (2000). Wind tunnel experiments on how thermal stratification affects flow in and above urban street canyons. *Atmospheric Environment*, 34(10):1553–1562.

[UN, 2019] UN (2019). Climate change - summit.

[Valiente, 2013] Valiente, G. (2013). *Algorithms on trees and graphs*. Springer Science & Business Media.

[Van Mieghem et al., 2017] Van Mieghem, P., Devriendt, K., and Cetinay, H. (2017). Pseudoinverse of the laplacian and best spreader node in a network. *Physical Review E*, 96:032311.

[Vardoulakis et al., 2003] Vardoulakis, S., Fisher, B. E., Pericleous, K., and Gonzalez-Flesca, N. (2003). Modelling air quality in street canyons: a review. *Atmospheric environment*, 37(2):155–182.

[West et al., 1999] West, G. B., Brown, J. H., and Enquist, B. J. (1999). The fourth dimension of life: fractal geometry and allometric scaling of organisms. *science*, 284(5420):1677–1679.

[WHO, 2018] WHO (2018). Ambient (outdoor) air quality and health. https://www.who.int/news-room/factsheets/detail/ambient-(outdoor)-air-qualityand-health. Accessed: 2019-12-05.

[Wiernga, 1993] Wiernga, J. (1993). Representative roughness parameters for homogeneous terrain. *Boundary-Layer Meteorology*, 63(4):323–363.

[Wolman, 1965] Wolman, A. (1965). The metabolism of cities. *Scientific American*, 213(3):178–193.

[Xie et al., 2007] Xie, X., Liu, C.-H., and Leung, D. Y. (2007). Impact of building façades and ground heating on wind flow and pollutant transport in street

canyons. *Atmospheric Environment*, 41(39):9030–9049.

[Yamartino and Wiegand, 1986] Yamartino, R. J. and Wiegand, G. (1986). Development and evaluation of simple models for the flow, turbulence and pollutant concentration fields within an urban street canyon. *Atmospheric Environment (1967)*, 20(11):2137–2156.

[Zeng and Zhang, 2013] Zeng, A. and Zhang, C.-J. (2013). Ranking spreaders by decomposing complex networks. *Physics Letters A*, 377(14):1031–1035.

This Ph.D. thesis has been typeset by means of the TEX-system facilities. The typesetting engine was pdfLATEX. The document class was `toptesi`, by Claudio Beccari, with option `tipotesi=scudo`. This class is available in every up-to-date and complete TEX-system installation.